# Underwater Iceberg Profiling and Motion Estimation using Autonomous Underwater Vehicles

by

©Mingxi Zhou

A Thesis submitted to the School of Graduate Studies in partial fulfillment of the requirements for the degree of

**Doctor of Philosophy**

**Faculty of Engineering and Applied Science**
**Memorial University of Newfoundland**

Memorial University of Newfoundland

**May, 2017**

St. John's Newfoundland

# Abstract

Icebergs originating from high latitude glaciers have drawn much attention from scientists and offshore operators in the North Atlantic. Scientists are curious about the iceberg drift and deterioration, while the offshore industry is concerned about the potential risks and damages on offshore oil platforms and infrastructures. In order to provide information to improve the iceberg drift and deterioration model constructed by scientists, and to assess the threats posed by icebergs to offshore platforms, iceberg shapes need to be measured. For the above water portion, optical instruments such as a camera and a laser scanner/LIDAR can be used. However, measuring the underwater portion of an iceberg is more challenging due to navigational constraints and sensor limitations. One approach, commonly used, is to deploy a horizontal plane scanning sonar from a support vessel at several locations around the iceberg. There are many drawbacks to this method, including the cost, sensing trade-offs in resolution and coverage, as well as constraints because of weather conditions limiting safe operations.

The technology of Autonomous Underwater Vehicles (AUVs) has been developing rapidly in the last two decades. AUVs are commonly chosen to carry scientific sensors for various oceanographic applications. Without human intervention, AUVs can accomplish pre-programmed missions autonomously and deliver scientific data upon the users' request. With these advantages, AUVs are considered as potential candidates

in underwater iceberg sensing operations because they can operate close to icebergs to measure shapes and collect environmental data of the surrounding water. Sonar is usually used for underwater mapping applications. Since AUVs are typically quieter acoustically than manned surface vessels, a low noise to signal ratio can be achieved on sonars carried by AUVs.

In this research, a technology of AUV-based underwater iceberg-profiling is evaluated. An iceberg-profiling simulator is constructed to analyse underwater iceberg-profiling missions. With the simulator, the accuracy of AUV-based operation is compared with conventional methods of deploying sonar profilers around icebergs. Beyond the simulation, a guidance, navigation, and control (GNC) system is designed with an objective of guiding the vehicle traveling around the iceberg at a standoff distance. The GNC uses measurements from a mechanical scanning sonar to construct a vehicle-attached occupancy map (VOM) that the probability of occupancy of the cells in the VOM is updated based on a dynamic inverse-sonar model. Using the occupancy information about the cells in the VOM, the line-of-sight (LOS) guidance law is used to compute the desired heading for the existing heading controller in the AUV. The GNC is first calibrated and validated in a simulated environment. Then, an AUV equipped with a forward side-looking mechanical scanning sonar is deployed in the field. The GNC guides the vehicle circumnavigated an iceberg autonomously, and underwater shape of the target iceberg is represented using the sonar samples.

The point cloud may deviate from the original iceberg shape due to the iceberg movement. A motion estimation algorithm is developed to estimate the iceberg motion for converting the point cloud into an iceberg-centered coordinate system. Two point clouds measured at different times, inputs of the motion estimation algorithm, are presumed to be identical in the iceberg-centered coordinate system. Then, the algorithm iteratively updates the motion estimates based on the translational matrix and

rotational matrix from an iterative closest point (ICP) algorithm to match the point clouds. The hypothesis that two point clouds are identical in the iceberg-centered coordinate system is valid when the motion estimates are converged in the updating process. Once the iceberg motion is resolved, the point cloud in the inertial coordinate can be converted in to the iceberg-centered coordinate to present the true iceberg shape. The algorithm for estimating iceberg motion is applied to data collected from the simulation environment and the field trials in Newfoundland.

# Acknowledgements

First of all, I want to express my sincere gratitude to my supervisors, Ralf Bachmayer, Brad deYoung, and Len Zedel for their insightful advice and instruction during my research. I would like to thank the financial support from Research & Development Corporation (RDC) of Newfoundland and Labrador through Ocean Industries Student Research Award (OISRA), and the Natural Sciences and Engineering Research Council (NSERC) through the NSERC Canadian Field Robotics Network (NCFRN), and Memorial University of Newfoundland. This research is also supported by the Memorial University of Newfoundland through the Atlantic Canada Opportunities Agency, the Government of Newfoundland and Labrador, the Research and Development Corporation of Newfoundland and Labrador, the Marine Institute and Suncor Energy - Terra Nova Project.

I also would like to thank Neil Riggs and Mike Hakomaki for the arrangements and logistics for field trials; and the people who helped me in various ways: Federico Luchino for electronics, Levi MacNeil for designing the glider thruster, Robin Matthew, Mark Downey, Oscar Parslow and Johanna Hansen (McGill University) for glider deployments and ballasting, the Captain, and crews of Anne S. Pierce, Inquisitor (Shamook), the Captain, and crews of the Midnight Shadow for supporting the field trials, and Prof. Stephen Rock and Marcus Hammond (Stanford University) for providing advice on the vehicle controls. Finally, I would like to thank my supportive family.

# Table of Contents

# List of Tables

# List of Figures

# List of Symbols

| | |
|---|---|
| **Inertial coordinate system** | |
| $X_e - Y_e - Z_e$ | the inertial coordinate system where $X_e$ is pointing north, $Y_e$ is pointing east and $Z_e$ is pointing downward |
| $O_e$ | the origin of the inertial coordinate system |
| $t$ | time variable where at the beginning of a mission $t$ is 0 |
| $\mathbf{P}_t^e$ | a point in the inertial coordinate system sampled at time t |
| $\mathbf{P}_{j:k}^e$ | a point cloud in the inertial coordiante system that $\mathbf{P}_{j:k}^e = \{\mathbf{P}_j^e, ..., \mathbf{P}_k^e\}$ |
| **Vehicle coordinate system** | |
| $X_v(t) - Y_v(t) - Z_v(t)$ | the vehicle coordinate system at time t |
| $O_v$ | origin of the vehicle coordinate system |
| $x_v(t)$, $y_v(t)$, $z_v(t)$ | the location of the vehicle ($O_v$) |
| $\phi(t)$, $\theta(t)$, $\psi(t)$ | the roll, pitch, yaw angle of the vehicle |
| $\dot{x}_v(t)$, $\dot{y}_v(t)$, $\dot{z}_v(t)$ | velocity of the vehicle in the inertial coordinate system |
| $\mathbf{P}_t^v$ | a point in the vehicle coordinate system sampled at time t |
| $\mathbf{P}_{j:k}^v$ | a point cloud in the vehicle coordinate system that $\mathbf{P}_{j:k}^v = \{\mathbf{P}_j^v, ..., \mathbf{P}_k^v\}$ |
| $\mu$ | magnetic declination (positive to the east) |
| **Iceberg coordinate system** | |
| $X_i(t) - Y_i(t) - Z_i(t)$ | the coordinate system attached to the iceberg at time t |
| $O_i$ | the origin of the iceberg attached coordinate system |
| $x_i(t)$, $y_i(t)$, $z_i(t)$ | the location of the iceberg ($O_i$) |
| $\phi_i(t)$, $\theta_i(t)$, $\psi_i(t)$ | the roll, pitch and yaw angle of the iceberg |
| $u_i$, $v_i$, $r_i$ | the northing velocity, easting velocity and planar rotational velocity $u_i = \dot{x}_i(t)$, $v_i = \dot{y}_i(t)$, $\omega = \dot{\psi}_i(t)$ |
| $\mathbf{P}_t^i$ | a point in $X_i - Y_i - Z_i - t$ and sampled at t |
| $\mathbf{P}_{j:k}^i$ | a point cloud in $X_i - Y_i - Z_i - t$ that $\mathbf{P}_{j:k}^i = \{\mathbf{P}_j^i, ..., \mathbf{P}_k^i\}$ |

| Transformation Matrice | |
|---|---|
| $\mathbf{R}_{v,t}^{e}$ | rotation matrix from $X_v(t) - Y_v(t) - Z_v(t)$ to $X_e - Y_e - Z_e$ |
| $\mathbf{T}_{v,t}^{e}$ | the translation of the vehicle $[x_v(t), y_v(t), z_v(t)]^T$ |
| $\mathbf{R}_{e}^{v,t}$ | rotation matrix from $X_e - Y_e - Z_e$ to $X_v(t) - Y_v(t) - Z_v(t)$ |
| $\mathbf{T}_{e}^{v,t}$ | $-\mathbf{T}_{v,t}^{e}$ |
| $\mathbf{R}_{i,t}^{e}$ | rotation matrix from $X_i(t) - Y_i(t) - Z_i(t)$ to $X_e - Y_e - Z_e$ |
| $\mathbf{T}_{i,t}^{e}$ | the translation of the iceberg $[x_i(t), y_i(t), z_i(t)]^T$ |
| $\mathbf{R}_{e}^{i,t}$ | rotation matrix from $X_e - Y_e - Z_e$ to $X_i(t) - Y_i(t) - Z_i(t)$ |
| $\mathbf{T}_{e}^{i,t}$ | $-\mathbf{T}_{i,t}^{e}$ |
| Sonar | |
| $\sigma(t)$ | scanning angle at time $t$ |
| $\Delta\sigma$ | stepping angle |
| $\beta$ | forward-looking angle |
| $\delta$ | angle of the simulated ray to the central ray |
| $R_s$ | profiling range of the sonar |
| $R_t$ | extracted range from the sonar to an object |
| $B_j$ | echo intensity at range index i |
| SL | source level |
| DI | directivity |
| TL | transmission loss |
| AL | attenuation loss |
| BS | backscatter strength |
| TS | target strength |
| EI | echo intensity |
| $\alpha$ | attenuation coefficient |
| $\theta_i$ | incident angle |
| $\mu_i$ | backscatter coefficient |
| Guidance, Control and Navigation system | |
| $P(M_{x,y})$ | initial value of the probability of a occupancy map |
| $P(M_{x^G,y^G}^{G})$ | initial probability of a global occupancy map |
| $P(M_{x^V,y^V}^{V})$ | initial probability of a vehicle-attached occupancy map |
| $P(M_{x,y}\|R_1, ..., R_t)$ | probability of occupancy in an occupancy map at location $< x, y >$ with sonar measurement from time 1 to time t |
| $P(M_{x^G,y^G}^{G}\|R_1, ..., R_t)$ | probability of occupancy in the global occupancy map at index <x,y> with sonar measurement from time 1 to time t |
| $P(M_{x^v,y^v}^{v}\|R_1, ..., R_t)$ | probability of occupancy in the vehicle-attached occupancy map at index <x,y> with sonar measurement from time 1 to time t |
| $l_{x,y}^{t}$ | log-odds of location <x,y> in the occupancy map |
| $\theta_s^v$ | the slope of the terrain relative to the vehicle |
| $\theta_s^G$ | the slope of the terrain in relative to the true north $\theta_s^G = \psi(t) + \theta_s^v$ |
| $P_o(\delta, R)$ | probability of occupancy from the dynamic inverse-sonar model |
| $\Delta$ | forward-looking distance in Line-of-sight control |
| $e_T$ | cross-track error for the Line-of-sight control |

# List of Abbreviations

| | |
|---|---|
| ADCP | Acoustic Doppler Current Profiler |
| AOSL | Autonomous Ocean Systems Laboratory |
| ASV | Autonomous Surface Vehicle |
| AUG | Autonomous Underwater Glider |
| AUV | Autonomous Underwater Vehicle |
| CHIRP | Compressed High-Intensity Radiated Pulse |
| CTD | Conductivity-Temperature-Depth |
| DOF | Degrees of freedom |
| DVL | Doppler Velocity Logger |
| GPS | Global Positioning System |
| GNC | Guidance, Navigation and Control |
| GOM | Global Occupancy Map |
| ICP | Iterative Closest Point |
| LBL | Long Baseline |
| LMC | Local Mission Coordinate |
| LOS | Line-of-sight |
| MUN | Memorial University of Newfoundland |
| NED | North-East-Down |
| NRCC | National Research Council Canada |
| PID | Proportional-integral-derivative |
| RHIB | Rigid-hull inflatable boat |
| RMS | Root-mean-square |
| SBC | Single board computer |
| SBL | Short Baseline |
| SLAM | Simultaneous Localization and Mapping (SLAM) |
| SDK | Software Development Kit |
| USBL | Ultra-short baseline |
| UTM | Universal Transverse Mercator |
| VOM | Vehicle-attached Occupancy Map |

# Chapter 1

# Introduction

## 1.1 Motivation

With increasing activities in the North Atlantic and sub-polar regions, icebergs originating from Western Greenland cause concerns to the offshore operations and marine transportation. A deep-keel iceberg could scour the seafloor leading to a risk of destroying seafloor pipelines and underwater infrastructure. In order to prevent these hazards posed by icebergs, iceberg management[1] is introduced to monitor and predict icebergs drift, to alert the offshore production, and to deviate threatening icebergs if necessary. The underwater portion of an iceberg, about 90% of the overall volume, is a key factor affecting its trajectory and stability [3]. Therefore, increased knowledge about the underwater profile of an iceberg is necessary for a better prediction in iceberg drift and a safer operation when altering the trajectory of icebergs.

The shapes of Icebergs are difficult to measure as they are large and irregularly shaped. In addition, the shape of an iceberg changes over time due to their deterioration, calving and rolling. Therefore, an accurate iceberg representation requires multiple assessments conducted at different times. Then the variation in shape changes can be

animated. At present, the underwater portion of an iceberg is commonly measured using a horizontal scanning sonar that is deployed from a ship at various locations around an iceberg [4] as shown in Figure 1.1. The overall underwater shape is created by merging the acoustic snapshots from multiple deployments. The survey takes a significant amount of time and resources to profile a single iceberg using this conventional method. The movement of icebergs poses another challenge. Icebergs translate and rotate due to ocean currents, surface waves, and winds [3]. The measurements from the sonar have to be corrected for the iceberg motion to represent the actual iceberg shape.

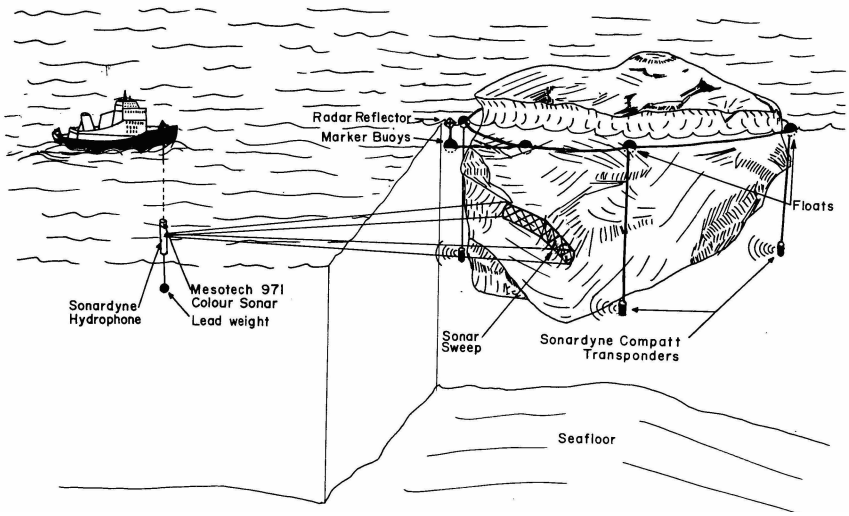


Figure 1.1: Configuration of the underwater iceberg mapping technique used in [4].

An improved method that is relatively lower cost and more convenient to map the underwater shape of icebergs is required. As well, the near-iceberg features such as water density and water circulation should be sampled to provide relevant background environmental data for iceberg drift and deterioration modeling (see Figure 1.2). In this research, an Autonomous Underwater Vehicle (AUV) is proposed to map the underside of icebergs without human intervention. The iceberg surface will be measured

by an acoustic sonar integrated into the AUV. A Guidance, Navigation and Control system will be designed to control the vehicle to follow the iceberg surface based on the sonar-measured ranges. Finally, an algorithm will be developed to estimate the iceberg motion using sonar measurements for iceberg shape reconstruction.

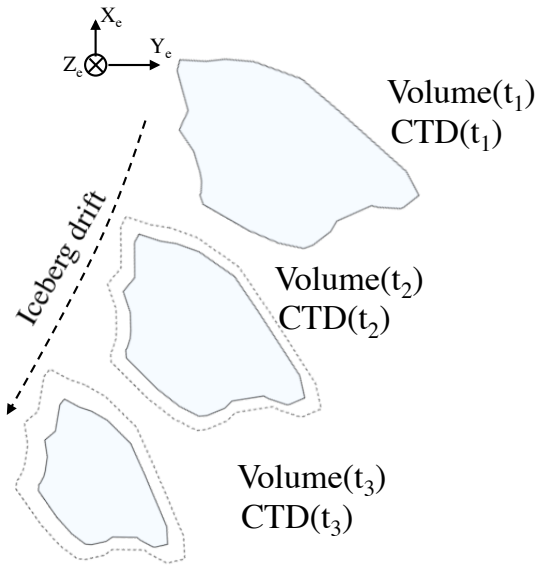


Figure 1.2: Iceberg drift and deterioration. The dotted lines shows the previous measured iceberg shape. The volume of iceberg and Conductivity-Temperature of the surrounding water vary with time.

## 1.2 Autonomous Underwater Vehicles (AUVs)

An Autonomous Underwater Vehicle (AUV) is an unmanned robotic system that is piloted by an on-board computer without continuously regular human intervention. They operate on their own according to pre-programmed missions or pre-defined mission objectives from AUV operators. They can access the high risk areas that cannot be approached by manned vehicles. During missions, multiple sensors are operated simultaneously for environmental assessment and vehicle guidance. The high-quality

multi-modal data is beneficial for post-processing and sensor fusion for scientific understanding of the ocean dynamics and iceberg interactions. The autonomy, wide operational range, and high-quality data make the AUV one of the primary platforms used in ocean exploration today.

Table 1.1: Summary of the characteristics of AUVs

| Size | Small | | Large | Extra-large |
|---|---|---|---|---|
| Class | man portable | light weight | heavy weight | large diameter |
| Weight | <=50 kg | >50 kg <=200 kg | > 200 kg <=10,000 kg | > 10,000 kg |
| Length | ≈ 1 meter | < 3 meters | < 10 meters | >10 meters |
| Deploy & recovery | one person by hand | at least 2 person using designed cart or small-size crane | a full-size crane and associated tethers | trailer and heavy-duty cranes |
| Applications | vehicle research, coastal mapping, hull inspection | oceanographic survey, environmental monitoring | seabed mapping, oil and gas survey, geophysical survey | hydro-acoustic research, defense and warfare |

The AUV industry has rapidly expanded and grown in the past two decades. There are over 200 AUVs documented in the database of Autonomous Undersea Vehicle Applications Center (AUVAC)[5]. AUVs can be categorized into four classes in term of physical dimensions. Table 1.1 summarizes the comparison of the AUVs in four categories. With limited payload allowance, small AUVs are primarily suitable for coastal oceanographic and environmental surveys using low-power scientific sensors such as conductivity-temperature-depth (CTD) sensor and oxygen optodes. Presented in [6], the Slocum underwater glider was deployed off the coast of Newfoundland, Canada, to measure dissolved oxygen levels, temperature, and ocean current using an oxygen optode, a CTD sensor, and an Acoustic Doppler Current Profiler (ADCP). In [7], the Slocum gliders were deployed off the coast of California, USA, to obtain the vertical profile of water density and chlorophyll variation over time. Large AUVs are usually equipped with multi-beam sonars and side-scan sonars for geophysical

surveying, such as seafloor bathymetry surveys presented in [8], and exploration of hydrothermal vents mentioned in [9] and [10]. In these geophysical surveys, the sonars have a high power consumption (over 30 watts) exceeding the power limitations of small-size AUVs. The extra-large AUVs are designed for national defense and warfare purpose referred as unmanned submarines. The endurance of AUVs, very important for extended field operations, is not included in Table 1.1, since it depends on the integrated sensors and their operation cycles. The endurance of a typical battery powered AUV is usually limited to several days except for Autosub (long Range version) developed by National Oceanography Centre in UK, Tethy developed by Monterey Bay Aquarium Research Institute in USA, and Autonomous Underwater Gliders (AUGs) introduced in [11] and [12]. The Autosub is a large size AUV, over 5 meters long. Its nominal speed is about 0.4 m/s with an endurance up to 6 month. The Tethy is two meters long with an endurance about 2 weeks. The AUGs are mainly driven by buoyancy pumps instead of thrusters resulting in a long endurance up to several months. With the development of underwater technology, the sensors for AUVs are becoming smaller and more energy efficient leading to a trend of using small-size AUVs for the applications that were conducted using large-size AUVs. For example, Teledyne Gavia, a light-weight AUV, was used for ice ridge measurement in [13] and [14], and seafloor survey in [15]. However, the power resources on the small-size AUV constrain the endurance when they are carrying these geophysical instruments which still have a relatively high power consumption (above 10 Watts) causing the limited endurance in several hours. We chose a small-size AUV such as Tethy and AUGs whose systems are energy optimized. But additional sensors must be integrated for iceberg mapping. The selection of sensors will be introduced in Chapter 2.

The navigation and localization of the AUVs has become a common topic in AUV op-

erations due to the lack of GPS signal beneath the ocean-surface. Many reviews ([16] to [20]) have been conducted on the available methods and technologies in underwater navigation. As discussed in [17], some of the vehicle states are directly measured using sensors while others are estimated. For instance, the vertical displacement can be accurately measured by a well-calibrated pressure sensor; while the accelerations, orientation, and angular rates are derived from magnetometers, gyroscopes, and compasses. The most challenging problem is estimating the displacements of the AUV in the horizontal plane (X and Y). Inertial-based, acoustic-based, and geophysical feature-based methods are the three techniques generally used in estimating the X-Y displacement. For the best navigational results, the operation normally incorporates the estimates from more than one of the localization methods. For example, the authors are intended to fuse inertial-based and acoustic-based methods for AUV navigation[23].

For inertial-based navigation, known as dead-reckoning, the location of an AUV is derived from double integrating the acceleration in the x-axis and y-axis while the depth is measured by a pressure sensor. The updating rate varies from one scenario to another, and it is related to the performance of the inertial measurements unit (IMU) e.g. sampling rate and accuracy. However, the estimated location deviates from its actual location due to ocean currents and measurement errors in the IMU. As a consequence, the predicted track of the AUV starts to deviate from the actual path with a bias accumulated over the distance traveled. To minimize the navigational errors, a high accuracy inertial navigation system (INS) or a Doppler Velocity Log (DVL) is needed. The DVL provides information about the vehicle's velocity over the ground [21] other than axial accelerations. Therefore, the measurement error is only integrated once in dead-reckoning causing less error accumulation problem. It is, however, not feasible for a small-size AUV, since the INS and DVL with high

accuracy come at a relatively high price and large size that is difficult to be integrated on small-size AUVs.

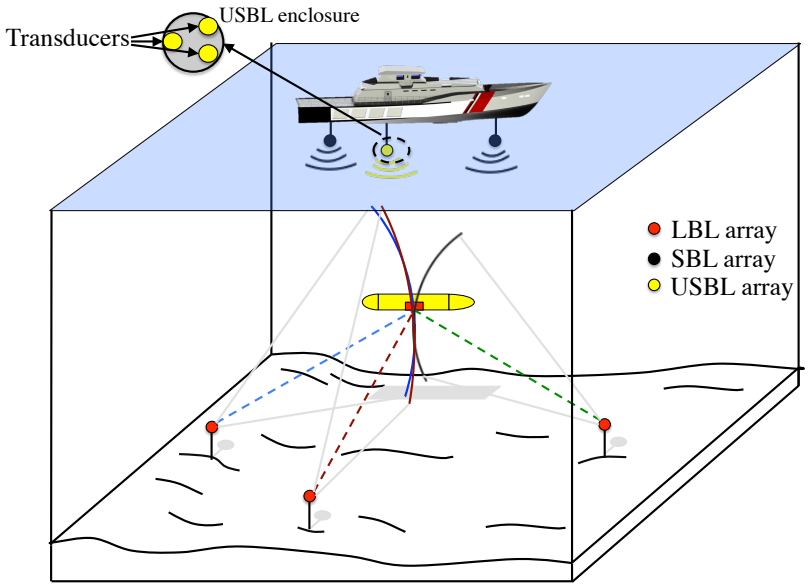


Figure 1.3: AUV navigation and localization using acoustical instruments, Long baseline (LBL), short baseline(SBL), and ultra-short baseline (USBL).

Acoustic-based navigation for AUVs is widely used in geophysical surveys where the navigation is essential for processing the measurements, i.e. measuring the sea-ice ridges [13], exploring hydrothermal vents [10], and identify shipwrecks [22]. Figure 1.3 shows the concept of navigation using acoustic transducers. The navigation package consists of an array of transceivers at known locations and a remote unit on the AUV. The transceiver at known location broadcasts acoustic signal towards the remote unit on the AUV. Once the signal is detected by the remote unit, an answer message is sent out. The range from the transceiver array to the AUV is equivalent to the distance sound travels during the time consumed in such message exchange process. With an array of transceivers, the location of the AUV is found at the intersection point of the spherical propagation from multiple transceivers. Long baseline (LBL), short baseline(SBL), and ultra-short baseline (USBL) are the most common acoustical

navigation instruments. The biggest difference between them is the distance between transceivers. The distance between the transceivers in a LBL system is usually more than 100 meters that they are normally moored on the seafloor. The transceivers in a SBL system are usually mounted under the hull of a ship with a separation distance from 10 to 50 meters. In the USBL, the transducers are extremely close that they are contained in the same enclosure and mounted under a ship. The navigational error using the acoustic approach is highly dependent on the time synchronization on these transceivers since the range is calculated from the time difference between the sound pulse emission until it received by another transceiver. Time synchronization is extremely important particularly on the USBL because the differential time is very small. Another error source of the acoustic approach is caused by the nature of sound. Because the transducer array is either close to the seafloor or near to the surface, the sound received on the AUV may not come directly from the transducer array. Instead, the sound received may coming from a location on the seafloor where the sound is reflected. Furthermore, the speed of the sound varies with the depth. The variation of sound speed causes the sound deflection between depths inducing an error in the range measurements. It is challenging to correct the errors caused by the sound speed variation because it also varies over the time. For a short period, the sound speed profile can be obtained by performing CTD casts in the vicinity of the survey area. Normally, the sound speed is assumed constant at 1500 m/s for acoustic instruments. The acoustic-based navigation are discussed and evaluated in [23] to [26].

In some areas, a prior map about the environment is available, such as a digital terrain map, a magnetic field, and gravitational anomalies. With the availability of environment information, the geophysical based navigation can be used. During the mission, AUVs sense the environment with on-board sensors, and it is intended to match the measured environment information with the stored environment map for estimating

the current location. The resulting navigation relies highly on the accuracy and the resolution of the stored map. An example of a terrain-aided navigation application on a Slocum glider is presented in [27]. Without a prior map, Simultaneous Localization and Mapping (SLAM), formerly known as concurrent mapping and localization, is used for AUV navigation. The mission begins with a stochastic map filled with unknowns. The map regularly updated with the environment sensing obtained during the mission. The AUV is then navigated in the stochastic map. Overall, the geophysical based navigation is computationally intensive because it normally requires the use of the Kalman Filter, the Extended Kalman Filter, and matching algorithms for the best result.

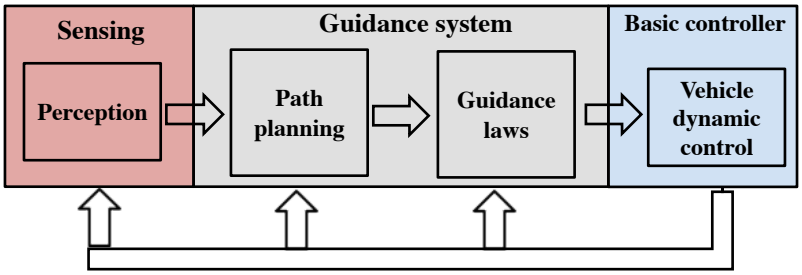


Figure 1.4: A layout of AUV control system modified from [28]

The control system is essential for the AUV to accomplish the objectives defined by the operators. Figure 1.4 shows a typical control system layout of an AUV. The AUV gains knowledge about the environment via the various on-board sensors. In a guidance system, the ideal path is planned according to the gained knowledge and predefined mission objectives. Guidance laws implemented in the guidance system generate commands to the basic controller, such as speed controller, depth controller, and heading controller, for maintaining or achieving the the desired path. The basic controller directly controls the mechanical mechanisms, e.g. thrusters and rudders, to minimize the error between the current vehicle states and the desired states from the guidance system.

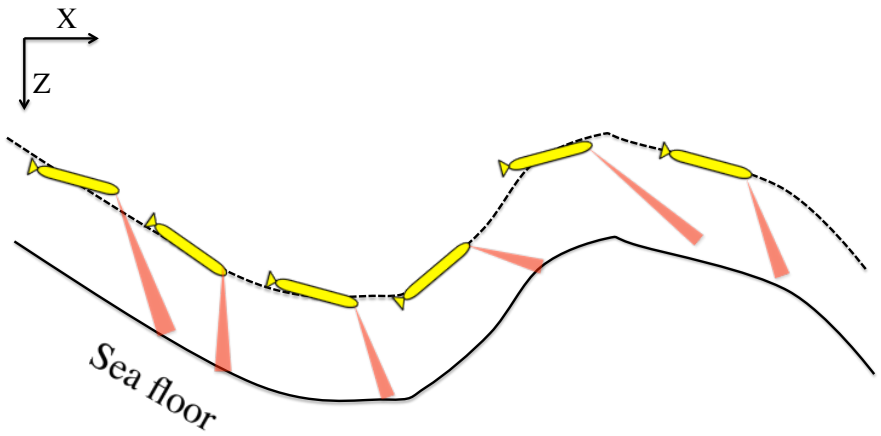


Figure 1.5: The AUV is controlled to following the seafloor at a consistent altitude.

For most survey type missions, the AUV is intended to stay at a constant distance away from the target, e.g. seafloor, to maintain a consistent sensor footprint. The bottom-following (terrain-following) has been well explored and validated on AUVs. The objective of the bottom-following is to control the AUV to maintain a fixed height above the terrain using the information from downward-looking sonars (Figure 1.5). In [29], a simple proportional-integral-derivative (PID) controller is implemented on the AUV Odyssey based on measured depth and altitude. The vehicle performed smoothly in a friendly environment that is acoustic reflective and no significant depth variation. In [30], the downward-looking sonar is modeled stochastically using the theory proposed in [31] to eliminate the uncertainties in the unknown direction of the incoming sound on the sonar. The sonar measurements are projected into a one-dimensional gridded map which generates a synthetic nonlinear elliptical force-field to control the vertical motion of the vehicle [32]. The algorithm is validated in surveying a subsea lava flow using the Autonomous Benthic Explorer (ABE), an AUV developed by Woods Hole Oceanographic Institution. In [33], a terrain-following controller is developed on Autosub 6000, a 6 meters long AUV designed in National Oceanography Centre in United Kingdom. The controller utilized the range measurements from a

Tritech SeaKing mechanical scanning sonar oriented in a forward-scanning configuration. The seafloor elevation measured by the sonar is used in a depth controller for stabilizing the altitude. The performance of the terrain-following is validated on a seafloor slope from 3000 meters to 1000 meters with a target altitude of 10 meters. In [35], a guidance system is introduced for the bottom-following mission. The linear regression is applied to the sensor readings to construct a bottom profile. By offsetting the profile with the desired altitude in bottom-following, a desired traveling path for the AUV is obtained. Then the guidance law is designed as a state feedback controller to minimize the cross-track error between the AUV and desired path. Other guidance laws in the path-following application are also available such as the line-of-sight path-following in [37] and [36], the Lyapunov direct method with the backstepping technique described in [38], and the vector-field path following mentioned in [41].

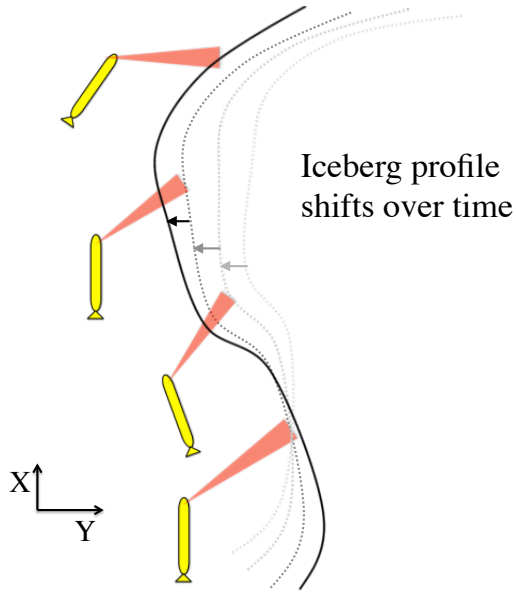


Figure 1.6: The AUV is intended to follow the moving iceberg profile at a constant standoff distance.

It is worthwhile to modify a bottom-following algorithm into a planar profile following scenario (Figure 1.6). But the difference between a terrain-following and an iceberg-

profile following application has to be considered. The terrain is generally speaking stationary while the iceberg is a moving object. Therefore, an increases of uncertainties in previous sonar readings appears since the iceberg drifts away from the location when a previous sonar measurement was taken. Moreover, the variation on the iceberg surface is larger than the seafloor terrain. Due to the deterioration and calving, sharp corners will form on icebergs. Nevertheless, the depth measurements which is used in bottom-following control have less error than the navigation error in the planar plane that is used in iceberg-profiling. Overall, a more complicated guidance system is necessary to be designed on an AUV for underwater iceberg-profiling.

## 1.3 Underwater iceberg profiling

### 1.3.1 Ship-based techniques

Atlantic Canada has a long history of tracking icebergs originating from Western Greenland. The demand for iceberg-profiling began in the early 1970s when the offshore industry started in the Canadian Atlantic Ocean. Large icebergs have a potential of colliding with offshore structures, while deep-keel icebergs have a potential of destroying subsea infrastructure such as pipelines buried on the seafloor. In order to forecast and to prevent icebergs entering the zone of offshore production, iceberg management has developed and is described in [1] and [2]. Initially, the drifting trajectories of icebergs are predicted with iceberg drifting model developed by the scientists, i.e. the dynamic model developed in [3]. While wind drag is related to the above water shape, water drag, a major factor causing iceberg translation, is determined from the cross-sectional area of the underwater portion against the ocean currents. The weight and moment of inertia that are determined from the above and below profiles are important for estimating iceberg motion when the above-mentioned

forces are applied. Thus, the underwater profile of an iceberg is critical for an accurate drift prediction. For icebergs that have the potential of entering or already entered the area of offshore production, iceberg deflection introduced in [1] and [42] is conducted to eliminate the threats. An iceberg stability study [43] has to be conducted based on the overall shape of the icebergs for selecting an appropriate deflection technique and location of applying deflection forces. Underwater profiles of the icebergs are essential for safe operations in re-directing these icebergs.

Unlike the above water iceberg profiling using LIDAR [44] and photogrammetry [45], iceberg profiling beneath the surface is challenging because light attenuates extremely fast under the water. Since 1970s, the majority of iceberg draft measurements have been conducted using acoustic technologies such as side-scan sonars and multi-beam sonars [46]. However, sound speed is very slow (about 1500 m/s) compared to the speed of light ($3 \times 10^8$ m/s). Thus the pinging rate of a sonar is usually limited to 5 Hz at a profile range of 150 meters because it takes 0.2 seconds for the sound to collide and echo back from a target that is 150 meters away. Iceberg models are constructed in correlating underwater iceberg profiles with above water features such as heights and waterline profiles. Various types of equations for estimating iceberg draft are proposed in [47], [48] and [49]. However, such models are not sufficient to provide an accurate estimate of the underwater shape of an iceberg. A typical setup of mapping the underside of an iceberg using a horizontal plane scanning sonar is shown in Figure 1.1. A tethered cylinder equipped with the sonars (see Figure 1.7), is deployed and recovered from the support vessel using a winch system. The sonar scans the iceberg sections transversely to its vertical movement, while its position is determined using acoustic transducers and dead-reckoning method. The scanning process is repeated from different angles around the iceberg to obtain a panorama view about the iceberg. Some successful trials were conducted in the past using the vertical sonar probe. In

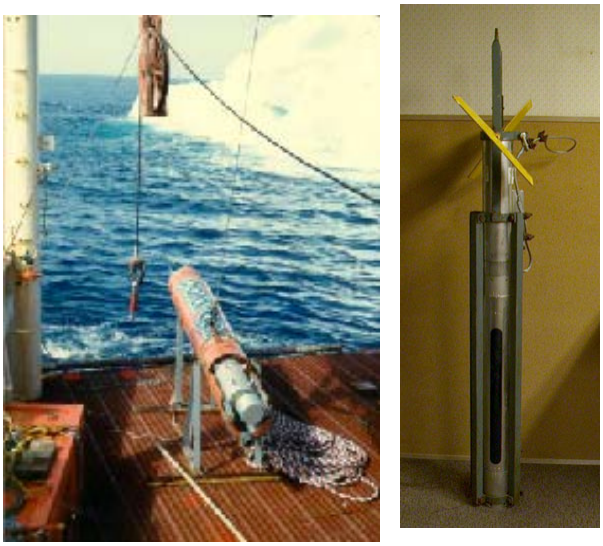

**Petro-Canada Lnc.**
**1984-1985**

**Oceans Ltd.**
**2003**

Figure 1.7: Profiling probes designed by Petro-Canada Inc. [46] and Oceans Ltd. [51].

1974, measurements from a side-scan sonar were used to generate contours of icebergs at discrete depths [50]. In 1987, a side-scan sonar was deployed from a ship near multiple icebergs on the Grand Banks off the Newfoundland to obtain vertical cross-sectional profiles [3]. In 1988, an iceberg profiler with a mechanical scanning sonar was deployed to obtain the underwater shape of an iceberg [4]. For safety concerns, the ships usually stay at least 50 meters away from the iceberg. As a result, the distance from the iceberg to the ship may exceed the maximum detectable range of the sonar at greater depth. Furthermore, due to the hydrodynamic interaction between the water and the scanning system, the profiler may rotate from its original orientation. Hence, the iceberg may be outside the field of view of the sonar.

With the developments in sonar technology over recent years, sonar systems are available now with greater range, higher sampling rate, and improved accuracy. Some recent iceberg profiling operations presented in [52] and [53] used side-mounted multi-beam sonars with a wide vertical field-of-view. The surveys were conducted by driving

the vessel at a nominal speed around the icebergs. This configuration increases the efficiency of the operation, however, this type of operation is not necessarily applicable to the icebergs with deep keels. At great depth, the majority of the energy from the sonar is deflected at the iceberg surface instead of reflected back towards the sonar that causes sensor dropouts at deep water. Moreover, the vertical coverage on the iceberg is related to the standoff distance when the vessel is circumnavigating the iceberg as shown in Figure 1.8. Thus, the mapping operation will be conducted either with lower sonar resolution (higher vertical coverage) at a further distance or higher sonar resolution (smaller vertical coverage) at a closer distance.

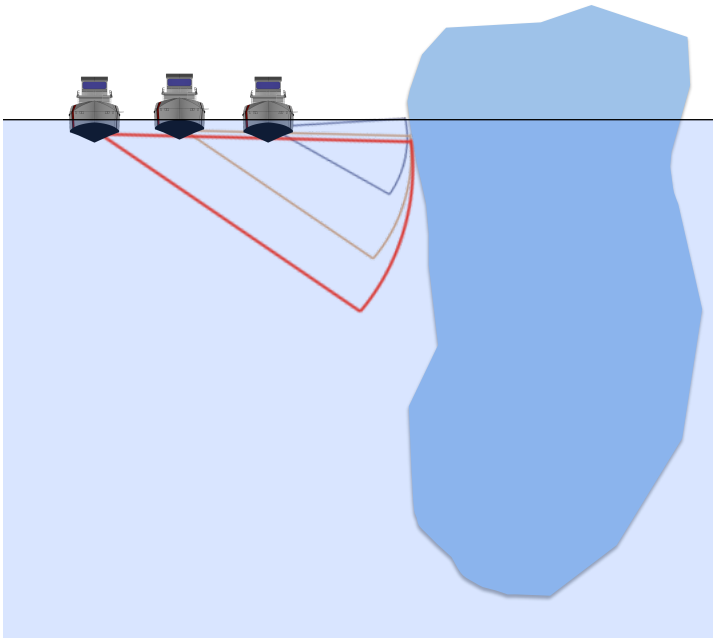

Figure 1.8: Vertical coverage of the sonar on the iceberg is increases with distance from the iceberg, although resolution declines.

In conclusion, from the review of existing methodologies, the sonar systems used are capable of detecting iceberg surfaces but the characteristics of the platforms accommodating the sonars significantly increase the complexity and cost of the mapping operation. Furthermore, the platforms can be a limiting factor for obtaining a high-

quality underwater map of an iceberg, and the environment data close to the iceberg are not accessible from the ship due to the safety concerns.

### 1.3.2 AUVs for iceberg mapping

In recent years, there has been conducted researches on using AUVs for underwater iceberg-profiling. These tether-free vehicles are capable of operating close to icebergs and maintaining a consistent sensor resolution that is critical for the instruments such as side-scan sonar and camera. In addition, AUVs allow us to gather oceanographic measurements such as water density and water circulation around icebergs for scientific studies.

Various approaches to use AUVs to profile the underside of icebergs have been made over the past decades. In [54] a Slocum glider with an upward-looking ice-profiling sonar was deployed in Greenland to travel underneath a small-size iceberg (L 30 m $\times$ W 15 m $\times$ H 4 m) for measuring the maximum draft. Presented in [53], the Teledyne Gavia AUV was deployed to travel underneath the Petermann Ice Island-B with an upward-looking multi-beam sonar. As a result, the AUV transects 700 meters under the ice island at a pre-programmed depth with the ice topography above the vehicle. The research shows that the AUV is capable of obtaining underside iceberg profile. However, without a customized guidance system, such as collision avoidance mentioned in [55], problems appeared in these applications. The Slocum glider was trapped under the iceberg in [54] and the iceberg drifted outside the view of the upward-looking sonar in some deployments mentioned in [53]. Mapping the iceberg with an AUV moving in a circular pattern, has also been proposed. The potential of spiraling around an iceberg using a Slocum glider was discussed in [56]. Consequently, a Deflectable Wingtip Mechanism (DWM) was developed to expand the maneuverability of the Slocum glider [57]. In [59] and [61], the authors proposed a method of

mapping the iceberg with the AUV circumnavigating around it. In [59], the author focused on the navigation of AUVs relative to target icebergs using measurements from a Doppler Velocity Log (DVL) and a multi-beam sonar. In [62], results of using the AUV to follow and map an underwater cliff near Monterey Bay are presented. In [63], an edge-following feature is developed and evaluated in a simulation environment for controlling the AUV to follow the iceberg surface at a standoff distance based on measurements from a horizontal-looking multi-beam sonar. Although many attempts have been made to use AUVs for iceberg surveys, improvements in iceberg-related vehicle control and navigation are necessary and essential to achieving successes in underwater iceberg-profiling using AUVs.

## 1.4 Estimating the motion of icebergs

Information about iceberg movement is important in iceberg shape reconstruction. The rolling, pitching, and heaving can be small for a stable iceberg. Therefore, icebergs are usually assumed to have three degrees-of-freedom (northward velocity, eastward velocity and rotation around a vertical axis located at the centroid). Because the locations of a survey vehicle are usually registered in a georeference coordinate system, such as Latitude-Longitude-Depth or North-East-Down, the sonar measured ranges are converted into a point cloud in the georeference frame. In order to represent the iceberg shape, the points have to be further corrected into an iceberg-attached coordinate system. Otherwise, the shape is deformed compared to the actual iceberg shape. As shown in Figure 1.9, the green and red clouds present an identical region on the iceberg. However, they do not overlapped in the North-East-Down coordinate due to the motion of iceberg. Therefore, it is necessary to correct the point cloud for the motion of icebergs to present the actual shape of icebergs.

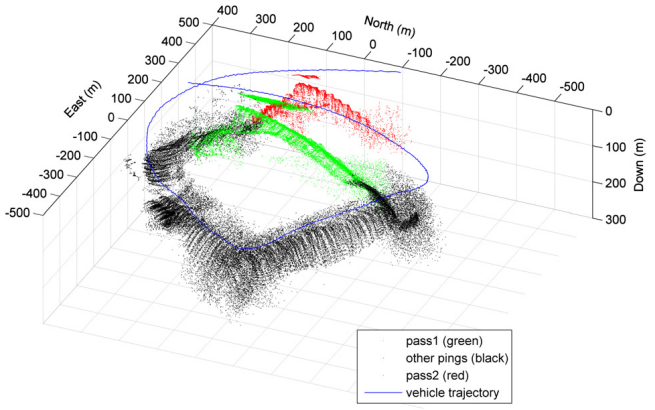


Figure 1.9: Sonar measurements obtained from the field trial presented in [59].

Satellite images were used for iceberg tracking in [64]. However, the remote sensing techniques typically have a coarse resolution resulting in an averaged motion information over an extended period. Iceberg beacons mentioned in [53] and [65] are designed for anchoring on iceberg. An iceberg beacon normally consists of a GPS module, an attitude sensor, a compass, and a communication module (radio modem or satellite modem). The information about the location and orientation reported from the sensors are transmitted to the operator via a wireless communication module. These beacons allow researchers to obtain a relatively accurate iceberg motion continuously for a short period. However, beacon anchoring only works reliably on relatively flat surfaces on stable icebergs.

Instead of directly measuring the motion on the iceberg, Figure 1.10 shows the idea of measuring iceberg motion from a surface vehicle. A ranging device, e.g. a laser range finder and a radar, is used to track the range from the vessel to a particular location (feature) on the iceberg. The trajectory of the tracking point (red line in Figure 1.10) on the iceberg can be derived from the known range measurements, the viewing angle of the ranging device, and the location of the vessel. The velocity of the tracking point is then calculated by differentiating the displacement of the tracking point over time. The resulting velocity can be represented by a linear velocity and a

rotational velocity around the centroid of the iceberg. This method was used in the iceberg field trial on CSS Dawson support vessel [3]. A total of nine icebergs were observed over a period of 6 weeks. The trajectory and velocity of the iceberg were obtained to validate an iceberg drift model. As a drawback, this method is associated with a high expenditure of utilizing the ship for an extensive period.

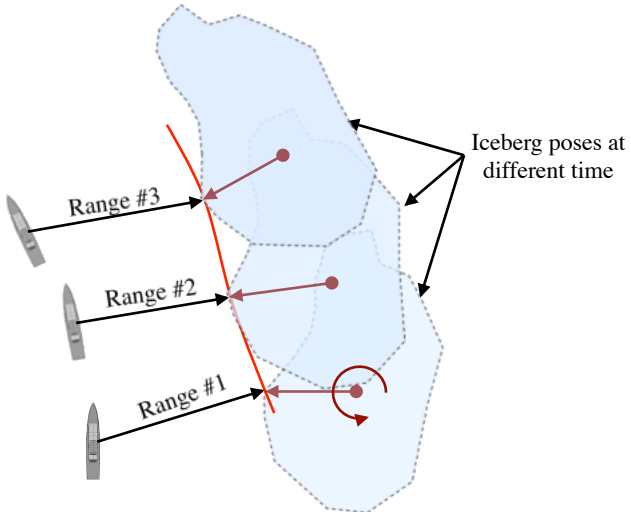


Figure 1.10: Measuring iceberg motion with a surface vessel by tracking the ranges from the vessel to a point on the iceberg.

Progress towards iceberg motion estimation using the point cloud registration is reported in [52] and [60]. The point cloud registration is a process that aligns data with an optimal translation and rotation matrices leading a minimum alignment error. A comprehensive review is conducted in [66] for further information about the development and algorithms in points cloud registration. It is widely used in object reconstruction [67] and autonomous vehicle navigation [68], e.g. the technique of Simultaneous Localization and Mapping (SLAM) introduced in [69] and [70].

The Iterative Closest Point (ICP) algorithm, first mentioned in 1992 [72], is one of the most popular algorithms used in points cloud registration. With two given 3-D shapes, the algorithm is intended to register them by minimizing the mean-square

distance with an optimal set of transformation matrices. However, this algorithm only works well in an ideal condition where outliers are not presented. The disadvantages of the algorithm in [72] is further reported in [73] that inappropriate initial transformations and low overlap ratio will cause the failure of the algorithm. An improved ICP algorithm using a statistical method based upon distance distribution to eliminate outliers is introduced in [74]. The algorithm was validated with both synthetic and real data. The improved algorithm is efficient and robust to register shapes and estimate the motion. Many variations and extensions of the algorithm have been developed based on ICP, such as the generalize ICP [76]. In order to improve the accuracy, features of the shape such as normals, curvature, and curvelet are considered in [75]. With the commercialization of laser scanner and the development of camera sensors, e.g. Microsoft Kinect$^{\text{TM}}$, many new developments in point cloud registration have appeared. Researchers are not constrained to using synthetic features generated from Computer-Aided Design (CAD), but can use real data sampled from the environment in validating their algorithms. With the rapid development of embedded systems, faster and more powerful processors have become available and affordable. Benefits from this development, point cloud registration can now be implemented on the robotic platforms for SLAM ([77] and [78]) and loop-closure detection [79] in determining the vehicle's location and orientation in an unknown but stationary environment.

Assuming the vehicle is operated in a dynamic environment with known vehicle pose (location and orientation) in an inertial coordinate system. Using the point registration and loop-closure detection, similar features within the samples captured from different period will be highlighted. The transformation matrices produced by these matching algorithms indicate the change of the environment. After the transformation, the correlated features should have a high ratio of overlap confirming the

estimated transformation. In [52], the iceberg motion is estimated by comparing the resulting cost function of the selected point clouds. The algorithm is validated on a point cloud sampled using multi-beam sonar on a tabular iceberg shown in Figure 1.9. The two point clouds at the beginning and the end of the circumnavigation are selected to be compared based on a three-dimensional predefined iceberg motion model. The averaged iceberg motion is estimated by finding a pair of velocities from the iceberg motion model yielding a minimum resulting cost. In [60], the algorithm is improved with additional measurements from a Doppler Velocity Log (DVL). By pointing the DVL towards the iceberg, the information about the vehicle's velocity relative to the ensonified terrain on the iceberg is estimated. The AUV is then intended to navigate in the iceberg-attached coordinate system. The rotation of the iceberg-attached coordinate system is estimated by applying the method in [52] to the samples from the multi-beam sonar. However, the DVL and the multi-beam sonar are not commonly available on some small-size AUVs due to the concerns about the power consumption, mechanical integration, and expenses.

## 1.5 Operational Scenario

In Atlantic Canada, ice management is required by the National Energy Board under the Canada Oil and Gas Operations Act [82] for the offshore production. Introduced in [80], ice management commonly consists of

- Ice/iceberg detection, tracking and forecasting
- Threat evaluation
- Physical ice/iceberg re-direct such as ice breaking and iceberg towing
- Procedures for disconnection of offshore structures.

As discussed in [81], visual iceberg detection using supply vessels or aircraft are commonly used on the Grand Banks. However, operations are limited by weather conditions such as fog and sea state. Marine RADAR is also used for iceberg detection and tracking, but also suffer from weather conditions and has range limitations. In [64], the authors describe the use of satellite for iceberg drift monitoring. This approach is limited to large icebergs due to its limited resolution.

Based on the existing ice-management protocol and its requirements, we identified an opportunity to incorporate a long endurance AUV in order to provide an early assessment of an iceberg threat potential, through the identification of key iceberg parameters such as maximum draft, size, and coarse shape. Such a long range AUV, a unmanned marine robot that can operate independently for weeks or months, is less constrained by weather.

As mentioned in [2], the size of the tactical zone is relevant to the iceberg drift velocities and time in physical iceberg deviation. For an iceberg with speed of 0.5 m/s, the tactical zone is about 20 km that allows ten hours for the iceberg re-direct operations. Multiple AUVs can be deployed to patrol in the tactical zone or at further range to assess icebergs. Once an iceberg is detected by marine radar or is observed by a ship, an AUV is then assigned to approach the iceberg. Based on the location provided from these sources, the AUV will plan an intercept path to approach the iceberg. During the approaching, the AUV will be directed to surface about every 30 minutes to report its current position and to accept the most recent iceberg location update in order to adjust its intercept path if necessary. Relevant research [83] has been conducted in tracking oceanographic surface drifters using AUVs with periodically updated drifter locations.

Once the AUV is in the vicinity of the iceberg, a search pattern [84] will be performed to locate the iceberg. After the iceberg is detected by the sonar on the AUV, an

underwater iceberg survey is then performed. The information about the iceberg shape and draft is then transmitted to the offshore site for a threat evaluation and for iceberg re-direction. Meanwhile the AUV continues to track the iceberg until the alert is lifted or transferred to an iceberg management vessel.

This thesis is focused on developing an AUV-based iceberg mapping technique. It describes a solution for AUV-based iceberg mapping using small-size and long endurance AUV. The development of an autonomous control system and an iceberg reconstruction method show the potential to measure and report key iceberg parameters in a automated process. Discussed in the field trials in Chapter 4, the iceberg approaching phase was conducted using a rigid-hull inflatable boat that brought the AUV into the proximity of the target iceberg. This approaching phase will be automated as a future development using periodic location updates of the iceberg position.

## 1.6 Overview of the thesis

### 1.6.1 Objectives and contributions

The AUV-based iceberg-profiling technique is first evaluated by comparing the results from a conventional vertical sonar-probe-based in a constructed simulation environment. The evaluation is focused on the outcomes, such as accuracy and time, from different survey patterns used in two techniques with the identical sonar configuration. The results from this assessment will provide important information in designing and improving the GNC development. For assisting the ice management on the Grand Banks in Eastern Canada, the AUV is capable of tracking and mapping iceberg at a further distance away from the offshore platform where it is outside the detection range of the radars and there is no support vessel in the vicinity. Moreover, the AUV operation is not constrained by severe weather condition, e.g. high sea-state that is

risky for ship operation. Nevertheless, the AUV can stay closer to the iceberg than a manned ship for collecting environment information, i.e. water circulations and water density near the iceberg. However, the AUV operation is challenging due to the limitations on underwater navigation and the development on the autonomous control using on-board sensors (see Section 1.2).

A Guidance Navigation and Control (GNC) system for automating the iceberg survey is developed for the AUV based on the experience from a simulation environment and actual field deployments. The GNC is intended to guide the AUV to follow the iceberg profile at a standoff distance without collision during the mission. With the field validation shown in Chapter 4, this GNC makes a significant contribution to the development of autonomous control on the AUV. The designed GNC is easily adaptable for other AUVs with existing basic vehicle control, e.g. heading controller. The GNC is also applicable on other applications such as underwater infrastructure survey and autonomous dam survey. More importantly, the GNC is capable of guiding the vehicle to circumnavigate a non-stationary object. Therefore, the GNC shows the potential for implementation on aerospace robots for planetary exploration.

An algorithm based on the point registration is developed and is introduced in Chapter 5 for estimating the iceberg motion. The algorithm estimates the iceberg motion by finding two overlapped sonar measurements on the iceberg. As a consequence, the iceberg shape is reconstructed with the sonar measurements adjusted for the iceberg motion. In an AUV-based iceberg-profiling operation, multiple revolutions at different depths are required to cover the overall shape of a deep-keel iceberg. The algorithm could be implemented on an AUV to trigger a loop-closure notification that instructs the AUV to adjust its depth progressively obtaining the overall underwater shape. Furthermore, this algorithm is also applicable on a rapid iceberg profiling system conducted by a ship [85] in iceberg reconstruction.

### 1.6.2 Thesis outline

**Chapter 1**

Literature review is conducted on AUV technology, techniques for underwater iceberg mapping, and estimating the iceberg motion. Additionally, the objectives and major contributions of this thesis are also summarized.

**Chapter 2**

The experimental framework and instruments used in this research are introduced. The discussion about the usage of the instruments and processing procedures of the sensors are introduced.

**Chapter 3**

An iceberg profiling simulator is presented. The simulator consists of a sonar model, an iceberg model, and a vehicle model to verify the sampling strategies on different platforms and to develop and adjust the control algorithm. The AUV-based iceberg mapping is compared with the conventional vertical profiling probe based on the simulation result.

**Chapter 4**

The development of a guidance, navigation, and control (GNC) system is presented with the evaluation in the simulated environment and the field studies. The system is intended to steer the vehicle autonomous at a standoff distance without collisions when surveying the underside of icebergs. Details of the the GNC design and results are presented and discussed.

**Chapter 5**

An algorithm based on the point registration is presented for estimating the iceberg motion. The algorithm is validated with the simulated data and field data. Using the estimated iceberg motion, the iceberg surface is reconstructed from the sonar measurements.

**Chapter 6**

The research is summarized highlighting the achievements of the research. An outlook is also included for future researchers in the area of iceberg mapping and vehicle autonomy.

**Appendix**

The content in Appendix A.1 includes the basic coordinate system transformation in processing the sonar measurements. The process of iceberg reconstruction using the available functions in the MATLAB$^{TM}$ is also included in A.2. The resulting point clouds obtained in verifying the sampling strategies in Chapter 3 are also summarized in Appendix A.3.

# Chapter 2

# Experimental framework and instrumentation

In this research, iceberg-profiling capability will be developed based on deploying a Slocum underwater glider to survey an iceberg. The Slocum glider is intended to circumnavigate an iceberg automatically using sonar measurements from a integrated mechanical scanning sonar. The underwater location of the Slocum glider is estimated using a model-based dead-reckoning method with orientation measured by a compass and attitude sensors. The parameters for the model are calibrated using data from an underwater modem to improve navigation performance. A multi-beam sonar is used to map the underside of a floating iceberg. A set of field data is collected to validate the algorithm for estimating the iceberg motion. The configuration for the sensors and data processing are presented in this chapter.

## 2.1 Slocum underwater glider for underwater iceberg profiling

The Slocum underwater glider is a small AUV that is about two meters long and 1 meters wide with wings installed. Normally, it travels in a sawtooth pattern in the water column driven vertically by a buoyancy pump in the forward section [11]. It is chosen to be the primary platform used for this research. It has a significant advantage in endurance. The alkaline battery pack lasts weeks while a lithium battery pack can last up to several months. More importantly, the Slocum underwater glider is convenient and low-cost for deployment and recovery. It can be easily deployed by two people from a rigid-floor inflatable craft. The vehicle is controlled on-shore via 900 MHz radio frequency modem (within several kilometers) or via satellite-based iridium modem [86]. With the mentioned advantages, the Slocum glider is suitable for continuously monitoring iceberg shape changes over an extensive period that is controlled by the operators remotely through a satellite link.

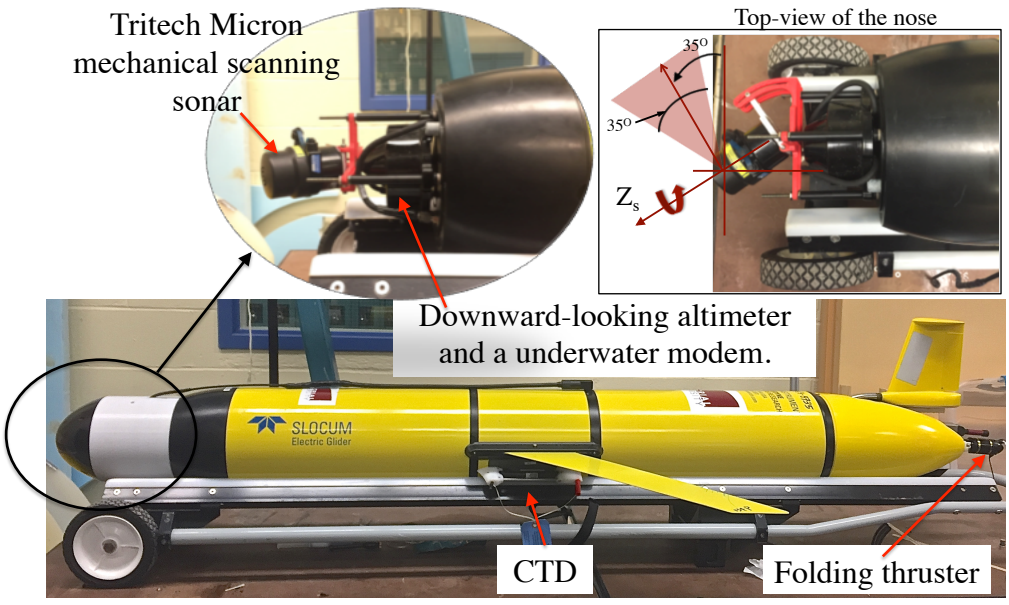


Figure 2.1: The Slocum underwater glider modified for underwater iceberg profiling

For the purpose of underwater mapping and profiling, a Slocum underwater glider has been modified in the Autonomous Ocean Systems Laboratory (see Figure 2.1). In the nose, a Tritech Micron mechanical scanning sonar is installed in a free-flooded acoustically transparent extension section (white section shown in Figure 2.1). The rigidity of the extended section is tested in a pressure chamber by applying a pressure equivalent to the water pressure at the water depth of 200 meters. A minor weight change of about 4% (16 grams) of the overall weight (400 grams) is found due to the water penetration into the structural pores. Such a weight change can be compensated by the buoyancy pump on the vehicle which has a range of about $\pm 250$ grams. The sonar is mounted on a tilting plate allowing adjustment of its forward-looking angle on the starboard side. The sonar is controlled to scan about the $Z_s$ axis and has a beamwidth of 35 degrees shown in the top view (Figure 2.1), The forward-looking angle is configured at 35 degrees for this sonar to detect iceberg profile variation in front of the vehicle. The forward-looking angle provides a nominal forward-looking distance about 40 meters that is twice the range of the minimum turning radius of the glider. Furthermore, an acoustic modem is integrated for improving the underwater navigation if paired with an acoustic navigation and communication system from the surface that measures the range together with azimuth angle and elevation angle to the vehicle. Thus, the location of the glider can be determined from known locations of the surface unit measured by a Global Positioning System (GPS). It provides an alternative source for underwater navigation besides the default method, model-based dead-reckoning. Beyond that, two-way communication can be implemented for multi-vehicle co-operation in the future. Finally, the iceberg-profiling glider is equipped with a thruster for level-flight at a higher surge speed, and a Conductivity-Temperature-Depth sensor under the wing on the mid-section.

During the deployment, the Slocum glider follows a mission script uploaded by the

user. In gliding mode, a buoyancy pump in the front section of the vehicle extends and retracts to alter the buoyancy and the pitch angle of the vehicle. Such changes causes a longitudinal speed that can be separated into a forward speed and a vertical speed. The glider repeats the motion of diving to a target depth and then climbing to another shallower depth until a surface event occurs. The surface event can be triggered by a watchdog timer, reaching a waypoint or an exceeded number of device errors. In hovering mode, the thruster is used to propel the vehicle. The vehicle is controlled to travel horizontally at a nominal depth within a tolerance zone up to the maximum operational depth. Within the tolerance zone, the desired depth and desired pitch angle are maintained by sliding a battery pack inside the front section. Once the vehicle depth is outside the tolerant zone, the buoyancy pump is engaged for major depth corrections.

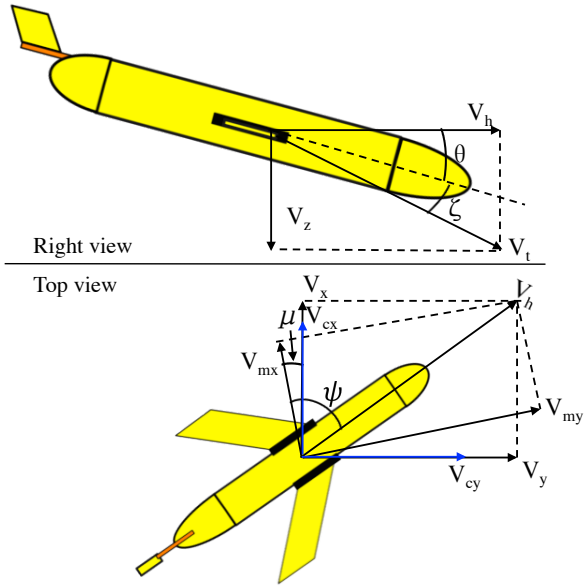


Figure 2.2: Velocity components defined in dead-reckoning.

Navigational accuracy is critical in an underwater survey. Conventionally, the position of the Slocum glider is estimated based on dead-reckoning. The underwater position

is derived by integrating the vehicle velocities over time from a known location. The vehicle velocity vector is composed of a measured vertical velocity, i.e. depth change rate, and the horizontal velocities derived using a simplified glider model with measured vehicle attitude and an assumed angle of attack. As shown in Figure 2.2, $V_z$ is estimated by differentiating the depth measurements from a pressure sensor on the glider. The horizontal velocity is then calculated using Equation 2.1 where the pitch angle ($\theta$) is measured by the attitude sensor, and the angle of attack ($\zeta$) is assumed to about 4 degrees. Then, $V_h$ is separated into two components ($V_{mx}$ and $V_{my}$) pointing towards magnetic east and magnetic north derived using the yaw angle from a compass (Equation 2.2). Using the information of magnetic declination ($\mu$), the angle between the magnetic north and true north, $V_h$ also can be divided into $V_x$ and $V_y$ pointing in the directions of true northing and easting (Equation 2.3). Here, the yaw angles (headings) are referred relative to the true north that is corrected from the magnetic north using the local magnetic inclination.

$$V_h = V_z / \tan^{-1}(\theta + \zeta) \tag{2.1}$$

$$\begin{bmatrix} V_{mx} \\ V_{my} \end{bmatrix} = \begin{bmatrix} \cos(\psi) & -\sin(\psi) \\ \sin(\psi) & \cos(\psi) \end{bmatrix} \cdot \begin{bmatrix} V_h \\ 0 \end{bmatrix} \tag{2.2}$$

$$\begin{bmatrix} V_x \\ V_y \end{bmatrix} = \begin{bmatrix} \cos(\psi) & -\sin(\psi) \\ \sin(\psi) & \cos(\psi) \end{bmatrix} \cdot \begin{bmatrix} \cos(\mu) & -\sin(\mu) \\ \sin(\mu) & \cos(\mu) \end{bmatrix} \cdot \begin{bmatrix} V_h \\ 0 \end{bmatrix} \tag{2.3}$$

There are, however, two drawbacks in the existing dead-reckoning calculation on the Slocum glider. First, the effect of the unknown environmental conditions, such as an ocean current, is not considered. This causes an accumulated bias between the dead-reckoned position and the actual position. Such a bias can be compensated in the

post-processing by assuming a consistent ocean current ($V_{cx}$ and $V_{cy}$) equals the bias of the dead-reckoned surfacing location and the actual surfaced location measured from a GPS divided by the time the vehicle had submerged. The assumed ocean current is included in the dead-reckoning to re-estimate the location in Equation 2.4. Figure 2.3 shows the comparison between the trajectory from the dead-reckoned location during the mission and from the re-estimation including the ocean current.

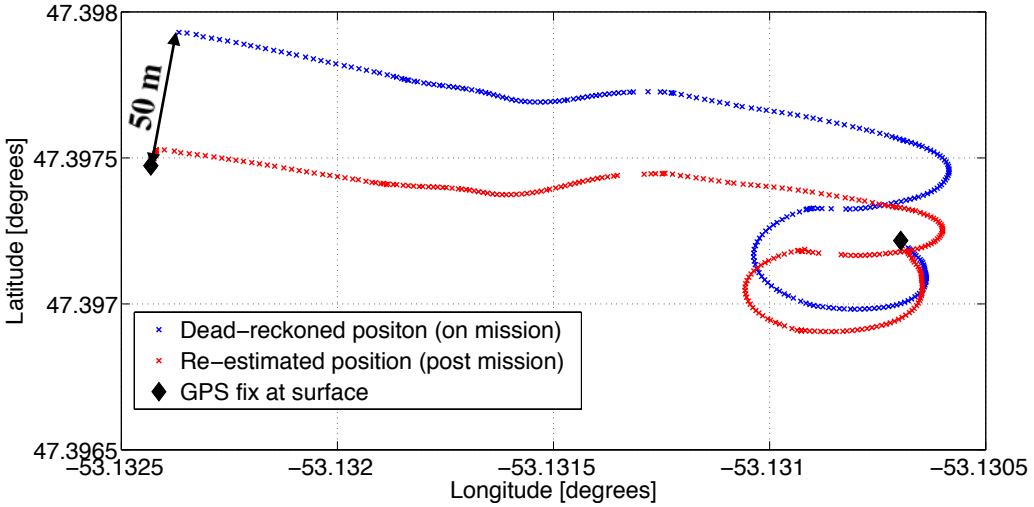


Figure 2.3: Comparing the trajectories from the dead-reckoned location during the mission with the re-estimated trajectory including the ocean current.

$$\begin{bmatrix} x_v(t) \\ y_v(t) \\ z_v(t) \end{bmatrix} = \begin{bmatrix} \int_0^t V_x dt \\ \int_0^t V_y dt \\ \int_0^t V_z dt \end{bmatrix} + \begin{bmatrix} \int_0^t V_{cx} dt \\ \int_0^t V_{cy} dt \\ 0 \end{bmatrix} + \begin{bmatrix} x_v(0) \\ y_v(0) \\ z_v(0) \end{bmatrix} \tag{2.4}$$

For a more precise dead-reckoning approach, a dynamic model of the glider introduced in [127] and [128] can be implemented. Instead of using a static model to estimate the velocity components, the influence of hydrodynamic forces (drag and lift) and hydrodynamic moments are considered. The water current can be estimated using an Acoustic Doppler Current Profiler (ADCP) and a Doppler Velocity Log (DVL). An ADCP measures the water velocity relative to the vehicle, while a DVL measures the

vehicle velocity relative to the seafloor.

Another drawback in the dead-reckoning is that the horizontal velocity cannot be calculated directly from Equation 2.1 when the spinning thruster induces an additional longitudinal force. Currently, the forward speed of the vehicle ($u$) under propulsion is estimated from the current feedback of the motor controller in Equation 2.5, where $C_2$, $C_1$ and $C_0$ are constants. In level-flight, the vehicle is assumed neutrally buoyant. The vehicle motion is assumed to have been induced by the propeller with a forward speed ($u$) in the vehicle's longitudinal direction. The $V_x$, $V_y$, and $V_z$ then can be obtained from Equation 2.6 where $\mathbf{R}_v^e$ is the rotation matrix from the vehicle coordinate to the inertial coordinate system, a function of the roll, pitch and yaw angle of the vehicle. In my research, a customized thruster is installed that produces a higher forward speed at lower current. Therefore, the surge speed, $u$, given by Equation 2.5, will initially be estimated in the open water with an acoustic underwater modem.

$$u = C_2 \cdot I^2 + C_1 \cdot I + C_0 \tag{2.5}$$

$$\begin{bmatrix} V_x \\ V_y \\ V_z \end{bmatrix} = \mathbf{R}_v^e \cdot \begin{pmatrix} u \\ 0 \\ 0 \end{pmatrix} = (R_\phi \cdot R_\theta \cdot R_\psi)^T \begin{pmatrix} u \\ 0 \\ 0 \end{pmatrix} \tag{2.6}$$

## 2.2 USBL/underwater modem

The Teledyne Benthos USBL/underwater modem is used to improve the navigation of the Slocum glider. The system consists of a transceiver mounted on a surface vessel and a remote transducer integrated into the glider. Figure 2.4 shows a typical configuration of the underwater modem. The slant range is calculated based on the time-of-flight that a message is transmitted from the transceiver until a message from

the remote transducer is received excluding the time cost for signal processing on the electronics board. Besides the slant range, the azimuth angle ($\beta_1$) and elevation angle ($\beta_2$) are also estimated based on the phase shift of the signal caused by the differential arrival time at separate receiving elements of the surface unit. With the known location from the GPS on the surface vessel and the orientation of the transceiver from the integrated compass and attitude sensor, the location of the glider can be resolved. Two-way communication is also available on this underwater modem. The resolved location can be transmitted from the surface unit to the glider to update the dead-reckoned locations.

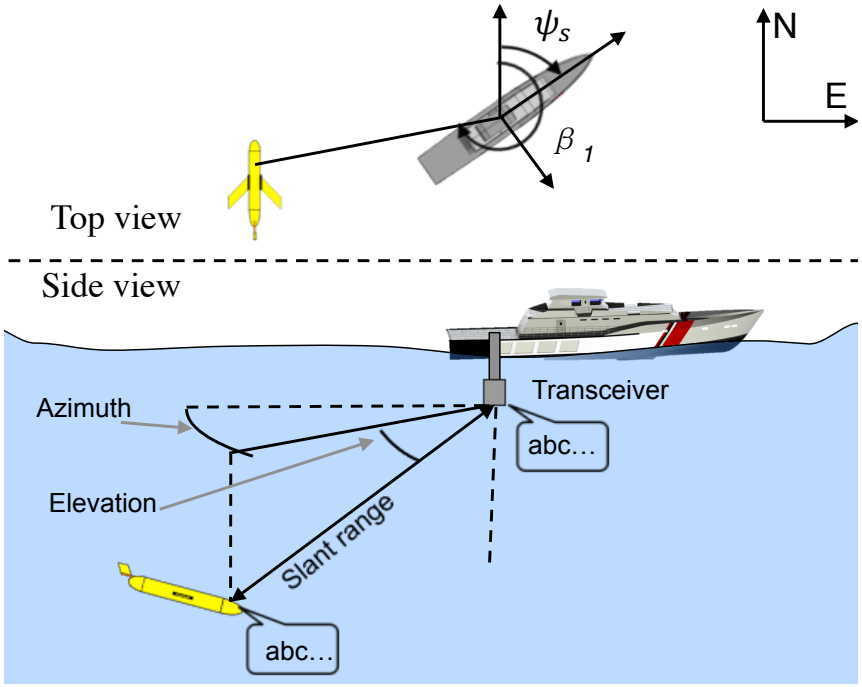


Figure 2.4: The underwater modem is not limited in locating the vehicle, it also allows the two-way communication between the surface unit and the remote unit.

The x-y location of the vehicle in the earth-referred coordinate system is computed from Equations 2.7 to 2.8. Equation 2.7 is used to convert the slant range ($R_t$) into a point relative to the surface transceiver where $\beta_1$ and $\beta_2$ are the azimuth

angle and elevation angle, and $\psi_s$ is the yaw angle of the surface transceiver. Then, Equation 2.8 is applied to convert the $\mathbf{P}_t^v$ into the Universal Transverse Mercator (UTM) coordinate system, where $[X_s(t), Y_s(t), Z_s(t)]^T$ is the location of the surface transceiver in the UTM coordinate system and $\mathbf{R}_v^e$ is the rotation matrix based on the orientation of the transceiver. The elements in $\mathbf{R}_v^e$ can be found in Appendix A.1. $[x_v(t), y_v(t), z_v(t)]^T$ can be further converted from the UTM coordinate system into latitude and longitude [87].

$$\mathbf{P}_t^v = R_t \cdot \cos\beta_2 \cdot \begin{bmatrix} \cos(\beta_1 - \psi_s) \\ \sin(\beta_1 - \psi_s) \\ 1 \end{bmatrix} \tag{2.7}$$

$$\begin{bmatrix} x_v(t) \\ y_v(t) \\ z_v(t) \end{bmatrix} = \mathbf{R}_v^e \cdot \mathbf{P}_t^v + \begin{bmatrix} X_s(t) \\ Y_s(t) \\ Z_s(t) \end{bmatrix} \tag{2.8}$$

Initially, two deployments were conducted to evaluate the performance of the underwater modem. The Slocum glider was programmed to settle on the seafloor at a depth of 40 meters, while the transceiver is attached to the surface vessel traveling in straight-line and circles.

Figure 2.5 shows the resolved location of the glider from this two tests. The red line shows the GPS location of the surface vessel. The black circles display the potential location of the glider with a measured slant range and elevation angle. The azimuth angle ranges from 0 to 360 degrees. Since the glider is stationary on the seafloor, the location of the glider is indicated at the intersection of the circles. In comparison, the blue diamonds are the location of the glider resolved from the azimuth angle measured from the surface transceiver. The resolved locations from the measured azimuth angles are distributed near the intersection point of the black circles although a few outliers

are detected. The results indicate that the location of the Slocum glider can be resolved from the underwater modem. Measurement inaccuracies might be caused by the multipath that the sound is deflected on the seafloor near the glider and deflected on the water surface near the surface vessel.

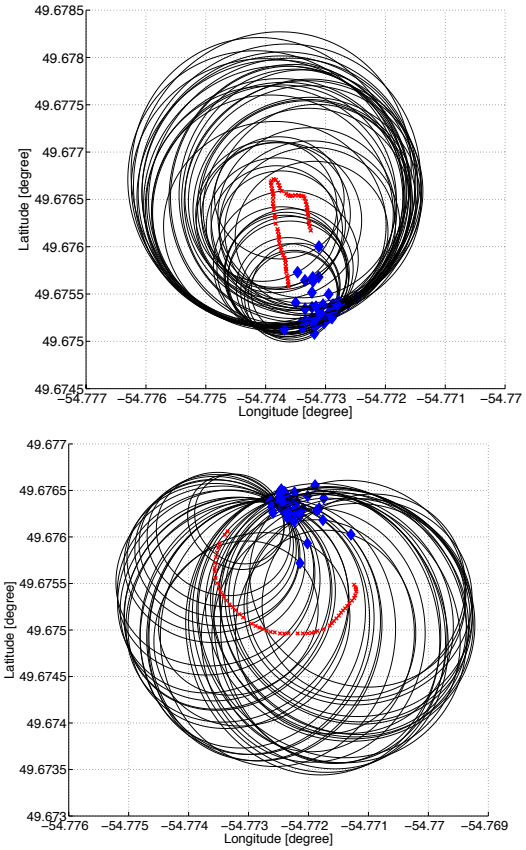


Figure 2.5: The surface vessel (red dots) was moving in the straight line pattern (top) and circular pattern (bottom) when the glider is landed on the seafloor. The blue dots are the resolved location using the estimates (relative range, azimuth angle and elevation angle) from the acoustical transceiver. The black circles displays the potential location of the vehicle without knowning the azimuth angle. For each grid, the horizontal distance is about 72 meters and vertical distance is about 55 meters.

A deployment was conducted in June 2016 to estimate the averaged surge speed during the horizontal flight. The acoustic modem is used to derive the underwater location of the glider. Since the low power thruster controller is still under development, we only operate the thruster at one desired RPM that has the lowest possibility of stalling

the thruster. Figure 2.6 shows the ideal vertical profile of the glider in a level-flight mission. The thruster will only be switched on from time $t_{h0}$ to $t_{c0}$. In the planar view, $(X_0, Y_0)$ gives the last known GPS fix before it dived below the surface, while $(X_t, Y_t)$ gives the first known GPS fix after the glider climbed to the surface. Figure 2.7 shows the actual vehicle performance during deployment. During the horizontal flight, the buoyancy pump stays at the same location to maintain the vehicle at neutrally-buoyant state. The offset in the buoyancy pump is caused by the small mis-trim in ballasting the vehicle. The vehicle is slightly negative buoyant when the buoyancy pump is at the neutral position (0 cc). The pitch of the vehicle in level-flight is controlled by moving the forward pitch battery with a PID controller. The pitch angle is found to oscillate about the desired pitch angle of zero degree. Due to the none-zero pitch, the depth of the vehicle oscillate around the target depth (11 meters) with a standard deviation of about 0.8. The depth change is mainly caused by the longitudinal speed induced by the thruster at non-zero pitch angle.

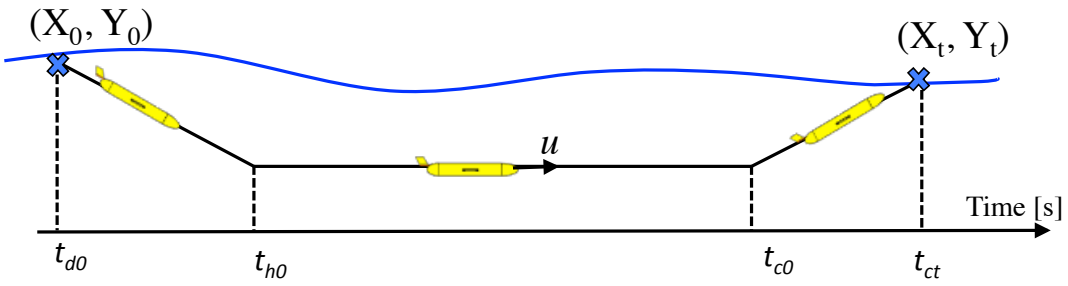


Figure 2.6: Vertical profile of the glider in a level-flight (bathtub) mission.

Here, we assumed the model-based dead-reckoning in diving and climbing is relative accurate in the absence of an ocean current. Then, the vehicle is assumed neutrally buoyant during the level-flight from time $t_{h0}$ to $t_{c0}$ as shown in Figure 2.6. As a result of the above assumptions, Equation 2.9 is obtained in the horizontal plane $(X_e - Y_e)$ where the horizontal displacement of the vehicle is calculated by integrating

the northing and easting velocities at a rate d$t$. Finally, the vehicle is assumed to have a constant longitudinal speed ($u$) in level-flight. Equation 2.9 then can be simplified and organized as shown in Equation 2.10 where we have two equations to resolve the longitudinal speed, $u$.

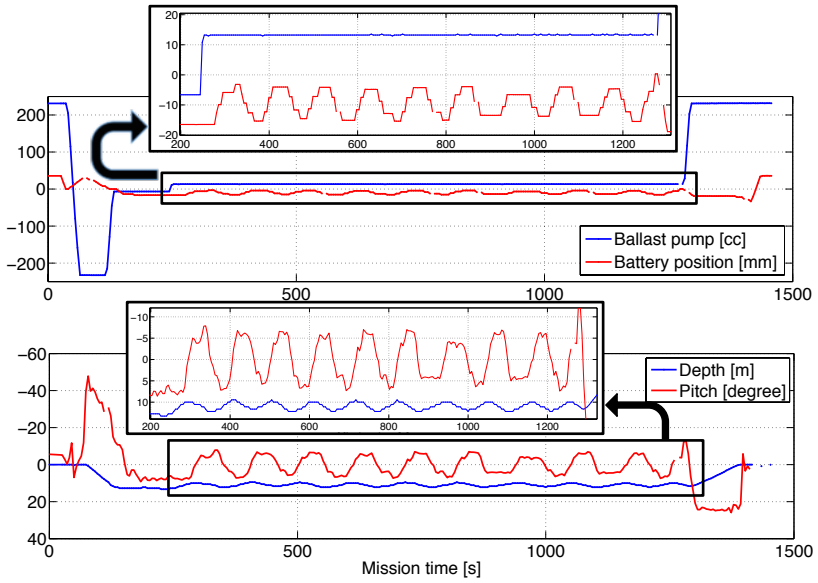


Figure 2.7: Performance of the vehicle during the deployment in June 2016.

$$\begin{pmatrix} X_t \\ Y_t \end{pmatrix} = \begin{pmatrix} X_0 \\ Y_0 \end{pmatrix} + \int_{t_{d0}}^{t_{h0}} \begin{pmatrix} V_x(t) \\ V_y(t) \end{pmatrix} \mathrm{d}t + \int_{t_{h0}}^{t_{c0}} \mathbf{R}^{e}_{v,t} \cdot \begin{pmatrix} u \\ 0 \end{pmatrix} \mathrm{d}t + \int_{t_{c0}}^{t_{ct}} \begin{pmatrix} V_x(t) \\ V_y(t) \end{pmatrix} dt \quad (2.9)$$

$$\begin{aligned} u \cdot \int_{t_{h0}}^{t_{c0}} \begin{pmatrix} \cos(\psi)\cos(\theta) \\ \sin(\psi)\cos(\theta) \end{pmatrix} \mathrm{d}t \quad &= \left( \begin{pmatrix} X_t \\ Y_t \end{pmatrix} - \int_{t_{c0}}^{t_{ct}} \begin{pmatrix} V_x(t) \\ V_y(t) \end{pmatrix} \mathrm{d}t \right) \\ &- \left( \begin{pmatrix} X_0 \\ Y_0 \end{pmatrix} + \int_{t_{d0}}^{t_{h0}} \begin{pmatrix} V_x(t) \\ V_y(t) \end{pmatrix} \mathrm{d}t \right) \end{aligned} \quad (2.10)$$

Applying the collected data from the deployment shown in Figure 2.7 into Equation 2.10, two solutions for the longitudinal speed ($u$) are found to be 0.6675 m/s and

-0.5085 m/s. Since $u$ has to be positive, 0.6675 m/s is selected as the averaged longitudinal speed induced by the thruster in horizontal flight. Figure 2.8 shows the resolved trajectories from different sources. The red track shows the dead-reckoned trajectory using the default model (Equation 2.5) that applies to the thruster designed by the manufacturer. A large location error is found between the end point of the red track and the surface GPS fix. The green track shows the dead-reckoned trajectory based on the averaged longitudinal speed of 0.6675 m/s obtained from Equation 2.10. The blue track is corrected from the green track by assuming the error between the surfacing GPS and the end point of green track is caused by a constant ocean current. The blue crosses are the resolved location of the glider using the acoustic modem. Figure 2.8 shows the dead-reckoned track with an averaged speed of 0.6675 m/s, better agreements with the acoustic modem measurements than the track generated with the default estimated speed.

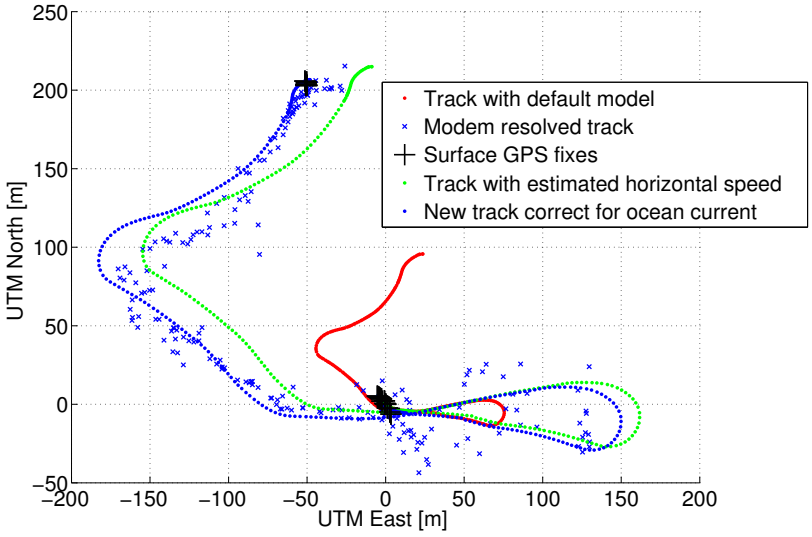


Figure 2.8: Comparison of the resolved trajectories

Using the vehicle track measured by the acoustic modem, the georeference horizontal speed of the vehicle can be extracted. Figure 2.9 shows the comparison between the horizontal speed extracted from the track measured by the acoustic modem, and

the horizontal speed calculated based on the averaged longitudinal speed $u$=0.6675 m/s corrected for the pitch angle. The horizontal speed is only calculated when the thruster is running. At the begining of the level-flight, the horizontal speed is large and unsettled. It is caused by the noisy measurements from the modem that are observed at the beginning of the deployment at the Southeast corner in Figure 2.8. From time 700 to the end of the horizontal flight, the extracted horizontal speed from the acoustic modem agrees with the speed from the estimated longitudinal speed of 0.6675 m/s.

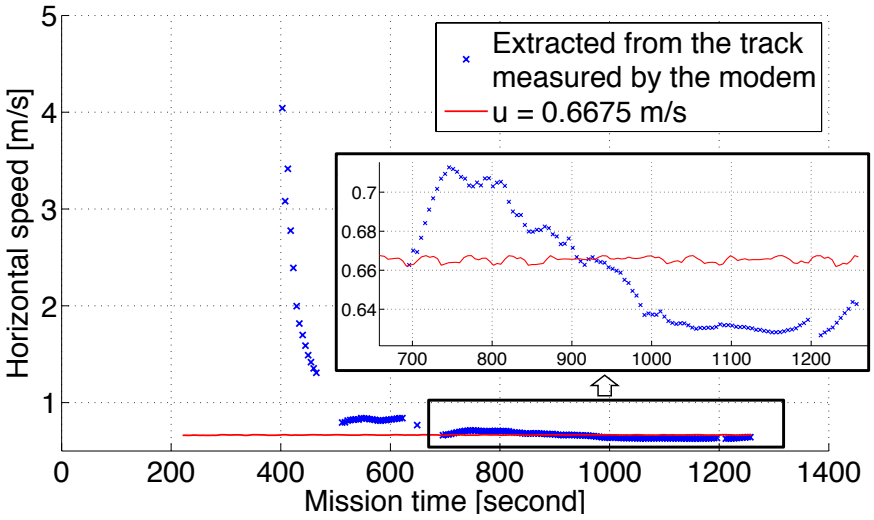


Figure 2.9: Comparison of horizontal speed from the track measured by the modem and from Equation 2.10. The zoom-in plot shows the agreement on the horizontal speed obtained from two sources.

For the remainder of this thesis, the navigation of the Slocum glider in the field trial is resolved with the constant longitudinal speed of 0.6675 m/s in level-flight. For a future implementation, the low power thruster controller has to characterized and modeled from a thruster test in a controlled environment, e.g. flume tank. A relation between the current feedback and propelling force will be drawn to estimate the parameters in Equation 2.5.

## 2.3 Mechanical scanning sonar

The Tritech Micron mechanical scanning sonar is selected to be integrated on the Slocum glider. It provides denser data than a fixed-angle single-beam sonar, and has advantages in size, processing power, and beam steering capabilities than multi-beam sonar. Thus, the sonar measurements are not limited for controlling the vehicle but also for mapping the iceberg. The Tritech Micron mechanical scanning sonar uses the Compressed High-Intensity Radiated Pulse (CHIRP) that provides clear target resolution [88]. The sonar has a beamwidth of 35 degrees along its longitudinal direction and 3 degrees in the direction of the scanning sector.

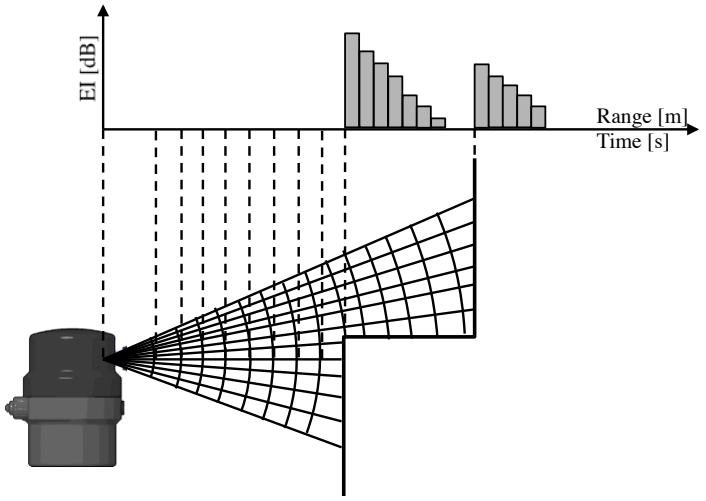


Figure 2.10: The sonar produces the received sound intensity at ranges, however, the angle of the received sound is not available.

Most of the sound energy is transmitted within the beamwidth as shown in Figure 2.10. The sonar records the echo intensity at incremental ranges equivalent to the time-of-flight at a speed of sound of 1500 m/s. The echo intensity distribution over the range is then exported from the sonar.

Shown in Figure 2.11, the sonar produces 400 data points to display the echo intensity at range intervals from the sonar to the maximum profiling range. At index j, the

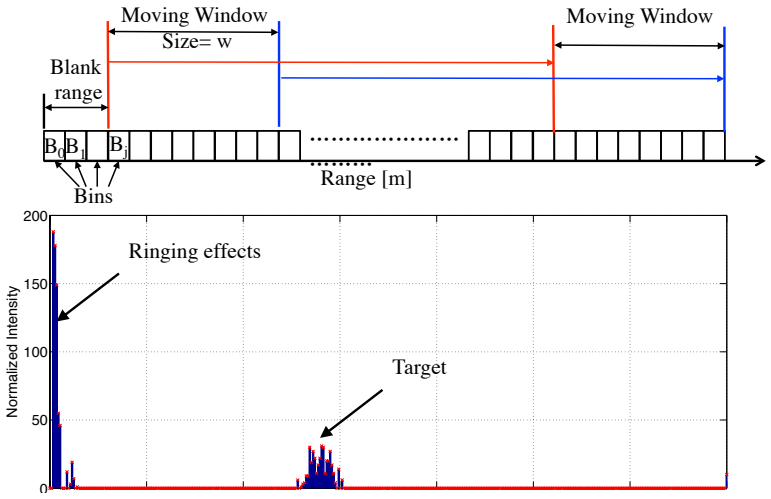


Figure 2.11: An example of sonar output as a distribution of normalized echo intensity over the range (bottom), and how to extract range from the distribution (top)

echo intensity is defined as $B_j$. The data points within the blank range are ignored due to the ringing effect of the device [89]. The blanking range is affected by the sonar electronics and the surrounding structure to which the sonar is attached. As a result of the ringing effect, a high peak in echo intensity at a close range is normally observed (see Figure 2.11). Therefore, only the data points beyond the blanking range are processed to extract the range from the sonar to a detected target. A moving window with a width of $w$ is introduced in extracting the range from the intensity distribution. The moving window scans through the data points and calculates the summation ($S_j$) within the window in Equation 2.11. Then the $S_m$ is found with $m$ leading to a maximum value of $S_j$ (see Equation 2.12). The index $n$ of the local maximum from $B_m$ to $B_{m+w}$, is then found in Equation 2.13. The Range, $R_t$, is calculated using Equation 2.14 where $R_s$ is the profiling range of the sonar. Assuming the returned sound is coming from the center of the beamwidth, a measured range can be converted into a point relative to the vehicle, $\mathbf{P}_t^v$. Using the information about the vehicle's location and orientation, $\mathbf{P}_t^v$ can be further converted into a point in the inertial coordinate, $\mathbf{P}_t^e$. The details of the transformation are introduced in A.1. The

uncertainty induced by the assumption that the returned sound is coming from the center of the beamwidth is analyzed and discussed in Chapter 4.

$$S_j = \sum_{j}^{j+w} B_j \tag{2.11}$$

$$m = argmax_{j\epsilon[0,400]}(S_j) \tag{2.12}$$

$$n = argmax_{j\epsilon[0,w]}(B_{m+j}) \tag{2.13}$$

$$R_t = \frac{m+n}{400} R_s \tag{2.14}$$

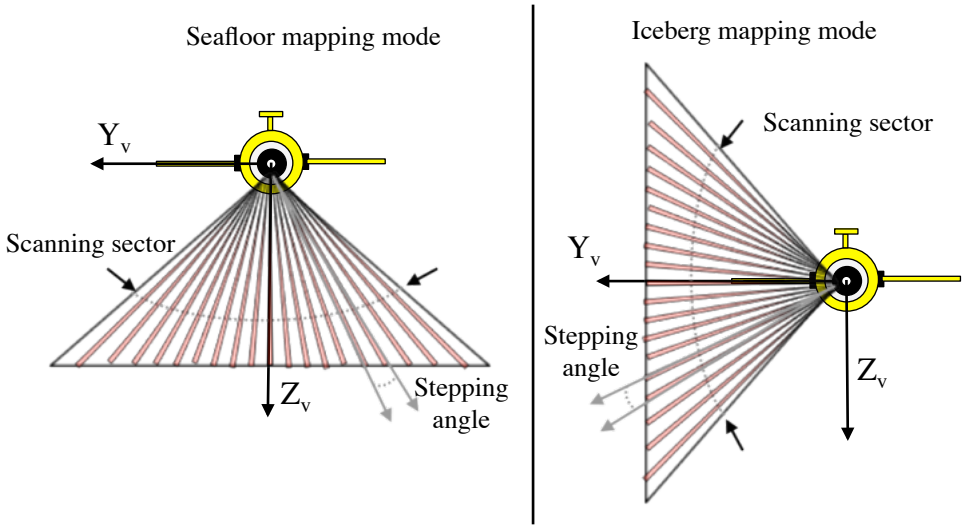


Figure 2.12: The sonar configuration in seafloor scanning and iceberg scanning modes.

Figure 2.12 shows the configurations of the sonar in seafloor mapping mode and iceberg profiling mode. The Tritech Micron mechanical scanning sonar can be configured to scan a sector from 0 to 360 degrees without mechanical modification. The left and right limit of the scanning sector is implemented that can be adjusted in

the glider's mission script. In the seafloor mapping mode, the sonar is configured with a downward-looking scanning sector, while a side-looking sector is defined in the iceberg mapping mode. In both modes, the stepping angle is defined as 1.8 degrees, the minimum stepping angle. For safety concerns in the iceberg mapping mode, the sonar can be oriented to have a forward-looking angle on the starboard side by tilting the pivot plate designed for securing the sonar (see Figure 2.1).

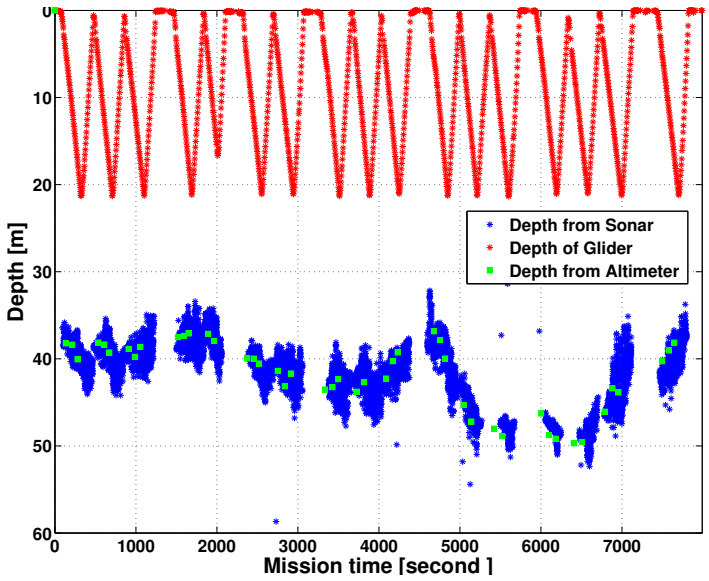


Figure 2.13: Comparison of measured seafloor depth from the altimeter and Tritech Micron mechanical scanning sonar.

The performance of the sonar is initially evaluated in the field by comparing the seafloor measurements from different sources. On July 15, 2014, a seafloor mapping mission was conducted in Conception Bay, Newfoundland, Canada. During the mission, the Slocum glider traveled through five defined waypoints in a zigzag pattern, with roughly 200 meters between two sequential waypoints. The mechanical scanning sonar is scanning downward within a sector of $\pm 60$ degrees and zero forward-looking angle. The standard-configured altimeter in the nose of the glider is looking directly downward when the vehicle is diving but disabled during climbing. When evaluating the sonar performance in a water tank, the nose cover is found to have an impact

by reducing transmitting energy from the sonar. Therefore, the receiving gain of the sonar is increased to 100% instead of 40% by default.

Figure 2.13 shows the comparison of the seafloor measurements from the altimeter on the Slocum glider and the Tritech Micron mechanical scanning sonar. The green squares are the altimeter measured seafloor depth while the blue dots are the seafloor depth measured by the Tritech Micron mechanical scanning sonar. The measurements from the two instruments show agreements in depth, except the measurements from the scanning sonar have a wider bandwidth because the sonar scanning transversely along the vehicle's track but the altimeter measures the seafloor depth directly below the vehicle when descending.

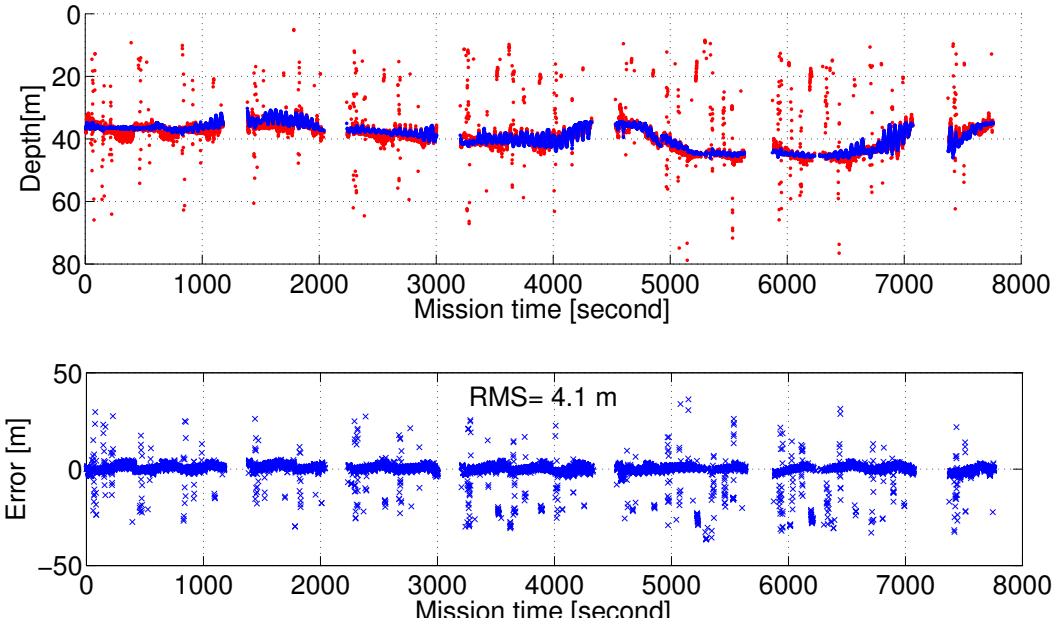


Figure 2.14: Comparing the seafloor depth measured by the mechanical scanning sonar (red) with the seafloor depth from the bathymetric map (blue).

The measurements from the mechanical scanning sonar are then compared with a digital bathymetric map provided by Marine Institute, Memorial University of Newfoundland. For each sample, the range measured by the sonar is first corrected for the average sound speed (1465 m/s) estimated from the conductivity-temperature-depth

sensor. Then the ranges are converted into points in Latitude-Longitude-Depth (see Appendix A.1 for detail). The measured depth of the seafloor is compared with the depth from the digital map at the same Latitude and Longitude. Figure 2.14 shows the seafloor depth measured from the two sources. There is good agreements between the two sources, the root-mean-square of the errors (4 meters) between them is observed that is potentially caused by the tide effects and minor errors caused by the deflection of the sound in the water layers due to the sound speed variation at depth. The sonar measured depth is then overlain on the bathymetric map in Figure 2.15. This seafloor mapping deployment approves the capability of the sonar in obtaining the topography of the target within the scanning sector. The method of extracting the range mentioned is validated by comparing the sonar measured depth with two independent sources, altimeter on the glider and a bathymetric map.

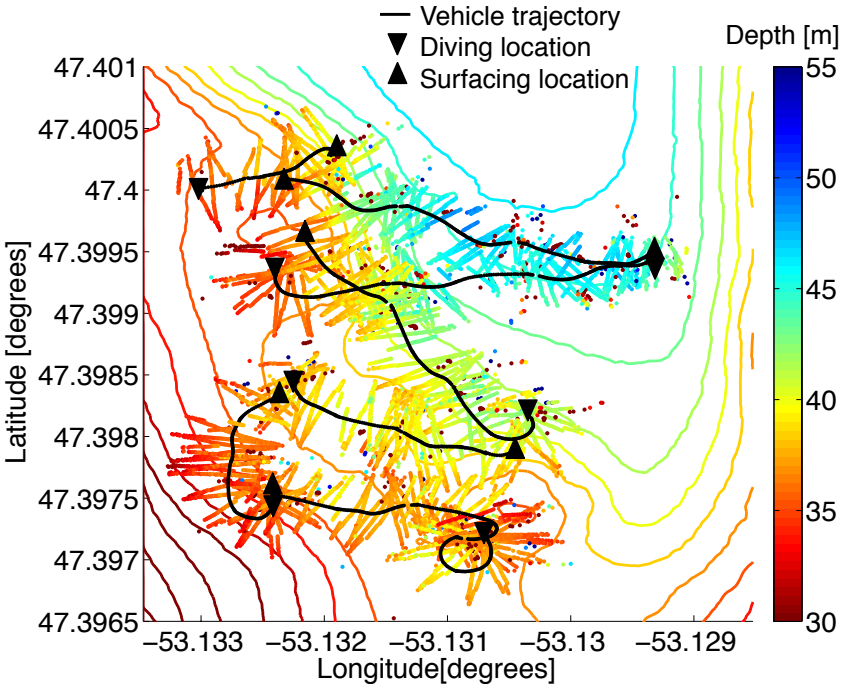


Figure 2.15: Comparing the water depth measurements from the Tritech mechanical scanning sonar with the bathymetry data provided by Marine Institute, Memorial University of Newfoundland.

## 2.4 Multi-beam Sonar

The Teledyne Blueview M450-130 multi-beam sonar (450 kHz) is also used in a ship-based iceberg profiling mission. It provides more measurements than the mechanical scanning sonar and allows the online processing with its software development kit (SDK). Figure 2.16 shows the model of the multi-beam sonar. The transducer array (768 beams) forms a field of view of 130 degrees in the horizontal direction, and 10 degrees vertically. Using the software supplied by the manufacturer, we can detect objects for range and the bearing as shown in the Figure 2.16.

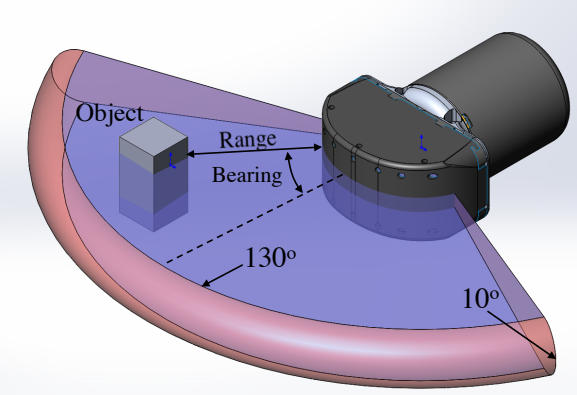


Figure 2.16: Blueview M450-130 Multi-beam sonar. The range and bearing from the sonar to a object is measured within a field of view of 130 degrees by 10 degrees.

Although it is beyond the power budget on the Slocum underwater glider, it is applicable for the small AUVs if an independent battery is used solely for the sonar. In our research, the Blueview sonar is evaluated on a support vessel in a side-looking configuration for profiling the underside of a floating iceberg (see Figure 2.17). During the ship-based iceberg mapping mission, the sonar is oriented to align the wider field of view vertically for obtaining the vertical swath on the iceberg. The sonar is further rotated downward such that the top beam is directed horizontally. The collected data is used to validate the algorithm for estimating the iceberg motion in Chapter 5. Figure 2.18 shows the procedures for extracting the ranges and bearings of the ob-

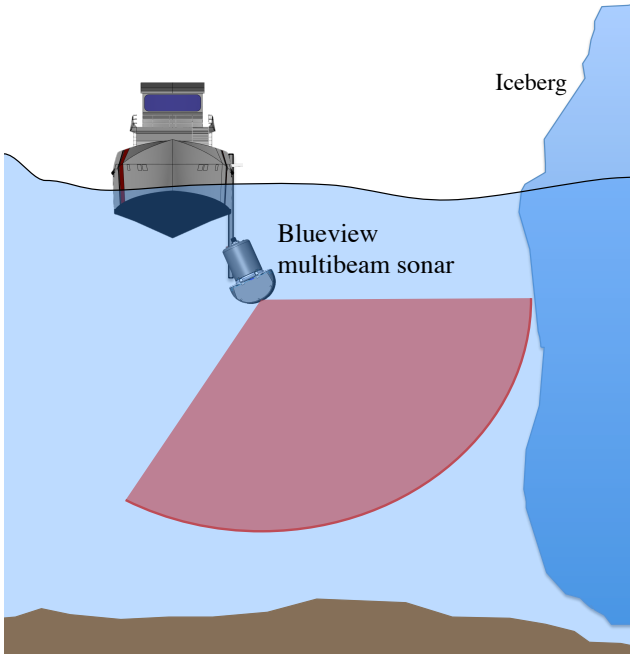


Figure 2.17: Blueview P450-130 Multibeam sonar.

stacles from the proprietary sonar file, *.son, the default logging file of the Blueview sonar. Initially, *.son file is processed into a series of images using the SDK. The image Ⓐ in Figure 2.18 presents the echo intensity in the field of view where the sonar is located at the top center of the image. Image Ⓐ is first subtracted by a template image Ⓑ where no object inside the field-of-view. As a result, the uneven fan-shape noise in image Ⓐ is minimized. The resulting image Ⓒ is then sharpened using a 2-dimensional median filter and a high-pass filter. The objects detected by the sonar are then highlighted in the image Ⓓ and Ⓔ in Figure 2.18. According to the SDK, each pixel in the image has its associated distance and bearing to the sonar. At each bearing in the field of view, its associated range measurement is found to be the distance from the sonar to the nearest highlighted point in image Ⓕ. The detected ranges are then converted into a point cloud in the inertial frame, i.e. earth frame or North-East-Down, using the orientation of the sonar and the location of the support vessel. The transformation matrix used in such a converting process is introduced in

Appendix A.1.

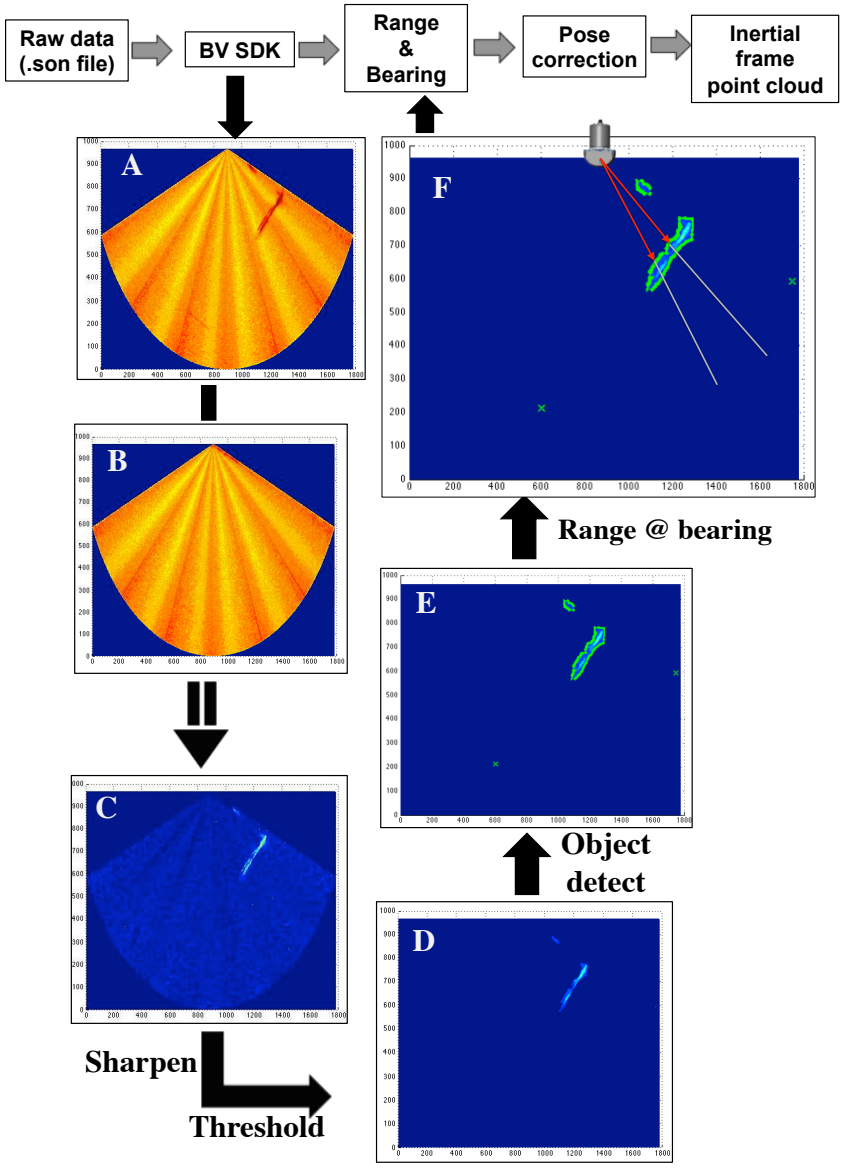


Figure 2.18: Flow chart for processing the samples from Blueview sonar

# Chapter 3

# Underwater iceberg profiling simulator

As was mentioned in the literature review, most underwater iceberg-mapping operations are conducted by lowering sonar probes from various locations around icebergs [4]. To compare various AUV-based underwater iceberg-profiling methods with this conventional method, an iceberg profiling simulator is constructed and will be presented in this chapter.

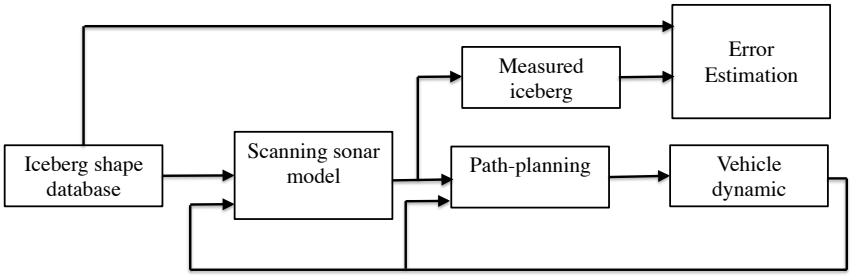


Figure 3.1: Block diagram of iceberg profiling simulator

Figure 3.1 depicts the block diagram of the simulator. In the simulated environment, iceberg shapes were obtained from an iceberg shape database presented in [91] from the National Research Council of Canada (NRCC). The three-dimensional iceberg

data from the NRCC is used to construct our numerical iceberg. A mechanical scanning sonar model is included to simulate the performance of the Tritech Micron mechanical scanning sonar which is integrated with the iceberg-profiling Slocum glider. To simulate the platforms accommodating the sonar, the path-planning block generates desired path from planned waypoints for the vehicle using the known iceberg shape and the measurements from the simulated sonar.

Both the sonar probe approach and the AUV-based method for iceberg profiling are simulated with the same sonar to map the icebergs at the same desired standoff distance. The estimated cross-sectional area and overall volume are then compared. Furthermore, the influence of factors, such as iceberg shapes and sonar pinging rates, to the mapping performance are evaluated.

Since both the profiling probe and the AUV require underwater navigation methods to resolve their location underwater, the navigation errors are not included in the performance analysis. Reviewed in Chapter 1, [25] shows some promising results of reducing the navigational error to 10 meters over a traveling distance of several kilometers with an USBL. For the purpose of this simulation, the navigation (underwater location) of the platforms are assumed known without error. The accuracy analysis is aimed to evaluate the influence from the sensors and the movement patterns of the platforms. But further analysis could be done to considered the influence of platform position error in the measurements.

## 3.1 Iceberg models

In the early 1970s to 1980s, scientists started to model icebergs from simple characteristics such as the draft, sail height, and waterline dimensions. The two-dimensional iceberg shape is modeled from the stability perspective in [92] where the iceberg

shapes are simplified into common shapes such as rectangles and triangles. The ratio of draft to height was calculated, and the minimum width to height ratio to determine iceberg stability was presented. In [43], three theoretical shape models of icebergs are proposed based on the parameters such as waterline length, width, sail height, and the draft. The iceberg models allow an immediate check on iceberg stability during field surveys. Two hundred measured icebergs were investigated and presented in [47]. The draft to sail height ratio is found to follow a power curve (see Equation 3.1. In 2004, a model of keel geometry was proposed [48]. It was found the draft has a linear relationship wtih the length of the iceberg. The cross-sections of an iceberg are modeled in stacked layers.

$$\text{Draft} = \text{Height} \cdot 49.4 \cdot (\text{Height})^{-0.8} \tag{3.1}$$

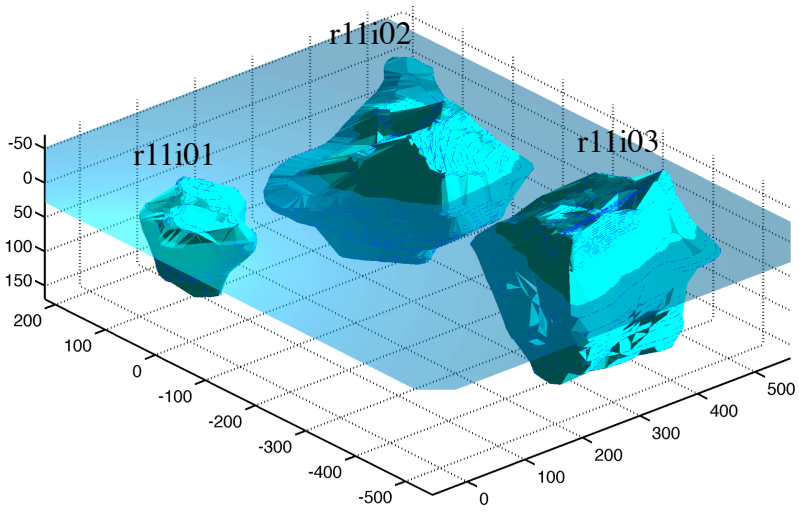


Figure 3.2: Three icebergs from the iceberg database provided by National Research Council Canada [91].

Instead of modeling icebergs, an iceberg shape database created by the National Research Council Canada (NRC) was introduced in [90] and [91]. These available iceberg shapes are currently used to construct target icebergs in the simulator. This

database contains the measured dimensions from 872 icebergs. Among those icebergs, 28 iceberg keels are available in a digital format, while others are available only in a chart format. The digitized iceberg shapes are represented as cross-sectional profiles at different depths, similar to iso-bathymetric or depth contours on nautical charts.

Table 3.1: Summary of the characteristics of the three icebergs

| Features | r11i01 | r11i02 | r11i03 |
|---|---|---|---|
| Width [m] | 148 | 221 | 235 |
| Length [m] | 161 | 257 | 259 |
| Height [m] | 31 | 50 | 68 |
| Below water shape | dome | dome | blocky |
| Draft [m] | 110 | 140 | 170 |
| Weight [million kg] | 1091 | 5265 | 6908 |

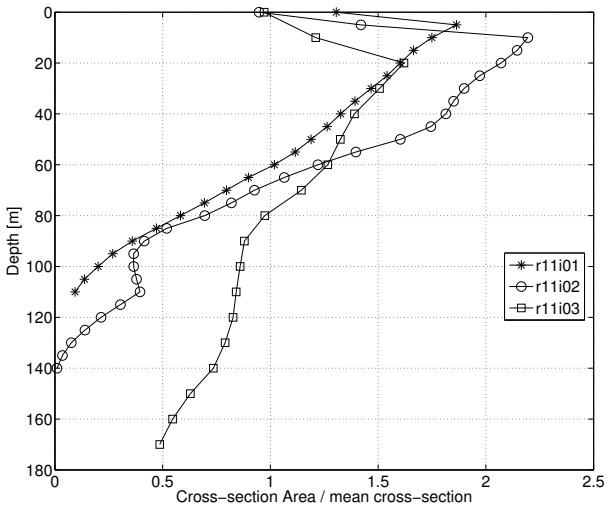


Figure 3.3: Areas of the cross-sectional profile normalized with its averaged cross-sectional area.

Figure 3.2 shows the three icebergs selected for our simulation. The iceberg surface is constructed by applying the Alpha Shape [93] on the three-dimensional data points. In 1988, the three icebergs were profiled with the technique introduced in [4] where the underwater portions were obtained by mosaicing the sidescan sonar measurements at four locations around the icebergs. The characteristics of the icebergs are summa-

rized in Table 3.1 where the weights are calculated based on a density of 910 $kg/m^3$ estimated in [48].

Figure 3.3 shows the variation of the cross-sectional area of the selected icebergs. At an incremental depth, the cross-sectional area is normalized with the averaged cross-sectional area of the entire iceberg below water. It is observed that r11i03 has the least variability in its vertical profile, while r11i02 has the steepest vertical profile variation. These particular characteristics of the icebergs described in Table 3.1 and shown in Figure 3.3 have potential effects on the overall mapping accuracy and survey time.

## 3.2 Model of the Tritech Micron Mechanical scanning sonar

The sonar equation (Equation 3.2) is widely used in sonar design and modeling. It represents the sound propagation from the perspective of conservation of energy that the echo intensity ($EI$) received by the sonar is equal to the transmitted power ($SL$ and $DI$) minus the energy loss ($TL$, $AL$, and $TS$) in the environment.

$$EI = SL + DI + 2TL + 2AL + TS \tag{3.2}$$

$$SL = 170.8 + 10\log_{10} P_e + 10\log_{10} E \tag{3.3}$$

As discussed in [94], the source level ($SL$) is the energy emitted by a sound source, i.e. the acoustic transducer. The emitted energy can be calculated using Equation 3.3 in the water, where $P_e$ is the electric power, $E$ is the percentage of the energy used in transmitting sound out of the overall applied power. $SL$ is in decibels reference to

the pressure of 1 MPa, at 1 meter.

The directivity index ($DI$) illustrates the differential power around the sonar at different transmitting angles. For a uniform sound source in two-dimensional space, the directivity is calculated using Equation 3.4 where $W$ is the width of the source, $\delta$ is the transmitting angle, and $k$ is the wave number. Computation of the DI for other types of sound source can be found in [95].

$$DI = 10\log_{10}\frac{\sin(\frac{kW}{2}\sin(\delta))}{\frac{kW}{2}\sin(\delta)} \tag{3.4}$$

Assuming the sound is spreading spherically in a homogeneous and isotropic medium, the energy is then distributed evenly over the spherical area which increases with the range to the source. Therefore, the energy at each point on the sphere decreases over the range ($R$) of sound propagated. The decreased energy is presented in Equation 3.5 in the unit of dB.

$$TL = -10\log_{10}(R^2) \tag{3.5}$$

Nevertheless, part of the acoustical energy is converted into heat dissipated in the medium. Such energy loss is defined as the attenuation loss ($AL$). The attenuation coefficient ($\alpha$) describes the reduction of sound intensity relative to the distance that the sound has propagated. One cause of energy dissipation is due to the viscosity of the medium. Equation 3.6 proposed in [98] shows the relation between the viscosity and the absorption, where $\mu_v$ and $\mu_s$ are the viscosity coefficient, $\rho$ is the density of the medium, $c$ and $f$ are the speed and the frequency of the sound. Proven in [99], the ionic relaxation of magnesium sulfate ($MgSO_4$) is the dominant cause of absorption in seawater below 100 kHz. But the $MgSO_4$ will have minor impact on the modeled mechanical scanning sonar which has a nominal frequency of 700 kHz. The results

from different researchers are summarized in [100] with a derived equation shown in Equation 3.7. The three individual parts in Equation 3.7 represent the attenuation coefficients due to the Boric Acid, $MgSO_4$, and pure water. Meanwhile, a chart showing the relation between frequency and attenuation rate is shown in Figure 3.4. It allows us to obtain the overall attenuation coefficient for Equation 3.8 at various sound frequencies.

$$\alpha = \frac{16\pi^2}{3\rho c^3}(\mu_s + \frac{3}{4}\mu_v)f^2 \tag{3.6}$$

$$\alpha = \frac{A_1 P_1 f_1 f^2}{f^2 + f_1^2} + \frac{A_2 P_2 f_2 f^2}{f^2 + f_2^2} + A_3 P_3 f^2 \quad [dB/km] \tag{3.7}$$

$$AL = -\alpha \cdot R \tag{3.8}$$

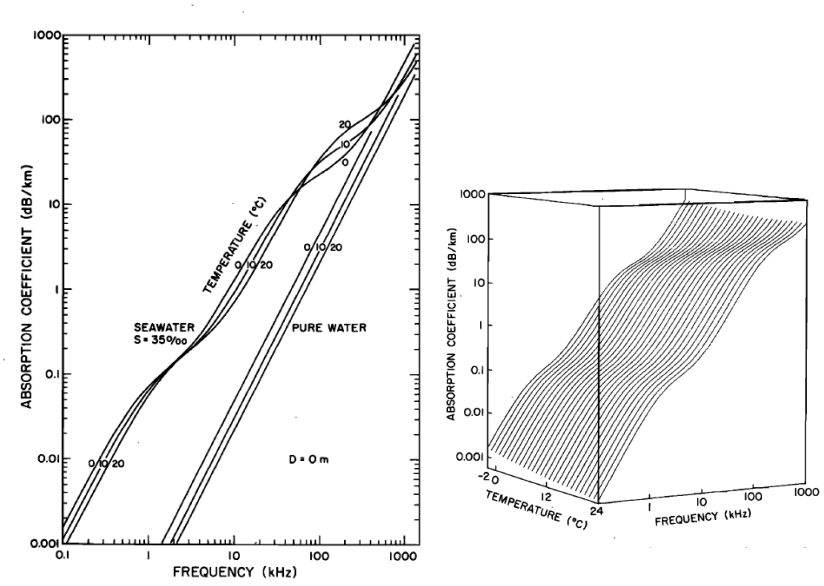


Figure 3.4: Attenuation rate at various sound frequency and temperature in the fresh water and salt water [100]

As sound propagates further, it collides with objects in the medium or reaches the

boundary of the medium, e.g. the seafloor or water surface. As shown in Figure 3.5, a part of the energy ($I_D$) is deflected away from the sound source, and part of the energy ($SL'$) is reflected backward sharing the propagating path. The loss of energy, $SL' - SL$, is defined as the target strength ($TS$) that depends on the physical parameters, such as radius, the surface roughness of the target, and the incident angle of the sound. In [95] and [94], the target strength of small targets are discussed in Chapter 7 and Chapter 9 respectively. For boundaries, the target strength is renamed as backscatter strength ($BS$) and discussed in [96] in Chapter 8. The BS from the boundaries is formulated in Equation 3.9 where $\mu$ is a scattering constant that can be measured empirically, and $\theta_i$ is the incident angle shown in Figure 3.5. As shown in Figure 3.6, the point cloud of the iceberg is rendered as a fractal terrain [97]. The incident angle is determined by the angle between the ray vector of the sonar and the normal vector of the surface.

$$BS = 10 \log_{10} \mu + 10 \log_{10} \sin^2 \theta_i \tag{3.9}$$

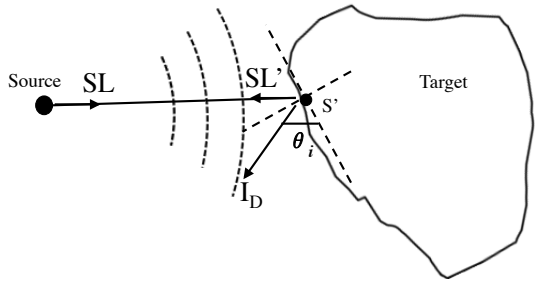


Figure 3.5: At the incident area, only a portion of the energy is reflected while the remaining energy are deflected.

The Tritech Micron mechanical scanning sonar is modeled using the sonar equation introduced above. As shown in Figure 3.7, the sonar has a wide beamwidth of $35^o$ in the longitudinal direction and a narrow beamwidth of $3^o$ in the scanning direction. At a maximum range of 75 meters, the major and minor radius of the elliptical foot-print

are 22.5 meters and 2 meters. To simplify the simulation, the sound propagation is modeled only for the wide beamwidth with 35 straight extending rays. The $DI$ at different rays are calculated using Equation 3.4 and are shown in Figure 3.7. The -3dB line intercepts the beam pattern at $\pm 17.5^o$ which is consistent with the specification of the sonar. The sonar equation is used to calculate the energy on each ray at incremental range equals to the range resolution of the sonar that is 1/400 of the configured maximum range. At each incremental range, the $AL$ and $TL$ are calculated for the rays. If any ray intersects the iceberg, the $BS$, $AL$ and $TL$ in the back-propagation are calculated. As a result of the iteration at the end, a curve of intensity-at-range that is the same format as the actual sonar output is obtained.

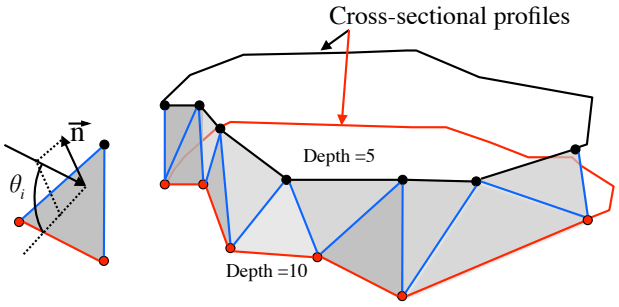


Figure 3.6: Deriving the incident angle from the fractal iceberg surface.

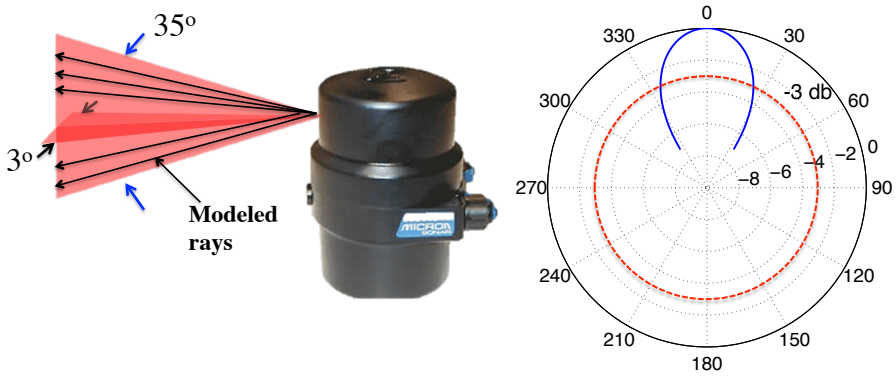


Figure 3.7: Tritech Micron mechanical scanning sonar and modelled beam pattern of the main lobe

Figure 3.8 shows the output from the modeled sonar. The sonar is placed at the origin

of the plot and it is 40 meters away from a flat wall. The sonar scans 180 degrees at a stepping angle of 1.8 degrees with the profiling range of 70 meters. The sonar outputs are presented in a Cartesian coordinate system with the received sound intensity displayed follow the color scheme. The detected ranges can be further extracted using the method mentioned in Section 2.3 in Chapter 2. In order to constrain the complexity of the simulation and minimize the execution time, advanced sonar models such as those that maintain consistent ray separation at the ensonified surface [101] are not used.

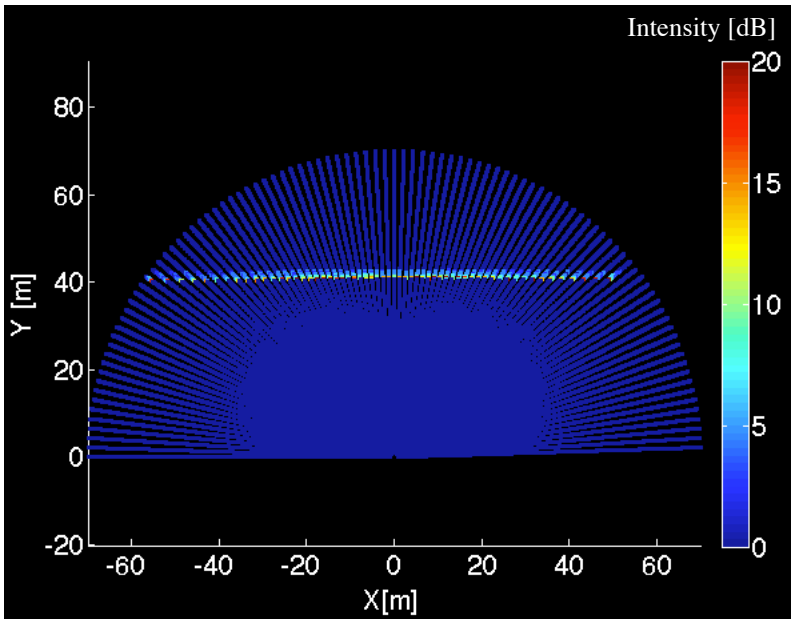


Figure 3.8: Modeled the sonar output when the sonar is scanning at sector of $180^o$ on a flat wall 40 meters away from it.

## 3.3 Path planning and vehicle dynamics

A vertical sonar probe and an AUV are modeled in the iceberg profiling simulator. The platforms are assumed to have a constant moving velocity of 0.5 m/s with constrained roll motion.

The vertical profiling mode is designed to model a tethered sonar probe used in conventional ship-based profiling method. For each iceberg, eight vertical sampling patterns are conducted from different locations around the iceberg.

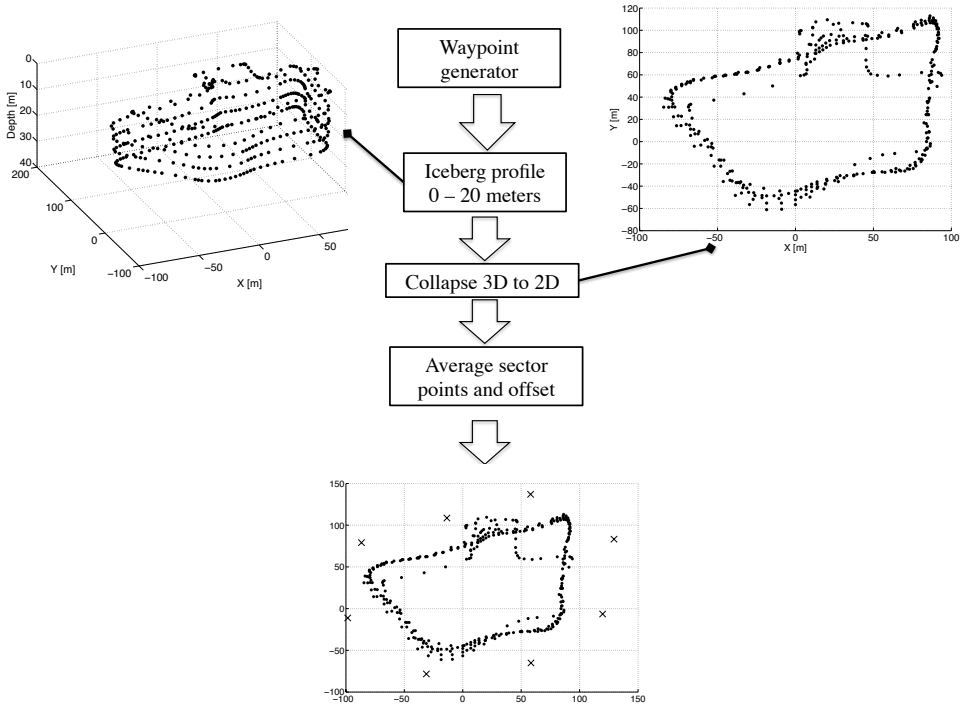


Figure 3.9: Diagram of obatining waypoints in the vertical mode. The crosses are the proposed locations of deployment while the dots are the sonar measured iceberg surface points

Figure 3.9 shows the locations of deployment for the vertical sonar probe determined from the assumed known iceberg profile from 0 to 20 meters. Such information can be measured by a sonar attached to a surface vessel. The profiles are collapsed from 3 dimensions onto the horizontal plane. The two-dimensional profile is then separated into eight sectors with a sector angle of $45^o$. In each sector, a deployment location is determined by averaging the coordinates of the detected iceberg points and then expanded outward a safe distance. After the deployment locations have been determined, the probe descends to a target depth at a constant speed of 0.5 m/s, while the simulated mechanical scanning sonar scans a horizontal sector of $\pm 45$ along the

trajectory.

In contrast, a simplified AUV is modeled to travel around the iceberg in a spiral pattern. The vehicle motion is simulated in a steady state without any hydrodynamic influence. The vehicle is assumed to move at a constant surge speed ($V$) of 0.5 m/s, and following a list of waypoints by adjusting its pitch angle and heading. The mechanical scanning sonar scans the starboard side of the vehicle up and down within the $\pm 45$ degrees off the horizontal plane of the vehicle.

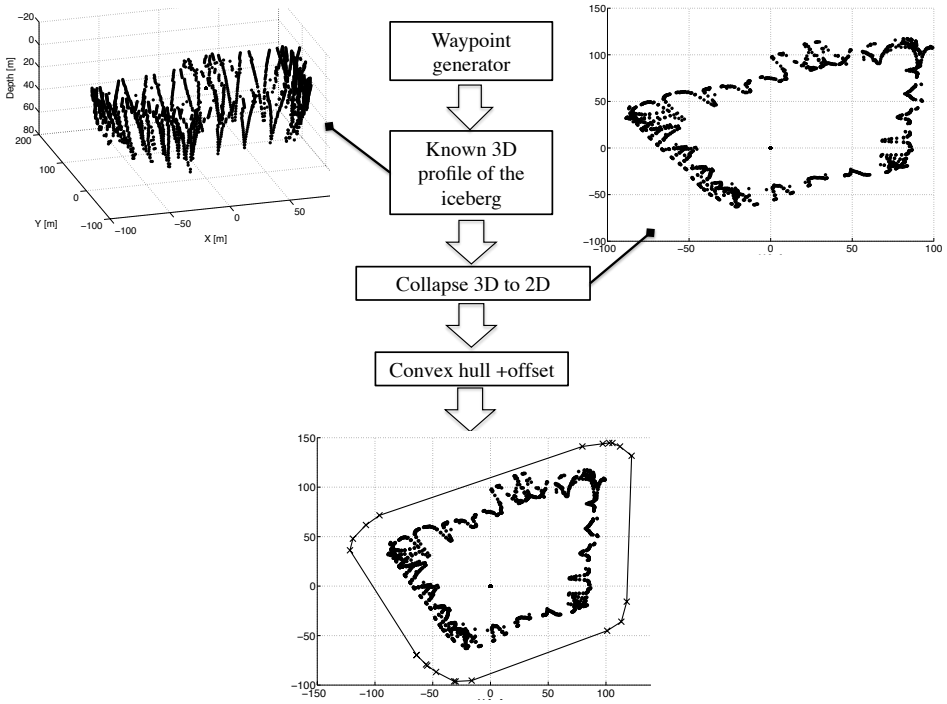


Figure 3.10: Diagram of obtaining waypoints in the AUV mode. The planned path enclose the sonar measured iceberg surface points

The steady-states of the vehicle in transition between waypoints $\mathbf{W}_i = [W_x(i), W_y(i), W_z(i)]^T$ are shown in Equation 3.10. The waypoints are determined from the known iceberg profiles with a flow chart shown in Figure 3.10. In determining the desired vehicle path in the horizontal plane, the known iceberg profile is collapsed into two-dimensional points and expanded outward with a standoff distance. Then convex hull ([102] and [103]), that filters a group of points by finding the outmost points to enclose all the

points, is applied such that the desired path is simplified to a reduced number of data points assigned as the waypoints. By now, the location of the waypoints in the horizontal plane is resolved. Since, the vehicle is operated in steady-state, the depth rate of the vehicle is proportional to the horizontal speed. Therefore, the depths of the determined waypoints are calculated using Equation 3.11 with a known depth range of waypoints $\sum_{i=1}^{n} \Delta W_z(i)$. It is determined from the current vehicle depth to the maximum detected iceberg depth (initially 20 meters). The list of waypoints will be updated once the vehicle reaches the last waypoint on the current list. The operation finishes once the vehicle detects no valid iceberg measurements from the depth below the vehicle when traveling through the latest list of waypoints.

$$\begin{bmatrix} V_x(i) \\ V_y(i) \\ V_z(i) \\ \theta(i) \\ \psi(i) \end{bmatrix} = \begin{bmatrix} V \cdot \cos\theta(i) \cdot \cos\psi(i) \\ V \cdot \cos\theta(i) \cdot \sin\psi(i) \\ V \cdot \sin\theta(i) \\ \arccos \frac{W_z(i) - W_z(i-1)}{|\mathbf{W}(i) - \mathbf{W}(i-1)|} \\ \arctan \frac{W_y(i) - W_y(i-1)}{W_x(i) - W_x(i-1)} \end{bmatrix} \tag{3.10}$$

$$\frac{\Delta W_z(i)}{\sqrt{\Delta W_y(i)^2 + \Delta W_x(i)^2}} = \frac{\sum_{i=1}^{n} \Delta W_z(i)}{\sum_{i=1}^{n} \sqrt{\Delta W_y(i)^2 + \Delta W_x(i)^2}} \tag{3.11}$$

## 3.4 Verification of AUV-based underwater iceberg profiling

Simulations are conducted on the three selected icebergs using the two modeled platforms equipped with the mechanical scanning sonar. The parameters for the iceberg profiling simulations are listed in Table 3.2. The sonar has a profiling range of 70 meters with a range resolution of 17.5 cm. The scanning sector of the sonar is $\pm 45^o$

transverse to the vehicle's track with a stepping angle of $1.8^o$. Three levels of sampling frequency are simulated on the sonar to evaluate the influence of the density of the measurements to the overall accuracy in estimating the iceberg shape. The platforms are assumed moving at a constant speed of 0.5 m/s with the trajectories generated using the method introduced in the previous section. The stand-off distance for the desired path is 35 meters.

Table 3.2: Sonar configuration for iceberg profiling simulations

| Parameter | Setting | Parameter | Setting |
|---|---|---|---|
| Sonar range | 70 meters | Range resolution | 17.5 cm |
| Sonar scanning sector | $\pm 45^o$ | Vehicle speed | 0.5m/s |
| Sonar step angle | $1.8^o$ | Safety distance | 35 meters |
| Sonar sampling frequency | 1 Hz,2 Hz,5 Hz | | |

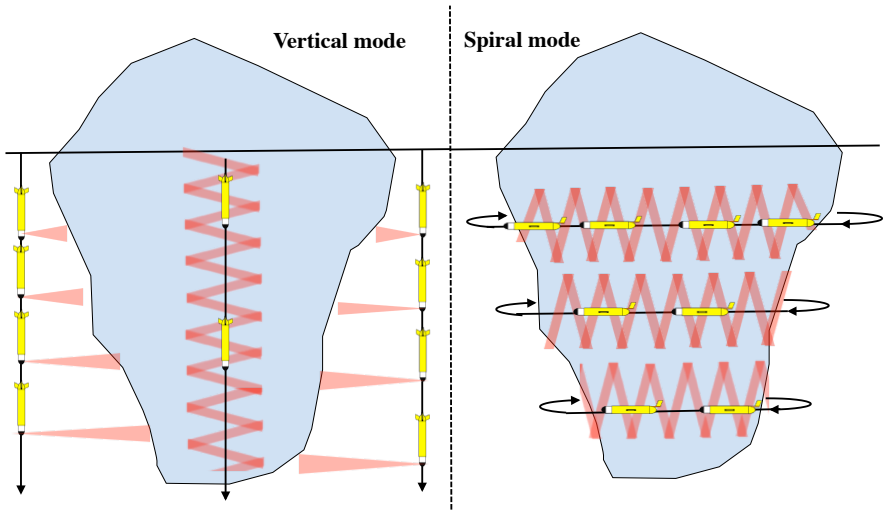


Figure 3.11: Sonar footprints on the iceberg with scanning sector of $\pm 45^o$ transverse to the trajectory for the two modeled platform motion profiles

Figure 3.11 shows the footprints of the mechanical scanning sonar applied to an iceberg based on different modeled motion profiles. In the simulation, the iceberg is assumed stationary, and the sonar measured ranges are converted into an inertial coordinate system displaying the measured iceberg surface in the form of a point cloud. The

point cloud is further processed by separating the points into cross-sectional profiles at incremental depth that is similar to the original iceberg profiles available in the database. Appendix A.3 summarizes resulting point clouds from the simulations, and the reference point cloud is from the iceberg shape database provided by the NRCC. Several metrics are introduced to evaluate and compare the performance from different simulations. $\mathbf{A}'_d$, the measured area of the cross-sections at depth $d$ are compared with the cross-section of the target icebergs $\mathbf{A}_d$. At each depth, the percentage error of each cross-sectional profile, $\boldsymbol{\epsilon}_d$, is calculated in Equation 3.12. Then the average ($\boldsymbol{\mu}$), standard deviation ($\boldsymbol{\sigma}$), and root-mean-square (RMS) of $\boldsymbol{\epsilon}_d$ are computed. The percentage error for the overall volume, $\boldsymbol{\epsilon}_V$, is computed by integrating the cross-sectional profiles with its depth span $\Delta d$ in Equation 3.13. These metrics from different simulations are compared in Table 3.3. The numbers of iceberg samples and operational time of the platforms are also included.

$$\boldsymbol{\epsilon}_d = |\frac{\mathbf{A}'_d - \mathbf{A}_d}{\mathbf{A}_d}| \cdot 100\% \tag{3.12}$$

$$\boldsymbol{\epsilon}_V = |\frac{\sum_0^{\max(d)}(\mathbf{A}'_d \Delta d) - \sum_0^{\max(d)}(\mathbf{A}_d \Delta d)}{\sum_0^{\max(d)}(\mathbf{A}_d \Delta d)}| \cdot 100\% \tag{3.13}$$

We obtain the percentage error for the cross-sectional profiles ($\boldsymbol{\epsilon}_d$), the $\boldsymbol{\mu}$ are smaller for the AUV than on the sonar probe. The $\boldsymbol{\mu}$ is about 15% on the AUV-based sonar survey compared with such result from the vertical sonar probe that is up to 40% on the iceberg r11i02. The $\boldsymbol{\sigma}$ and RMS of the percentage error are also smaller in the AUV-based operation, meaning the error is more consistent and stable comparing a large fluctuation on the vertical sonar probe. Figure 3.12 shows the comparison of $\boldsymbol{\epsilon}_d$ at incremental depth indicating a more consistent result from spiral AUV (blue) than from the vertical probe (red).

Table 3.3: Summary of the performance in the vertical mode and the AUV mode

| | | $\boldsymbol{\epsilon}_d$ [%] | | | $\boldsymbol{\epsilon}_V$ [%] | Samples size | Time [min] |
|---|---|---|---|---|---|---|---|
| Iceberg | $f$[Hz] | $\boldsymbol{\mu}$ | $\boldsymbol{\sigma}$ | RMS | | | |
| | | Vertical sonar probe | | | | | |
| r11i01 | 1 | 27.97 | 25.43 | 37.43 | 10.73 | 1236 | 39 |
| | 2 | 22.26 | 25.13 | 33.16 | 0.33 | 2453 | 39 |
| | 5 | 36.13 | 53.88 | 63.9 | 12.23 | 6121 | 39 |
| r11i02 | 1 | 44.89 | 40.52 | 60.00 | 23.10 | 1066 | 47 |
| | 2 | 49.58 | 39.13 | 62.74 | 20.04 | 1992 | 47 |
| | 5 | 45.57 | 39.27 | 59.72 | 0.55 | 5518 | 47 |
| r11i03 | 1 | 22.89 | 25.00 | 33.38 | 15.48 | 1854 | 55 |
| | 2 | 14.40 | 11.37 | 18.15 | 5.57 | 3649 | 55 |
| | 5 | 9.92 | 8.33 | 12.8 | 0.01 | 9131 | 55 |
| | | Spiral AUV | | | | | |
| r11i01 | 1 | 15.70 | 14.02 | 20.84 | 10.31 | 4128 | 134 |
| | 2 | 13.96 | 12.15 | 18.33 | 10.20 | 8658 | 143 |
| | 5 | 13.31 | 11.69 | 17.50 | 9.82 | 21819 | 147 |
| r11i02 | 1 | 13.41 | 26.26 | 29.08 | 8.02 | 8969 | 301 |
| | 2 | 17.78 | 38.48 | 41.78 | 8.45 | 17122 | 276 |
| | 5 | 18.00 | 27.55 | 32.51 | 5.82 | 41373 | 272 |
| r11i03 | 1 | 8.58 | 11.70 | 14.25 | 7.32 | 10693 | 305 |
| | 2 | 8.19 | 11.59 | 13.93 | 7.91 | 20918 | 308 |
| | 5 | 7.69 | 11.85 | 13.85 | 7.69 | 51176 | 309 |

Furthermore, the volume estimated from the AUV are more consistent, less variation, than the vertical probe. As seen from the Table 3.3, the $\boldsymbol{\epsilon}_V$ in the vertical mode is lower than 1% but has a high average and standard deviation in $\boldsymbol{\epsilon}_d$. This is inconsistency is induced by Equation 3.13 in computing the volume. The volume error caused by the $\mathbf{A}'_d$ is larger than $\mathbf{A}_d$ and the $\mathbf{A}'_d$ is smaller than $\mathbf{A}_d$. It appears that the errors canceled each other in the summation. Therefore, low values in $\boldsymbol{\mu}$ and $\boldsymbol{\sigma}$ will lead to a low error in the overall volume ($\boldsymbol{\epsilon}_V$), but not vice versa. No major improvements are founded in the $\boldsymbol{\mu}$, $\boldsymbol{\sigma}$ and RMS, when comparing the results from different sampling levels. The estimated cross-sectional profiles are slightly more accurate when the sonar is operating at 5 Hz than at 1 Hz.

Key features of icebergs, variation in cross-sectional area over the depth, are founded

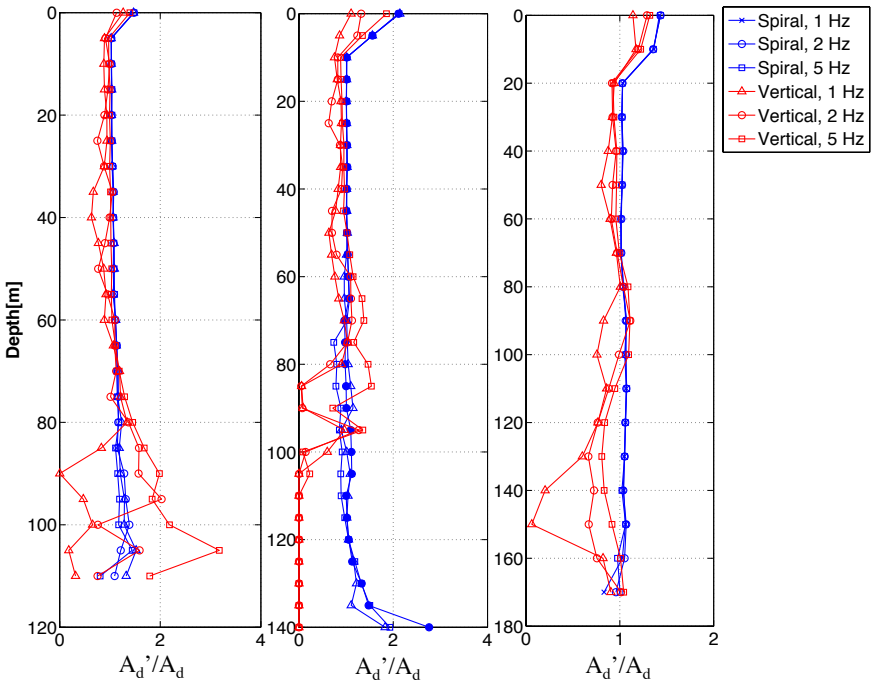


Figure 3.12: Comparison of the measured and the actual area of the cross-sections in different modes.

to have an impact on the performance. Previously, Figure 3.3 from Section 3.1 shows the variation of the cross-sectional profile. Iceberg r11i02 has the highest variability while r11i03 has a relatively uniform blocky shape. After comparing the $\boldsymbol{\epsilon}_d$ for different icebergs, the cross-sectional errors have the largest standard deviation and average values on the iceberg r11i02 and the least values on the iceberg r11i03. Large errors in cross-sectional profile at greater depth are found on r11i02. Therefore, the distance from the vehicle to the iceberg profile at reduced size may exceed the maximum profile range of the sonar that producing a gap. The reduction in the cross-sectional profile is a critical problem for the vertical sonar probe whose deployment locations are determined from the surface where icebergs usually have a larger cross-sectional profile. To insure the iceberg detection at greater depth, the sonars integrated in vertical sonar probes usually have a larger profiling range, over 150 meters. Noticeable, the vertical probe still yields larger errors in estimating the cross-section area at

shallower depths where the assumed sonar range is sufficient in detecting iceberg surface. As shown in Figure 3.12, the blue points are closer to one than the red points. Such difference is caused by the limited horizontal field-of-view of the sonar. Although the scanning sector can be increased to ±90 degrees, the sensor dropouts may happen at large angles off the central plane where the sound is deflected away from the sonar at the ensonified area due to the small incident angle. The dropouts limit the valid field-of-view on the icebergs. The number of deployments of the vertical probe can be doubled to increase the coverage and lower the error, but then the overall mission time will increase.

As shown in Table 3.3, the survey time is about six times greater for the AUV mode than in the vertical mode. Among the simulations with the AUV, the longest operation is about 5 hours on the r11i03 iceberg. It is possible to reduce the operation time by increasing vehicle speed. The velocity assumed in the simulation, 0.5 m/s, is near the minimum speed of survey-class AUVs. The left plot in Figure 3.13 shows the resulting point cloud from the AUV mode for the r11i03 iceberg when the sonar is scanning at 2 Hz. The AUV circumnavigated around the iceberg seven times during the mission, a high ratio of vertical overlap between consequential revolutions is detected. The right plot in Figure 3.13 shows the sonar measurements from the four continuous circumnavigations where significant overlaps are found between the sonar measurements from two continuous layers. The number of revolutions can be decreased to have a lower overlap ratio that decreases the survey time of the mission dramatically. Now only a subset of the sonar measurements are selected for computing the error percentage. For example, the point clouds in blue, green, yellow, and magenta in Figure 3.13 are included while the points in other colors are excluded. Table 3.4 summarized the error percentage from the reduced revolutions. The result shown in Table 3.4 illustrates that there is no significant increase in error with reduced

revolutions. Such a result implies the potential to reduce the survey time by reducing the iceberg circumnavigations without significantly increase the error.

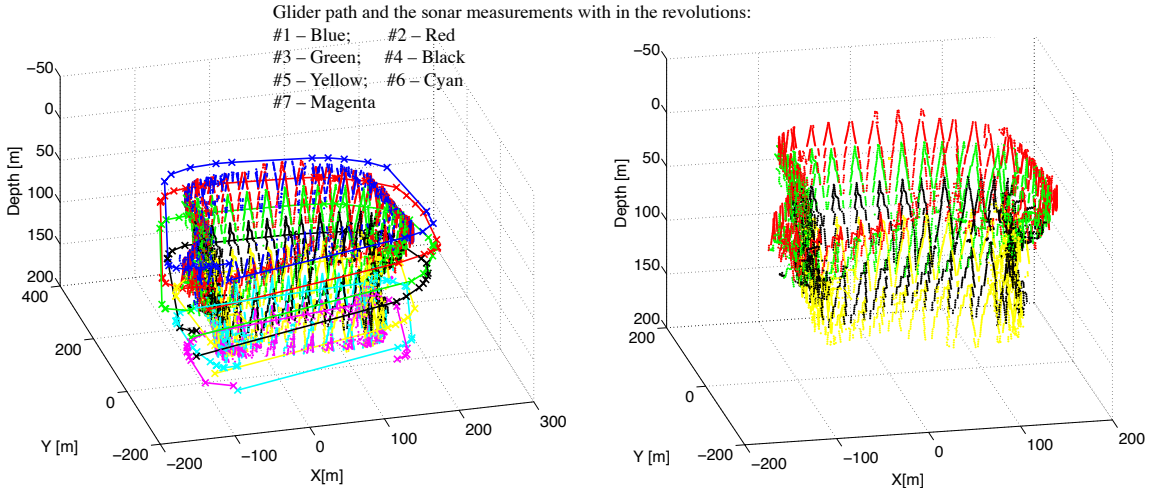


Figure 3.13: Left: The sonar measurements and vehicle trajectories in multiple revolutions around the iceberg. Right: The sonar measurements from four sequential revolutions.

Table 3.4: Comparison the percentage errors of the reduced revolutions to the original revolutions

| | | Reduced revolutions | | | | Original | | | |
|---|---|---|---|---|---|---|---|---|---|
| | | $\epsilon_d$ [%] | | | time | $\epsilon_d$ [%] | | | time |
| Iceberg | $f$[Hz] | $\mu$ | $\sigma$ | RMS | [mins] | $\mu$ | $\sigma$ | RMS | [mins] |
| r11i01 | 1 | 15.36 | 15.91 | 21.87 | 66 | 15.70 | 14.02 | 20.84 | 134 |
| | 2 | 12.26 | 10.48 | 15.98 | 73 | 13.96 | 12.15 | 18.33 | 143 |
| | 5 | 13.51 | 11.69 | 17.70 | 72 | 13.31 | 11.69 | 17.50 | 147 |
| r11i02 | 1 | 16.88 | 28.36 | 32.58 | 194 | 13.41 | 26.26 | 29.08 | 301 |
| | 2 | 17.90 | 33.55 | 37.52 | 165 | 17.78 | 38.48 | 41.78 | 276 |
| | 5 | 20.51 | 30.87 | 36.62 | 160 | 18.00 | 27.55 | 32.51 | 272 |
| r11i03 | 1 | 7.54 | 11.61 | 13.57 | 180 | 8.58 | 11.70 | 14.25 | 305 |
| | 2 | 7.94 | 11.13 | 13.42 | 135 | 8.19 | 11.59 | 13.93 | 308 |
| | 5 | 7.54 | 11.25 | 13.28 | 151 | 7.69 | 11.85 | 13.85 | 309 |

When using a long endurance AUV, such as the Slocum glider, the cost of using the support vessel is minimized therefore reducing the importance of the survey duration when compared to ship-based operations. The AUVs can be deployed for a multi-day

non-stop iceberg mapping mission until it is recovered again from a support vessel. In contrast, the vertical probe will require the support of a vessel and operators during the deployments and recovery that has to be conducted multiple time on a single iceberg.

Comparing the two operations in terms of cost, a support vessel normally cost $20,000 to $40,000 per day, while the cost of operating an Slocum glider is about $2,000 per day including the battery consumption on the AUV, depreciation of the value over a period about 10 years, and a remote glider operator. Based on the results of this verification, the AUV-based iceberg-profiling mission normally took 3 hours while the ship-based method took only 1 hour. However, the ship is assumed operating 12 hours a day and the AUV can be operated 24 hours a day. Within a week, the numbers of icebergs can be profiled by the two methods are not significantly different. However, the cost of operating the ship in a week is extremely high comparing to the cost of operating an AUV for iceberg profiling.

In summary, the verification of AUV-based iceberg-profiling indicated that it is more accurate and less expensive than the ship-based approach. Beyond that, it potentially reduces the risk to human by significantly lowering the needs for the presence of humans in a harsh environment.

# Chapter 4

# Developing the Guidance, Navigation and Control on the Slocum glider for iceberg survey

In Chapter 3, the AUV-based underwater iceberg mapping is simulated and compared with the conventional sonar probe that profiles the iceberg in a vertical pattern. Since the icebergs of interests are assumed stationary, the path planning using georeferenced waypoints works well for the simulation in the AUV mode. In reality however, icebergs are usually floating. The surge, sway, and yaw of icebergs are affected by forces and moments applied by the wind, current and waves, while the roll, pitch, and heave are predominantly caused by the iceberg deterioration. Therefore, I have assumed that a floating iceberg is moving in the horizontal plane with additional rotating speed about the vertical axis through the centroid of the waterline plane. Without knowing the iceberg motion initially, the path planning introduced in the previous chapter is not suitable for the AUV control in profile-following unless the AUV navigation and waypoints are referenced to the iceberg-centered coordinate frame instead of the

inertial coordinate (NED). The Aerospace Robotics Lab (ARL) in Stanford University made considerable progress in solving the navigation of AUVs relative to the iceberg frame ([52] and [59] to[62]). The authors used a side-looking Doppler Velocity Log (DVL) to measure the linear velocity of the vehicle relative to the iceberg, while the rotation of the iceberg is estimated using a point matching technique.

In this Chapter, the development of iceberg oriented guidance, navigation and control (GNC) is introduced. I am addressing this issue in several incrementally more complex steps. Initially, the glider is deployed to travel around a grounded iceberg following predetermined GPS coordinates sampled in proximity of the iceberg. This trial confirms the sonar capability and the range extraction algorithm in detecting iceberg surface. Second, I am developing a low-level adaptive heading controller to actively control the vehicle to avoid collision with icebergs. The performance of the controller is proven in a simulated environment and tested in the field. However, some issues appeared showing that the controller is not suitable to control the vehicle at highly variable terrain as is expected in the iceberg-profiling case. An improved GNC system must then be designed. We will show that the improved GNC system performed well in both simulation and the field successfully enabling the AUV to follow and map an underside portion of an iceberg.

## 4.1 Mapping icebergs with pre-defined waypoints using the Slocum glider

The modified Slocum glider shown in Figure 4.1 was deployed near a grounded iceberg in Conception Bay, Newfoundland, Canada, in June 2015. The target iceberg is shown Figure 4.2. The above water dimension of the iceberg is approximately 150 meters by 100 meters by 30 meters in length-width-height. The sonar was config-

ured scanning within the ±45 off the horizontal plane of the vehicle at a 35 degrees forward-looking angle. The ranges reported by the sonar were recorded on-board, but not used to change the predetermined trajectory of the glider. Since the iceberg was grounded, the glider was operated in the waypoint-following mode using the GPS coordinates around the iceberg. The GPS coordinates around the iceberg were collected manually by driving a small craft around the iceberg. The desired waypoints were placed approximately 40 meters away from the iceberg. The glider was operated in gliding mode (sawtooth pattern) to travel between 10 and 25 m of depth. In order to obtain a valid GPS fix and communication with control center for potential operator intervention, the surfacing interval for the glider was set to be every 12 minutes.

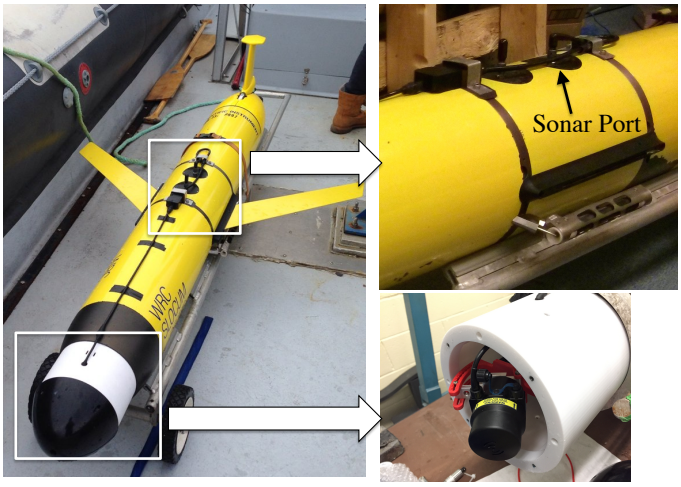


Figure 4.1: The Slocum glider used in the iceberg field trial in 2015.

The overall result from this field trial is presented in Figure 4.3. The overall mission last about an hour. The sonar samples covered about 80% of the circumference of the iceberg. The mission was aborted due to limited support vessel time on-site. In post-processing, the trajectory of the glider is first corrected by back-propagating the error between the dead-reckoned surfacing location and the actual measured surface GPS location. The resulting trajectory of the glider in a North-East-Down coordinate is shown in Figure 4.3. The sonar measured ranges are converted into 3 dimensional

points in the North-East-Down coordinate. The iceberg surface is reconstructed using the layered cross-sectional profile that is processed from the three-dimensional point cloud. The detailed procedure of reconstructing the iceberg surface with three-dimensional point cloud presented in Appendix A.2.

Figure 4.2: Collecting GPS coordinates around the iceberg using the 11 meter-long inflatable craft (image credit to Mike Hakomaki)

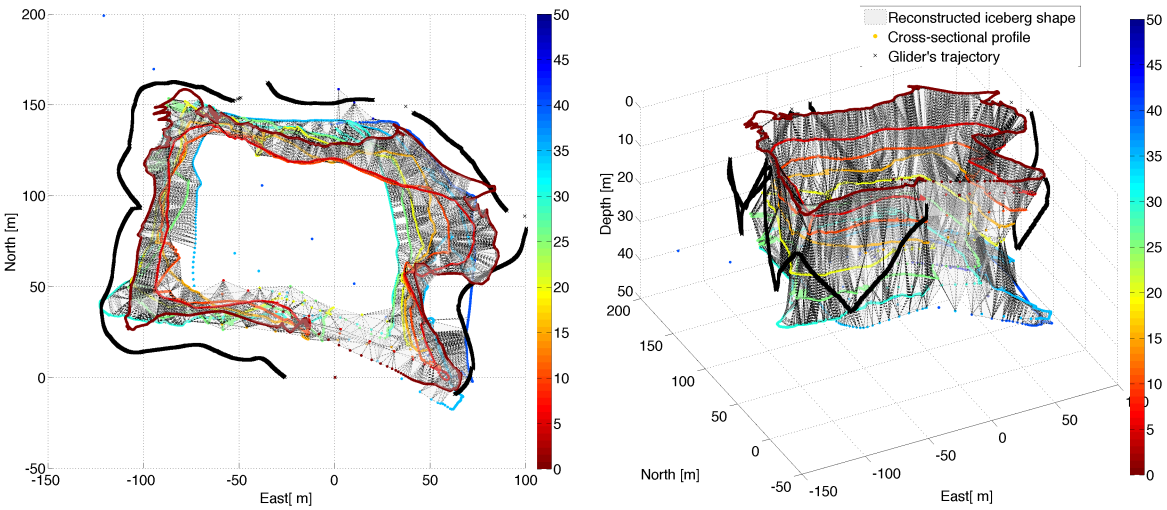


Figure 4.3: Iceberg reconstructed by applying Alpha shape [93] to the smoothed cross-sectional profiles. The trajectory of the Slocum glider is post-processed and shown in black-line.

This field trial showed that the sonar is capable of detecting the iceberg surface, and

that the range extracting function is working well. The glider traveled around the iceberg in about an hour and detected the iceberg surface from up to 50 meters away. Since the vehicle navigation and waypoints are defined in the inertial frame, the presented approach is only suitable for stationary icebergs. Furthermore, the operation is depended on the GPS coordinates collected manually that induce uncertainty in the mission operations and therefore make this approach operationally impractical. Improvements especially in vehicle control are needed in order to expand the capability of the proposed system for profiling floating icebergs.

## 4.2 Preliminary results with a low level adaptive heading controller

In this section an alternative approach is presented. The approach enables the vehicle to follow the iceberg shape by adapting its course during a mission. An adaptive heading controller is designed that uses the ranges measured from the sonar to compute a desired heading for the control system on the glider. The desired heading is intended to guide the vehicle to follow the iceberg surface and to avoidance collisions. The vehicle will be controlled with a desired standoff distance to maintain a consistent sensor footprint on the target.

### 4.2.1 Hardware implementation

A single board computer (SBC) is installed inside the glider. It is used to process the sonar measurements, to compute heading commands based on the sonar data, and to send the updated control commands to the glider computer. The SBC communicates with the sonar and the glider computer using RS485 protocol and RS232 protocol respectively. The sonar configurations, e.g. scanning sector and profile range, are

defined in the glider mission script. These parameters are transmitted to the SBC to configure the sonar during mission initialization. The raw sonar data are stored in a text file in the flash storage on the SBC. The sonar measurements are pre-processed into ranges on the SBC before transmitted to the glider computer. The sonar measured ranges are further processed from acoustic travel-times into physical ranges using local estimates of the speed of sound. Only the sonar ranges and scanning angles are logged on the glider computer co-registered with system time of the glider.

### 4.2.2 Controller design

The heading controller implemented on the SBC computes the desired heading based on the sonar measured ranges and the orientation of the glider. The desired heading is then transmitted to the glider computer as a new desired heading that is included in the native glider heading control loop. Regarding the noise in the sonar measurements induced by the water surface and the seafloor, I defined an active depth and effective sector to exclude those effects (see Figure 4.4. Therefore, the controller only uses the sonar samples when the scanning angle of the sonar is within the effective sector and the vehicle is below the active depth. Meanwhile for mapping purposes, the scanning sector of the sonar can be larger than the effective sector, and is turned on even when the vehicle is above the active depth. As shown in Figure 4.4, the sonar scans the starboard side of the vehicle up and down within the scanning sector with the effective sector shown in blue that has a smaller angle range. By analyzing the measurements from the field trial data presented in the previous section, the minimum active depth is selected to 5 meters and the effective sector is $\pm 5$ degrees off the x-y plane of the vehicle to only include the features above and below the vehicle within 5 meters. When the vehicle is below the active depth, the sonar measurements within the effective sector are used to compute the desired heading. In every sonar

sweep inside the scanning sector, measured ranges, $R_t$, within the effective sector are converted into points $\mathbf{P}_t^v$ in the vehicle coordinate system shown in Figure 4.4 using Equation 4.1 derived in Appendix A.1. The right-hand side of Figure 4.4 shows the associated angles where $\sigma$ is the current scan angle, $\beta$ is the forward-looking angle, and $[x_s^v, y_s^v, z_s^v]^T$ is a vector describing the mounting location of the sonar relative to the origin of the vehicle coordinate system. Since such an offset is relatively small compared to the profiling range of the sonar on a small vehicle, the sonar is assumed to be located at the origin of the vehicle coordinate system.

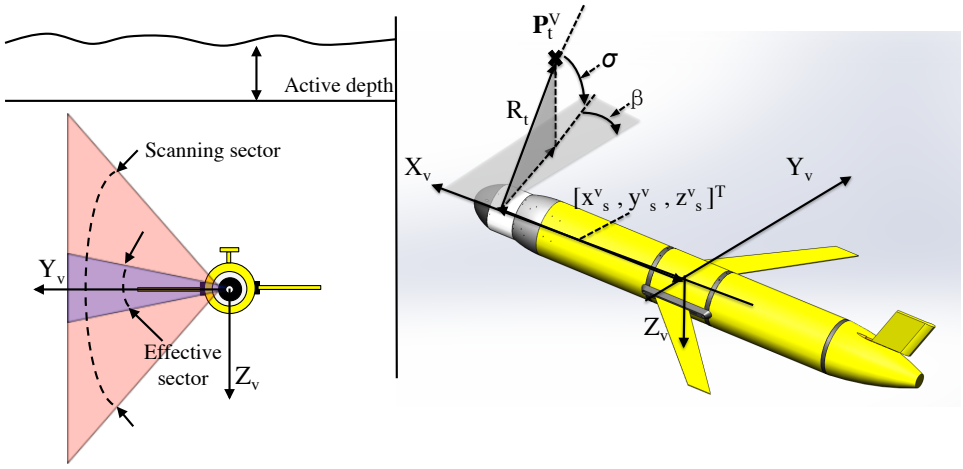


Figure 4.4: The heading controller computes the desired heading using the sonar measurements within the effective sector when the vehicle is under the active depth. Converting a sonar range into a point.

$$\mathbf{P}_t^v = \begin{pmatrix} P_x^v \\ P_y^v \\ P_z^v \end{pmatrix} = \begin{pmatrix} -\cos\sigma \sin\beta \\ \cos\sigma \cos\beta \\ \sin\sigma \end{pmatrix} \cdot R_t + \begin{pmatrix} x_s^v \\ y_s^v \\ z_s^v \end{pmatrix} \tag{4.1}$$

$$\psi_d = K_p(\overline{P_y^v} - S_d) + K_i \sum_{t=1}^{t} (\overline{P_y^v} - S_d) + K_d \frac{d(\overline{P_y^v} - S_d)}{dt} + \psi(t) \tag{4.2}$$

The desired heading ($\psi_d$) is computed using a proportional–integral–derivative (PID) controller applied to $\overline{P_y^v}$ , the averaged value of $P_y^v$ from the effective sector in one

sweep. In Equation 4.2, $S_d$ is the desired standoff distance, $\psi(t)$ is the vehicle heading at time t, $K_p$, $K_i$, and $K_d$ are the gains for the PID controller. Before the controller is activated, the desired heading is obtained from an initial heading defined in the glider mission file. This angle is computed prior to the mission by aligning the glider parallel to the edge of the iceberg that the glider is going to follow initially.

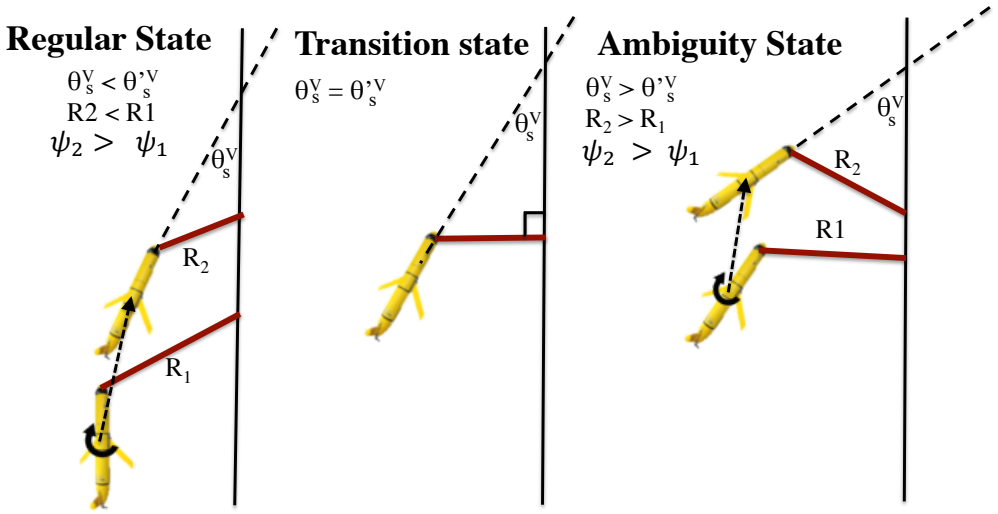


Figure 4.5: Three states defined in the heading controller.

An ambiguity problem is found that causes an increasing sonar range when the glider is turning towards the iceberg. The glider is observed in the ambiguity state when the angle ($\theta_s^V$ in Figure 4.5) from the terrain to the forward direction of the vehicle exceeds a value $\theta_s'^v$ that is determined by the forward-looking angle of the sonar. As shown in Figure 4.5, three states are defined in the heading controller. In the regular state and transition state, the desired heading is computed from Equation 4.2. While in the ambiguity state, the desired heading is calculated by subtracting the current vehicle heading with a constant angle that guides the vehicle turn counter-clockwise towards the regular state. The ambiguity state of the vehicle is identified using the sign of $\Delta\psi \cdot \Delta\overline{P_y^v}$ from two continuous sweeps which is negative in the regular state and positive in the ambiguity state.

### 4.2.3 Controller evaluation in the simulation and in the field experiments

The heading controller is first evaluated in the simulation environment introduced in Chapter 3 on the iceberg r11i01. The iceberg is simulated to be moving at 0.1 m/s toward north. During the simulation, the scanning sector of the sonar is limited to ±45 degrees off the horizontal plane of the vehicle. The sonar is sampling at a frequency of 5 Hz with a forward-looking angle of 35 degrees and a maximum profiling range of 70 meters. The active depth is configured at 5 meters, and the effective sector is ±5 degrees (see Figure 4.4). The motion of the Slocum glider is simulated using a manufacturer supplied glider hardware simulator. The simulator produces a real-time glider operation with simulated sensor outputs and an assumed known ocean current. The simulated glider is programmed to glide at depth between 10 meters to 30 meters using the buoyancy pump.

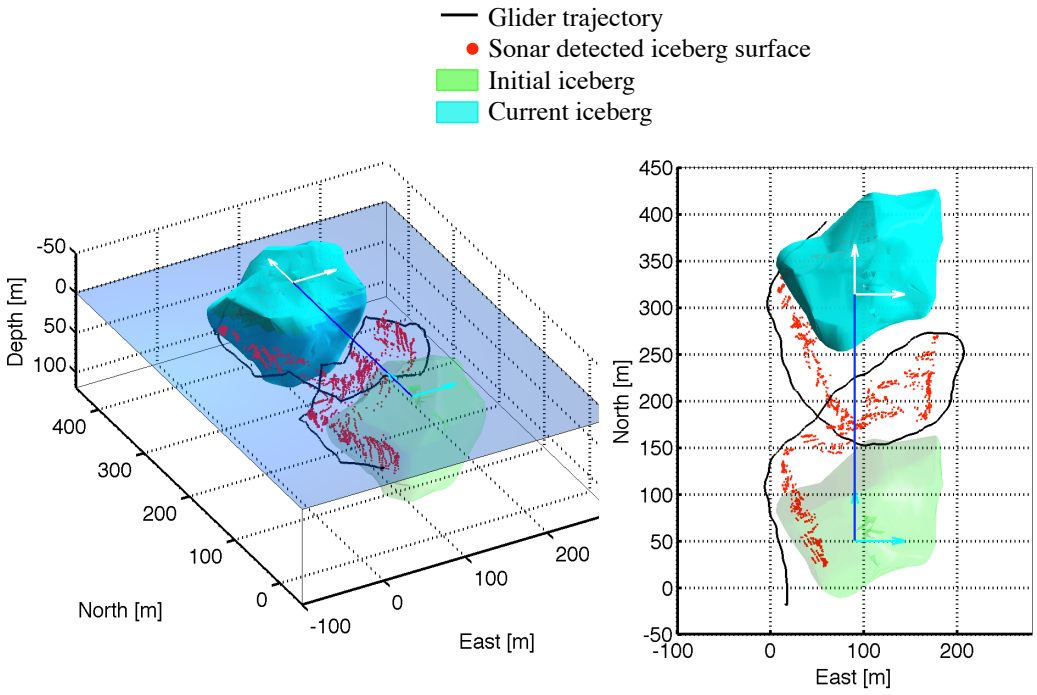


Figure 4.6: Summary of the simulated AUV survey on a moving iceberg.

Figure 4.6 shows the result of the simulation that the glider successfully circumnavigated around the iceberg in 45 minutes. In Figure 4.6, the black line shows the trajectory of the glider, and the red dots are the simulated sonar measurements from the iceberg surface registered in the inertial coordinate system (North-East-Down). The green iceberg and cyan iceberg displayed in Figure 4.6 show the simulated starting and ending location of the iceberg with the blue line indicating the traveled path of the iceberg. The simulated vehicle successfully circumnavigated around the iceberg with the designed controller.

In July 2015, the Slocum glider shown in Figure 4.1 was deployed near a grounded iceberg in Conception Bay, Newfoundland, Canada. The implemented heading controller computes the desired heading using sonar measurements within the effective sector of $\pm 5$ degrees when the vehicle is below the depth of 5 meters. The deployment was conducted by four people using a rigid-hull inflatable boat (RHIB). The glider was gliding between the depth from 5 meters to 25 meters and programmed to surface every 12 minutes for user communication and acquiring position update from the GPS. Except for mission #3 which has no sonar measurements from the iceberg, the glider detected the iceberg and adapted its heading towards the iceberg in the mission #1, #2, and #4.

As introduced in Chapter 2, the glider's position is estimated based on the dead-reckoning method. As a result of the integration, the unknown environmental influences accumulate over the submerged period, causing a bias between the dead-reckoned position and the actual location. In post-processing, the dead-reckoning trajectory is recalculated including the assumed ocean current derived from the distance between the dead-reckoning surface locations and the actual GPS fixes. For each mission, the trajectory is first post-processed in the Local Mission Coordinate (LMC) where the x-axis is pointed at the magnetic north, and the origin is at the

start location for the mission. The magnetic declination is used to convert the overall trajectory into the Universal Transverse Mercator (UTM) coordinate system, then into the Longitude-Latitude coordinate system using the functions introduced in [87]. The comparison between the dead-reckoned location during the missions and the post-processed trajectory is shown in Figure 4.7.

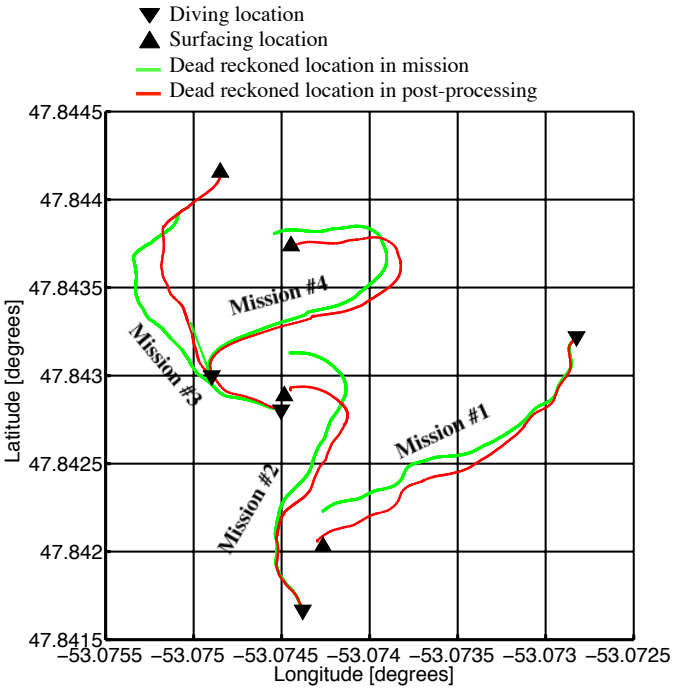


Figure 4.7: Comparison between the dead-reckoned trajectories and the post-processed trajectories in the iceberg field trial

After the trajectories of the vehicle are corrected, the ranges measured by the sonar are converted into the vehicle coordinate. Then, $\mathbf{P}_t^v$ are converted into the UTM coordinate system using the corresponding position and orientation of the vehicle (See Appendix A.1 for detail). The outliers are cleaned manually in MeshLab software [104]. To reconstruct the iceberg shape, the data points are separated into horizontal cross-sectional profiles at incremental depth. The profiles are smoothed with a moving average method [105] and then are interpolated for denser and smoother profiles.

Finally, the Alpha Shape [93] is applied to the resulting three-dimensional points to construct the iceberg surface. The resulting iceberg surface constructed using the data points are shown in cyan in Figures 4.8 and 4.9. The overall iceberg-profiling mission was aborted after mission #4 finished due to a malfunction in the glider system. As a result, the eastern face of the iceberg was not fully covered.

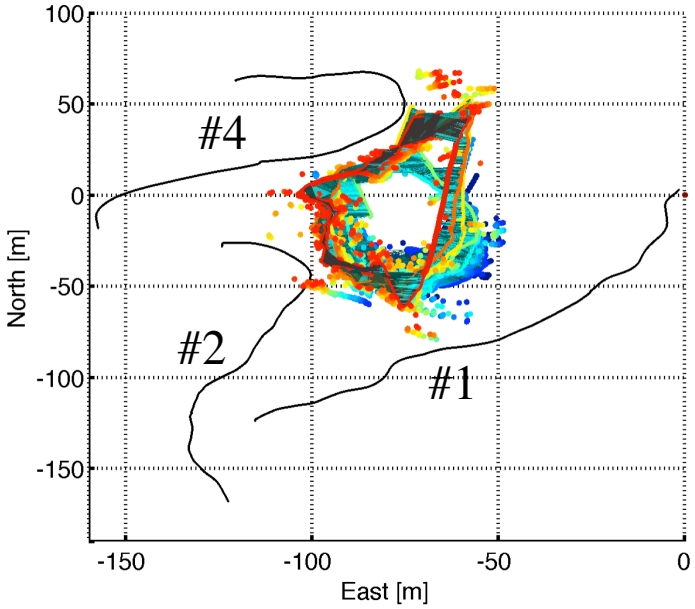


Figure 4.8: Top view of the iceberg reconstruction result using Alpha shape [93] with smoothed cross-sectional profiles. The trajectory of the Slocum glider is the black-line

Due to the imperfect gain tuning for the PID controller for the actual field performance of the vehicle, significant overshoots are found in the mission #2 and mission #4. Furthermore, the heading controller is not sufficiently fast in turning the glider at the iceberg corners. This can be attributed to slower than expected vehicle turning rates. The turning rates modeled in the vehicle hardware simulator were consistently faster than the ones experienced in actual operations. The heading of the Slocum glider is adjusted by a small control surface on the tail-fin. The turning rate in the actual environment is lower than the modeled vehicle dynamics in the hardware simulator. As an outcome of these trials, it was shown that it was necessary to develop a more

sophisticated controller to better guide the vehicle to follow the iceberg shape.

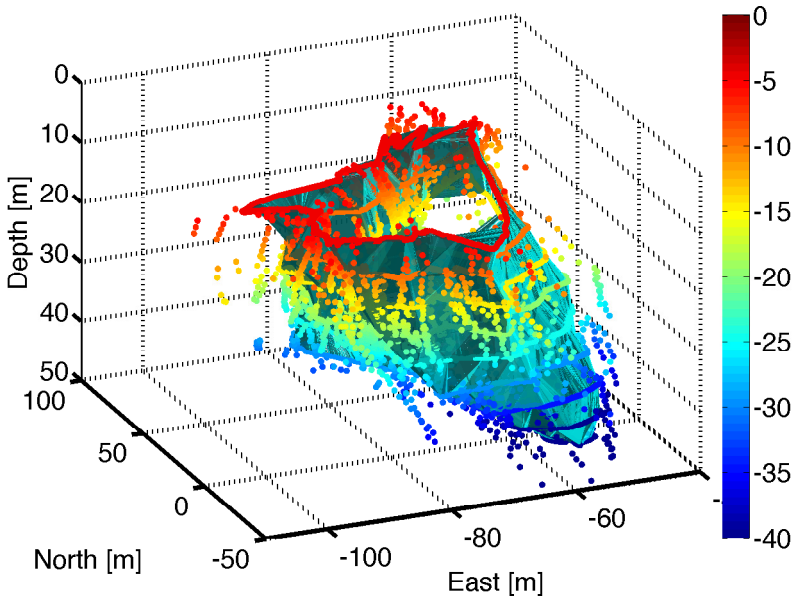


Figure 4.9: Perspective view of the iceberg reconstruction using Alpha shape [93] with smoothed cross-sectional profiles(colored contour lines).

## 4.3 Advanced GNC for iceberg survey

An advanced GNC is designed and is implemented on a SBC running Linux Operating System. In the advanced GNC design for iceberg survey, three phases are defined in the system. At the beginning of the mission, the glider is operated in the iceberg search mode. After consistent iceberg returns are detected, the glider will switch into the profile-following mode. In case the glider loses track of the iceberg, for example at sharp corners that may exceed the minimum turning radius of the glider, the glider control mode will be switched to iceberg relocating mode. The mode switching is executed automatically based on the sonar measurements from the most recent scans. The designed GNC is validated both in simulation and in the field.

### 4.3.1 Iceberg search mode

Figure 4.10 shows the flow chart of the GNC in the iceberg searching mode. Before the glider is deployed, an initial heading ($\psi_i$) is programmed in the mission file that is measured by pointing the glider parallel to the portion of iceberg edge. The glider is then deployed at a distance away from the iceberg and pointed in the direction of the initial heading. The active depth ($z_e$) and effective sector ($[\sigma_L, \sigma_H]$) introduced in the previous section are also included in the GNC design to avoid surface returns at shallow depth.

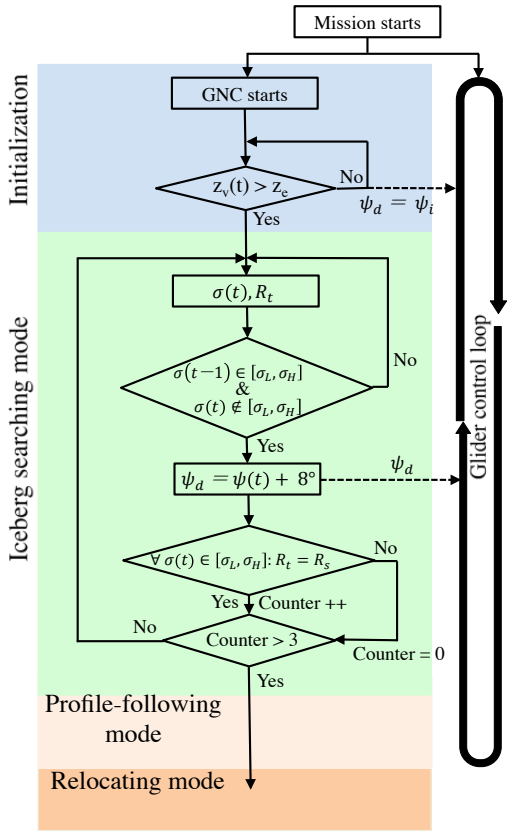


Figure 4.10: Iceberg searching mode flowchart.

During the descent from the surface to the $z_e$, the glider will fly at the reprogrammed heading. Once the glider is below the active depth, the glider will be operated in the iceberg searching mode to intersect the target iceberg. The GNC computes new

desired headings for the existing heading controller on the vehicle. A new desired heading is commanded to the glider when the sonar finished a full scan in the effective sector. If the sonar does not detect any target in the effective sector, the desired heading is then set to be equal to the current heading of the glider plus 8 degrees. This change in desired heading will turns the vehicle towards the iceberg at a rate of 0.25 degrees/second which is equivalent to a circular trajectory with a radius of about 115 meters. Meanwhile, a counter keeps track of detected obstacles in the effective sector. In contrast, if no obstacle is detected in the current scan in the effective sector, the counter will be cleared to zero. For our application, the glider will be switched from the iceberg search mode to the profile-following mode only if the counter is larger than 3. In other words, the iceberg profile-following mode will be activated if the iceberg surface was consistently detected in three consecutive scans. The threshold of the counter for switching the controller mode is defined based on the vehicle speed, sonar configuration, and the desired standoff distance.

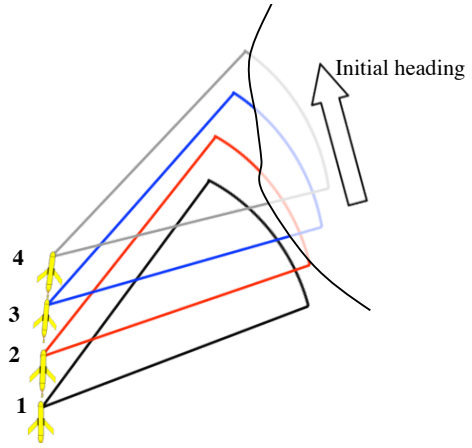


Figure 4.11: The fan shaped beams with $\sigma(t) = 0$ in four continuous scans.

The sonar with a beamwidth of $\delta$ is configured at a forwarding-looking angle $\beta$ on the vehicle. Figure 4.11 shows the fan-shaped beams when the scanning angle $\sigma(t) = 0$ in four continuous scans. No object is detected at location 1 because the iceberg is

outside the sonar's profiling range, but a consistent iceberg surface is detected in the three following scans. For a safe operation, the distance the vehicle has traveled before switched into the profile-following mode, i.e. from location 1 to 4, should be smaller than the forward-looking distance at the last location where no object is detected, i.e. location 1. Equation 4.3 to 4.4 show such safety concern in choosing the appropriate threshold (N). Using the system configurations summarized in Table 4.1, N is set equal to 3 in order to satisfy the safety requirement mentioned.

$$N \cdot \frac{SS}{\Delta\sigma \cdot f} \cdot V < \min(D_f) \tag{4.3}$$

$$D_f = R_s \cdot \sin(\beta + \delta) \tag{4.4}$$

Table 4.1: System configurations

| Name | Symbol | Size | limit |
|---|---|---|---|
| Scanning sector [degrees] | $SS$ | 90 | [-45, 45] |
| Sonar stepping angle [degrees] | $\Delta\sigma$ | 1.8 | |
| Averaged vehicle speed [m/s] | $V$ | 0.5 | |
| Averaged ping-rate [Hz] | $f$ | 4 | |
| Forward-looking distance [meters] | $D_f$ | | [21.0, 55.5] |
| Sonar profiling range [meters] | $R_s$ | 70 | |
| Forward-looking angle[degrees] | $\beta$ | 35 | |
| Beamwidth [degrees] | $\delta$ | 35 | [-17.5, 17.5] |

### 4.3.2 Iceberg relocating mode

Once the glider is controlled in the profile-following mode, the glider has to respond to any sharp terrain variations. In order to turn the vehicle at a higher rate to follow any sharp corners on icebergs, the iceberg relocating mode is defined in the GNC. The relocating mode can only be activated from profile-following mode when no object is detected within the effective sector in the three continuous sonar scans as shown in the flow chart in Figure 4.12.

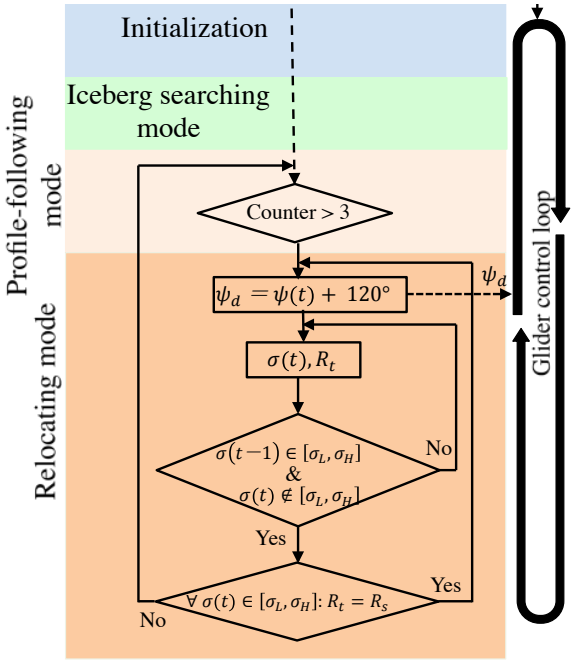


Figure 4.12: The flow char of switching between profile-following mode and relocating mode.

The number of empty scans before entering the iceberg relocating mode is chosen based on the same criteria in choosing the counter threshold in the iceberg searching mode. When the vehicle is in the iceberg relocating mode, the GNC will command the desired heading that is 120 degrees larger than the current heading of the vehicle to turn towards the starboard side. The Slocum glider can move at a turning rate of 1.5 degrees per second which is equivalent to a 20 meters turning radius at a speed of about 0.5 m/s. If any object is detected from the sonar scans in the effective sector during the turning, the glider will exit the relocating mode and return to the iceberg profile-following mode.

### 4.3.3 Iceberg profile-following mode

In the iceberg profile-following mode, the GNC uses a series of subsequent sonar scans within the effective sectors to compute the desired headings to control the vehicle to

follow the trend of the iceberg profile. The GNC in profile-following mode consists of a vehicle-attached occupancy map (VOM) in order to estimate the iceberg profile and generate a desired path; a dynamic inverse-sonar model to compensate the uncertainty in the sonar measurements and update the VOM; and a line-of-sight path-following algorithm to compute the desired heading based on the desired track from VOM.

#### 4.3.3.1 Occupancy grid maps

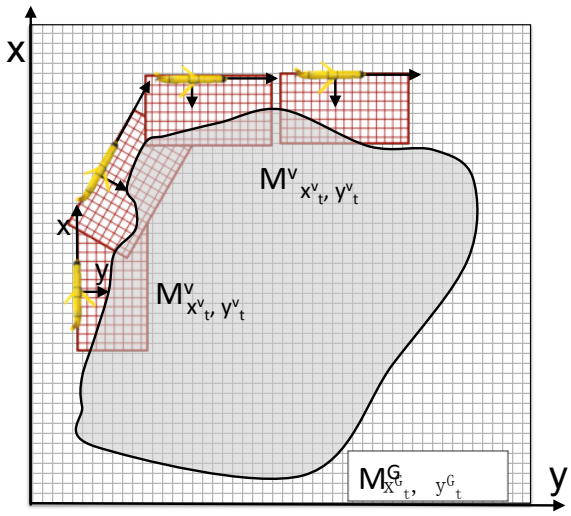


Figure 4.13: Global occupancy map (GOM) and vehicle-attached occupancy map (VOM)

Figure 4.13 shows the two types of gridded occupancy maps used in our research for displaying the two-dimensional underwater environment around the vehicle. A global occupancy map (GOM), $M^G_{x^G_t, y^G_t}$, depicts the iceberg measurements in an inertial coordinate, while the vehicle-attached occupancy map (VOM), $M^v_{x^v_t, y^v_t}$, displays the iceberg profile relative to the vehicle with its origin located at the center of buoyancy of the vehicle. A probability of occupancy ranging from zero to one is associated with each cell $(x^G_t, y^G_t)$ and $(x^v_t, y^v_t)$ to present the possibility of occupancy or emptiness. Thus, we define $P(M^G_{x^G_t, y^G_t} | R_1, ..., R_t)$ and $P(M^v_{x^v_t, y^v_t} | R_1, ..., R_t)$ to be the probability of

occupancy of the cell $(x_t^G, y_t^G)$ and $(x_t^v, y_t^v)$ updated from the sonar measured ranges from time 1 to time t.

As shown in Figure 4.13, only the environment on the starboard side of the vehicle is included in the VOM because the sonar is oriented to have a forward-looking angle on the starboard side resulting in a backward-looking angle on the opposite side. Therefore, the vehicle is limited to circumnavigate icebergs in the clockwise direction. Due to the change in the location and orientation of the vehicle from time t-1 to t, a cell in the $M^v_{x^v_{t-1}, y^v_{t-1}}$ has to be projected into $M^v_{x^v_t, y^v_t}$ prior to the update from a sonar measured range at time t.

Equations 4.5 to 4.7 show the conversion from $x^v_{t-1}, y^v_{t-1}$ to $x^v_t, y^v_t$. As a consequence, the probability of occupancy $P(M^v_{x^v_{t-1}, y^v_{t-1}} | R_1, ..., R_{t-1})$ is projected to $P(M^v_{x^v_t, y^v_t} | R_1, ..., R_{t-1})$. After that, the inverse-sonar model is used to update $P(M^v_{x^v_t, y^v_t} | R_1, ..., R_{t-1})$ to $P(M^v_{x^v_t, y^v_t} | R_1, ..., R_t)$ and $P(M^G_{x^G_t, y^G_t} | R_1, ..., R_{t-1})$ to $P(M^G_{x^G_t, y^G_t} | R_1, ..., R_t)$ based on the log-odds using the Bayes' theorem [106].

$$\begin{bmatrix} \Delta x_t^{t-1} \\ \Delta y_t^{t-1} \end{bmatrix} = \begin{bmatrix} \cos\psi_{t-1} & \sin\psi_{t-1} \\ -\sin\psi_{t-1} & \cos\psi_{t-1} \end{bmatrix} \begin{bmatrix} x(t) - x(t-1) \\ y(t) - y(t-1) \end{bmatrix} \tag{4.5}$$

$$\begin{bmatrix} x_t^v \\ y_t^v \end{bmatrix} = \mathbb{M} \cdot \begin{bmatrix} x_{t-1}^v - \Delta x_t^{t-1} \\ y_{t-1}^v - \Delta y_t^{t-1} \end{bmatrix} \tag{4.6}$$

$$\mathbb{M} = \begin{bmatrix} \cos(\psi(t) - \psi(t-1)) & \sin(\psi(t) - \psi(t-1)) \\ -\sin(\psi(t) - \psi(t-1)) & \cos(\psi(t) - \psi(t-1)) \end{bmatrix} \tag{4.7}$$

The calculation of the log-odds of a cell in an occupancy map $P(M_{x_t, y_t} | R_1, ..., R_{t-1})$ is shown in Equation 4.8. The log-odds at index $(x_t, y_t)$ is then updated in Equation 4.9 using an inverse-sonar model. In our sonar configuration, the wide beamwidth is aligned in the moving direction of the vehicle. Unlike the multi-beam sonar, the

echo intensity received at different angles relative to the transducer is not available. Therefore, uncertainty in resolving the location of the target at the measured ranges within the angular sonar spreading angle appears. A dynamic inverse-sonar model will be introduced in the following section It accounts for the incident angle of the sonar rays with a potential iceberg surface. The dynamic inverse-sonar model is used to update the log-odds in Equation 4.9 in our research. Alternatively, a simpler static inverse-sonar model could be used as described in [108]. A comparison between this two models will be discussed in the Section 4.3.4. In Equation 4.9, $P(M_{x_t,y_t}|R_t)$ is the probability of occupancy derived from the inverse-sonar model, $l_{x,y}^{t-1}$ is the log-odds based on the sonar measured range from time 1 to t-1, and $l_{x,y}^{0}$ is the initial log-odds assumed by the user. For example, $l_{x,y}^{0}$ is equal to zero if the probability of occupancy of the cells in the VOM are initialized with 0.5 in Equation 4.8. After the log-odds is updated with the sonar measurements, the updated probability of occupancy is calculated in Equation 4.10.

$$l_{x,y}^{t-1} = \log \frac{P(M_{x_t,y_t}|R_1, ..., R_{t-1})}{1 - P(M_{x_t,y_t}|R_1, ..., R_{t-1})} \tag{4.8}$$

$$l_{x,y}^{t} = \log \frac{P(M_{x_t,y_t}|R_t)}{1 - P(M_{x_t,y_t}|R_t)} + l_{x,y}^{t-1} + l_{x,y}^{0} \tag{4.9}$$

$$P(M_{x_t,y_t}|R_1, ..., R_t) = 1 - \frac{1}{1 + e^{l_{x,y}^{t}}} \tag{4.10}$$

The effective sector $[\sigma_L, \sigma_H]$ is introduced to control the update on VOM and GOM. With this feature, only the targets close to the depth of the vehicle are included. Due to this, obstacles outside the effective sector, such as the surface returns and the seafloor returns, are excluded in order to avoid unnecessary reactions. In our case, the effective sector is set to $[-5, 5]$ to cover the obstacles within the 5 meters

above and below the vehicle. The desired trajectory will be generated from the most updated VOM every time the sonar swept the effective sector. The overall procedures of updating the VOM are summarized as follows

1. VOM is initialized, i.e. $P(M^v_{x^v_0,y^v_0}) = 0.5$ and $l^0_{x,y} = 0$;
2. vehicle moved from $x(t-1), y(t-1)$ to $x(t), y(t)$ with the heading changed from $\psi(t-1)$ to $\psi(t)$;
3. if $\sigma(t) \in [\sigma_L, \sigma_H]$ then go to step 4) to update the VOM, else jump to step 10);
4. project $P(M^v_{x^v_{t-1},y^v_{t-1}}|R_1, ..., R_{t-1})$ to $P(M^v_{x^v_t,y^v_t}|R_1, ..., R_{t-1})$ with Equation 4.5 to 4.7 based on the change of vehicle's location and orientation ;
5. calculate $l^{t-1}_{x,y}$, the log-odds of $P(M^v_{x^v_t,y^v_t}|R_1, ..., R_{t-1})$, in Equation 4.8;
6. a sonar measured range $R_t$ is obtained at time t;
7. calculate $P(M^v_{x^v_t,y^v_t}|R_t)$, the probability of occupancy from an inverse-sonar model;
8. update the log-odds in the VOM, $l^t_{x,y}$, using Equation 4.9;
9. calculate $P(M^V_{x^v_t,y^v_t}|R_1, ..., R_t)$, the update probability of occupancy from $l^t_{x,y}$ using Equation 4.10;
10. if $\sigma(t) \notin [\sigma_L, \sigma_H]$ and $\sigma(t-1) \in [\sigma_L, \sigma_H]$, calculate the desired trajectory from the VOM for line-of-sight path follower;
11. repeat the step 2) to 10).

GOM is updated in a similar process except for step 4) because the GOM is not attached to the vehicle. Step 10) is also not applicable to update GOM since the GOM is not used to compute the desired vehicle trajectory. The GOM, a relatively large

map, is recommended to be generated in post-processing than during the mission. Since the iceberg may move from its original location, the profile extracted from the GOM may be different from the actual iceberg profile. Moreover, the GOM is constructed based on the location of the vehicle from time 1 to time t where an accumulated error between the dead-reckoned location and the actual locations may exist, causing an error in representing the iceberg profile. Once the vehicle trajectory is corrected in the post-processing, the GOM can be updated to present the profile of a stationary object. In contrast, the VOM is relatively small. The navigation errors have fewer effects in estimating the local profile of the target.

#### 4.3.3.2 Dynamic inverse-sonar model

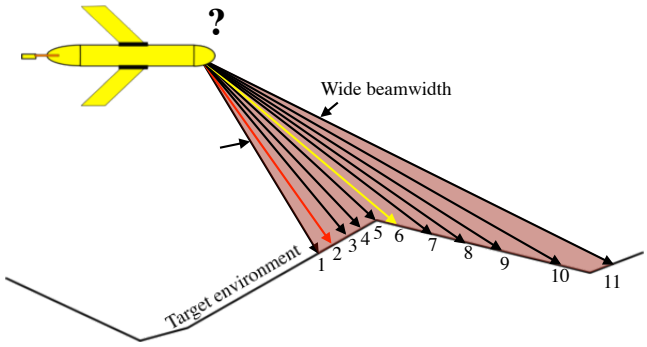


Figure 4.14: The sonar is oriented with a wide beamwidth align along the vehicle's traveling direction. The sound is emulated as rays.

As mentioned, the sonar is oriented to scan at a forward-looking angle of 35 degrees on the starboard side. As a result, the wide beamwidth is aligned with the AUV's traveling direction as shown in Figure 4.14. A range measurement is processed from the echo intensities received by the sonar. However, the information about the directionality of the incoming sound beyond the mechanical orientation of the transducer is not available. Therefore, the assumption used in the general sonar model that the sound is coming along the central ray, i.e. ray #6 in Figure 4.14, was causing an

error in estimating the profile of the target. The maximum echo intensity may not be observed at range where ray #6 intersects the terrain, because of a small incident angle. It will have a potential negative impact in controlling the vehicle to follow the real terrain accurately.

$$EI = SL + DI + 2TL + 2AL + TS \tag{4.11}$$

$$P_{EI}(\delta) = P_{SL} \cdot P_{TL}^2 \cdot P_{AL}^2 \cdot P_{DI}(\delta) \cdot P_{TS}(\delta) \tag{4.12}$$

$$\frac{\mathrm{d}P_{EI}(\delta)}{\mathrm{d}\delta} = P_{SL} \cdot P_{TL}^2 \cdot P_{AL}^2 \cdot \frac{\mathrm{d}(P_{DI}(\delta)P_{TS}(\delta))}{\mathrm{d}\delta} \tag{4.13}$$

In a ray-tracing sonar model [96], the sound propagation is simulated with several rays within the beamwidth as shown in Figure 4.14. In an uniform medium where the sound is traveling at a consistent speed, the lengths of the rays are equal to the range the sound has propagated. The principal of the ray-tracing sonar model is the sonar equation [94] shown in Equation 4.11 in units of dB. Equation 4.12 can then be derived from Equation 4.11 by changing the units from dB to power. The terms in Equation 4.11 were introduced in Chapter 3 where $SL$ represents the source level of the sonar relative to the power applied to the transducer; $DI$ is the directivity index of the sonar that varies at different ray angles ($\delta$); the transmission loss ($TL$) due to the increase of ensonified area over the range is included in $TL$; the attenuation loss, $AL$, includes the energy dissipated into the medium during the propagation. The $TL$ and $AL$ are doubled to include the two-way energy loss. When the sound waves strike a target, part of the energy is absorbed by the target and is deflected in other directions, while the remaining energy is reflected back towards the sonar. The energy loss during the contact with the target is formulated as target strength ($TS$).

In those terms, the $SL$ is consistent for different rays, and the $TL$ and $AL$ do not significantly differ between rays since the traveling distance of the rays are similar from the sonar to a target. In contrast, directivity ($DI$) and target strength ($TS$) vary for individual rays due to the beam pattern of the transducer and different incident angles ($\theta_i$) when the rays intersect with the terrain. Therefore, $P_{DI}(\delta)$ and $P_{TS}(\delta)$ are the terms left when differentiating the $P_{EI}(\delta)$ with respect to $\delta$ (see Equation 4.13).

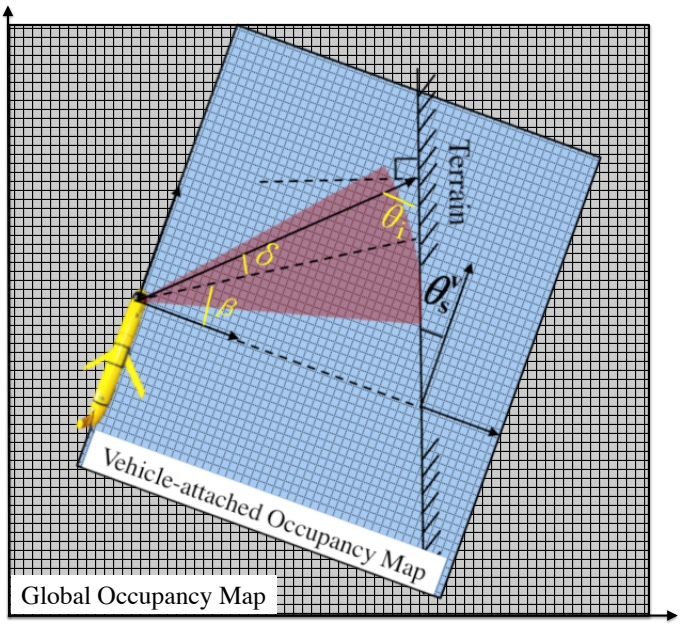


Figure 4.15: A simulated ray intersects with the terrain. The sound propagation inside the beamwidth is displayed as a red fan shape.

In the two-dimensional space shown in Figure 4.15, $P_{DI}(\delta)$ is expressed in Equation 4.14, where $k$ is the wave number and $h$ is the length of the transducer. Equation 4.15 shows the target strength in units of power, $P_{TS}(\delta)$, for a large object, such as seafloor or iceberg. Equation 4.15 is derived from Equation 4.16 according to [94], where $\mu$ is the scattering constant which can be determined empirically through experiments, and $\theta_i$ is the incident angle. Figure 4.15 shows the propagation path of a ray which intersects with the terrain at an incident angle of $\theta_i$ with the sonar oriented forward

at an angle $\beta$. With the known forward-looking angle of the sonar ($\beta$), the angle of the individual ray ($\delta$), and the terrain slope relative to the vehicle ($\theta_s^v$), the incident angle $\theta_i$ is calculated as shown using Equation 4.17.

$$P_{DI}(\delta) = \frac{\sin(\frac{kh}{2}\sin\delta)}{\frac{kh}{2}\sin\delta} \tag{4.14}$$

$$P_{TS}(\delta) = \mu \sin^2\theta_i(\delta) \tag{4.15}$$

$$TS = 10\log_{10}\mu + 10\log_{10}\sin^2\theta_i \tag{4.16}$$

$$\theta_i(\delta) = 90 - (\beta + \delta + \theta_s^v) \tag{4.17}$$

$$P_o(\delta, R) = \begin{cases} 0, & \text{if } R < R_t \& R_t < R_s \\ \frac{P - \min\{P\}}{2(\max\{P\} - \min\{P\})} + 0.5, & \text{if } R = R_t \& R_t < R_s \\ 0, & \text{if } R_t = R_s \end{cases} \tag{4.18}$$

$$P = P_{DI}(\delta) \cdot P_{TS}(\delta) \tag{4.19}$$

In Equation 4.18, probabilities of occupancy, $P_o(\delta, R)$, along the propagation of the rays are defined. For all ranges smaller than the extracted object range $R_t$ the probabilities of occupancy is assumed to be zero for all rays. At the measured range $R_t$, a probability distribution ranging from 0.5 to 1 is assigned on the rays within the beamwidth. The distribution is calculated from $P_{DI}$ and $P_{TS}$ in Equation 4.19. If the range extracted is the maximum profiling range ($R_s$), the probability is assumed to be zero at all rays for the entire ranges including $R_s$. The rays with a computed incident angle of less or equal to zero, i.e. the relative direction of propagation is

parallel or diverging from the trend of the terrain, are assumed to have a probability of occupancy of 0.5 at range $R_t$. Figure 4.16 shows such probability distribution for different ray angles ($\pm 17.5^o$) and different terrain trend ($\theta_s^v$) with forward-looking angles of zero and 35 degrees.

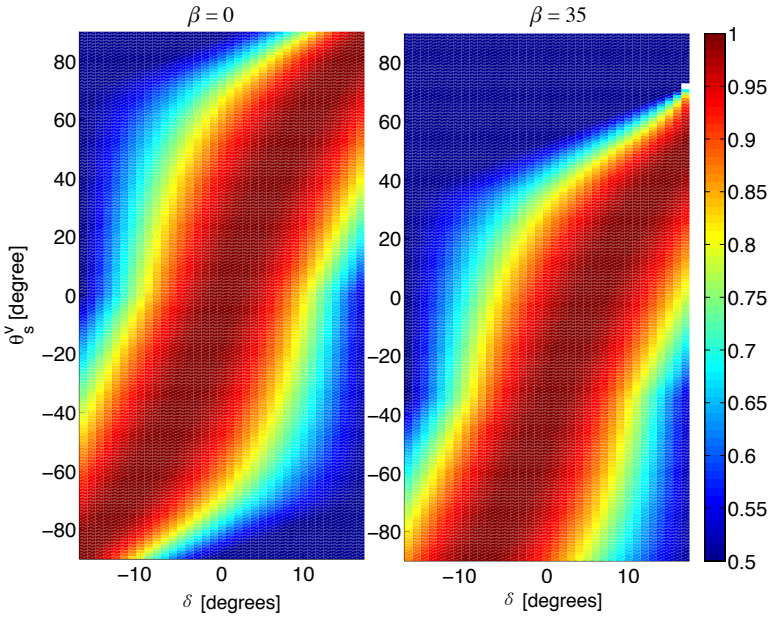


Figure 4.16: Probability of occupancy with different ray angles at different terrain slopes when $R = R_t$. The forwarding looking angle is 0 degrees(left) and 35 degrees (right). Colorbar displays the probability of occupancy from 0.5 to 1.

To update the VOM introduced in Section 4.3.3.1, $P_o(\delta, R)$ is converted into $P(M^v_{x_t^v, y_t^v}|R_t)$. The calculation of $x_t^v, y_t^v$ with a known $\delta$, $\beta$ and $R$ is included in Appendix A.1. Since $\theta_s^v$ is required by Equation 4.18, it is initially assumed to be zero. Subsequently, it is computed as follows. To estimate $\theta_s^v$, the polynomial regression is applied on the location of the selected cells $(x_t^v, y_t^v)$ in the VOM with $P(M^v_{x_t^v, y_t^v}|R_1, ..., R_t) > 0.5$. In order to get a valid estimate of $\theta_s^v$, the algorithm is only applied if at least 5 occupied cells ahead of vehicles, otherwise, $\theta_s^v$ is assigned to zero.

To evaluate the process of updating the VOM using the dynamic inverse-sonar model, the vehicle was simulated to move at a constant speed of 0.5 m/s on a straight line

40 meters away from a flat wall. An example of the VOM is shown in Figure 4.17. The green squares show the $(x_t^v, y_t^v)$ selected for estimating the trend of the terrain in first-order polynomial regression (Equation 4.20). The red line in Figure 4.17 shows the resulting track (Equation 4.21) when applying a first-order polynomial regression on the selected cells.

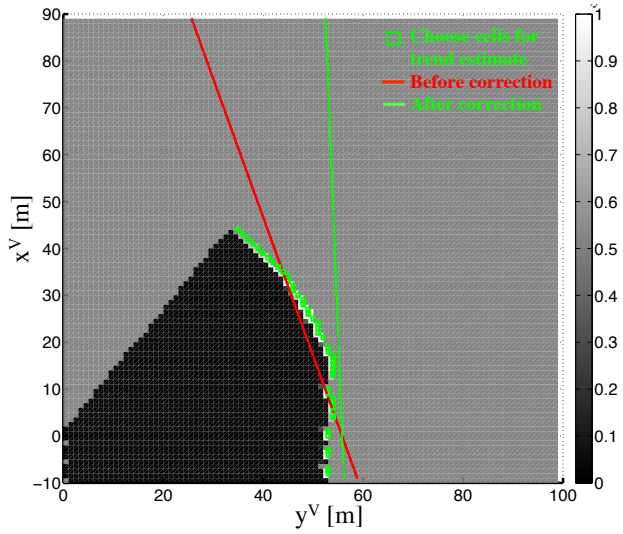


Figure 4.17: An example of VOM. The paths are generated from the indices of the chosen cells shown in green sqaures. Red line is from Equation 4.21,and green line is from Equation 4.23

$$[b_1, b_0] = pfit(x_t^v, y_t^v) \tag{4.20}$$

$$y'^v = b_1 \cdot x'^v + b_0; \tag{4.21}$$

$$\theta_s^G = \arctan(b_1) + \psi(t) \tag{4.22}$$

The trend of the terrain in an inertial frame can be calculated using Equation 4.22 based on the heading of the vehicle and $b_1$. The red squares in Figure 4.18 show

the $\theta_s^G$ estimated from the VOM. A steady-state angle-offset about $16.57^o$ is found between the estimated and the actual trend of the wall (zero degrees). The bias is caused by the forward-looking angle that the occupied cells form an arc shape in the VOM. Therefore, a constant compensation is applied in estimating the trend of the wall from the polynomial regression. In Figure 4.17, the newly estimated terrain in the VOM from Equation 4.23 is shown in green line. Figure 4.18 shows results from two simulations. The red curve is generated using the original algorithm (Equation 4.22), while the blue curve is generated by removing the bias (see Equation 4.24). From this figure one can see better agreement with the actual slope. Therefore, the terrain slope in the VOM, $\theta_s^v$, is calculated in Equation 4.24.

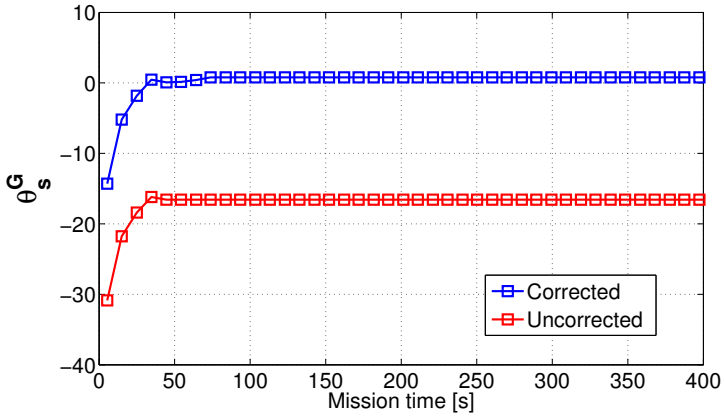


Figure 4.18: Comparison of the trend of the wall, $\theta_s^G$, before and after the bias is corrected

$$y'^v = \tan(arctan(b_1) + 16.57^o) \cdot x'^v + b_0 = \frac{b_1 + \tan(16.57^o)}{1 - b_1 \cdot \tan(16.57^o)} \cdot x'^v + b_0; \qquad (4.23)$$

$$\tan(\theta_s^v) = \frac{b_1 + \tan(16.57^o)}{1 - b_1 \cdot \tan(16.57^o)} \qquad (4.24)$$

#### 4.3.3.3 Line-of-sight path following using VOM

By applying polynomial regression on the occupied cells (green squares in Figure 4.19), the wall shape of the obstacle is generated and shown in Figure 4.19. The red, blue and yellow curves show the estimated profile of the obstacle from first-order, second-order and third-order polynomial regressions.

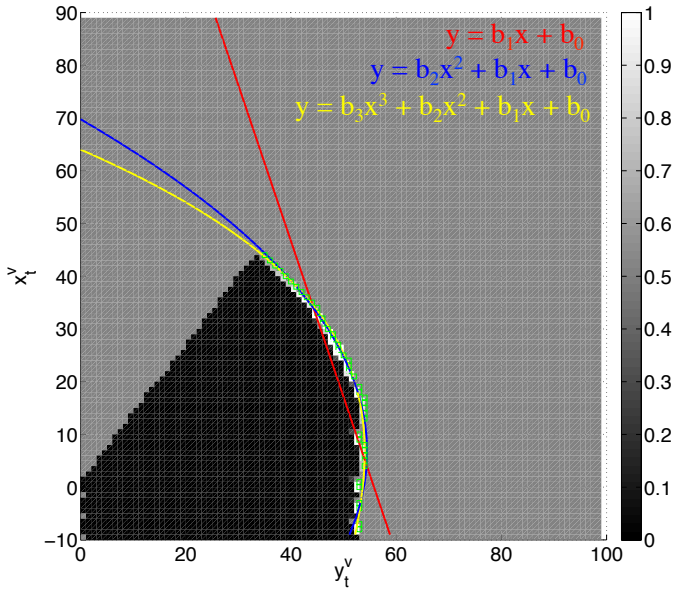


Figure 4.19: The three path (red, blue and yellow) are generated from applying the different polynomial approximations (1st, 2nd and 3rd orders) to the indices of the occupied cells (green squares).

Although the resulting curves from higher order polynomials show better agreements on the location of occupied cells, it takes more time to compute the regression coefficients and is more complicated for the chosen guidance law, line-of-sight (LOS). The Slocum glider has a relative slow dynamic, the control parameters are updated at about 4 seconds. Due to the motion constraints, the vehicle cannot response to high curvature profiles varying at a high frequency. The computational benefits of determining the polynomial coefficients as well as the simplified implementation of a line-of-sight trajectory following algorithm make the first order polynomials more

attractive. For more details on the LOS algorithm, the reader is referred to [36] to[40] for the application of the LOS approach to a curved desired path.

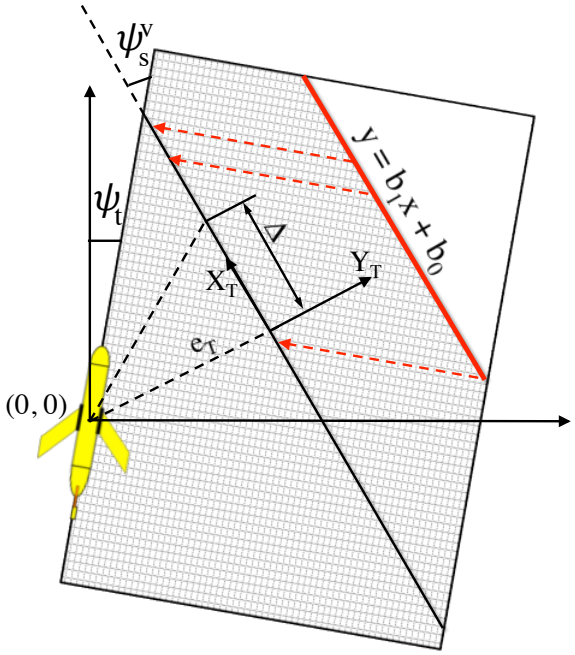


Figure 4.20: The desired track, $X^T - Y^T$,is generated by shifting the estimated wall shape of the obstacle ($y = b_1x + b_0$). The objectives of the forward-looking LOS is to minimize the cross-track error ($e_T$), and to align the vehicle with the trend of the desired track ($\psi_s^v = 0$).

As shown in Figure 4.20, the vehicle by definition is located at the origin of the VOM. The desired path is generated by shifting the estimated terrain profile ($y = b_1x + b_0$) by the desired standoff distance in the VOM. For a straight-line path, one can easily compute the cross-track error, $e_T$, by expressing the vehicle's coordinates in a track attached coordinate system, e.g. $X^T$–$Y^T$ shown in Figure 4.20. Therefore, the glider's coordinate in the $Y_T$ direction expresses the shortest distance to the path, cross-track error. In the looking-ahead LOS control, a forward-looking distance ($\Delta$) is defined by the user. The desired heading referred in the VOM, $\chi^V(e_T)$, can be calculated as shown in Equation 4.25 in order to satisfy the control objectives [39] stated in Equation 4.26. To provide more control over the error system dynamics, Equation

4.25 can be expanded into Equation 4.27 where the argument of the arctan shows the elements of a PID controller. In the $X^T - Y^T$, a right-hand-side coordinate system, shown in Figure 4.20, $e_T$ is defined to be negative when the vehicle is on the left-hand-side of the desired path where the vehicle requires a positive turning command to follow the desired path. Thus, a negative sign is added on $e_T$ in Equation 4.25 and subsequently to Equation 4.27. Since the desired heading commanded to the vehicle is based on an inertial coordinate system, the desired heading is obtained by offsetting the relative heading, $\chi^V(e_T)$, with the vehicle's current heading, $\psi(t)$, as shown in Equation 4.28.

$$\chi^V(e_T) = \psi_s^v + \arctan(-\frac{e_T}{\Delta}) \tag{4.25}$$

$$\begin{aligned} \lim_{t\to\infty} e_T &= 0 \\ \lim_{t\to\infty} \psi_s^v &= 0 \end{aligned} \tag{4.26}$$

$$\begin{aligned} \chi^V(e_T) \quad &= \psi_s^v + \arctan(-K_p \cdot e_T \\ &\quad + K_i \cdot \textstyle\int_0^t -e_T(t)dt + K_d \frac{d(-e_T(t))}{dt}) \end{aligned} \tag{4.27}$$

$$\psi_d = \chi^V(e_T) + \psi(t) \tag{4.28}$$

The sonar configuration and desired standoff distance are used to determine the parameters in Equation 4.27. Figure 4.21 shows the forward propagated distance for the scanning sonar (± 17.5 degrees) moving parallel to a straight wall that is configured to be 35 degrees forward looking as introduced in Chapter 2. The standoff distance of 40 meters is selected because the averaged forward propagated distance exceeds 20 meters which is the minimal turning radius of the vehicle. Therefore the sonar foresees the obstacles beyond vehicle's turning radius to alert the potential collision.

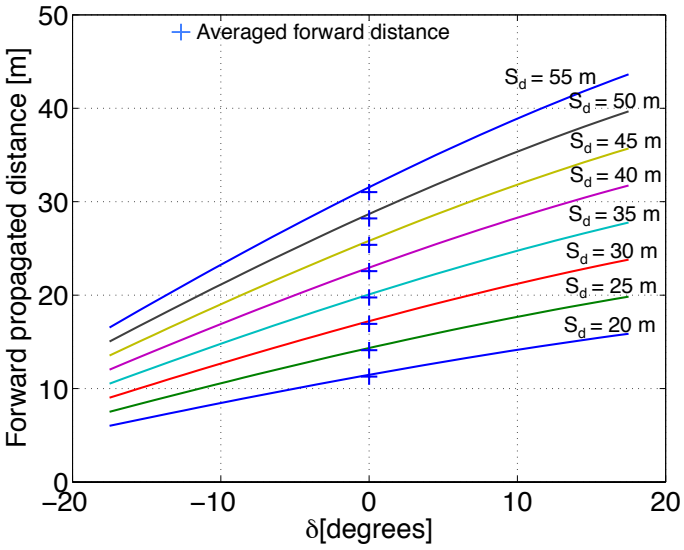


Figure 4.21: Forward-looking distance of the rays at different desired standoff distance

$$\Delta = S_d \cdot \sin(\beta + \max(\delta)) \tag{4.29}$$

The maximum forward-looking distance for a desired standoff distance ($S_d$) can be calculated in Equation 4.29. At a standoff distance of 40 meters, the forward-looking distance in LOS (Equation 4.25) is computed at about 30 meters from Equation 4.29. Thus, $K_p$ in Equation 4.27 is equals to 1/30. Several attempts were conducted in the simulation environment to tune other parameters in the Equation 4.27. The $K_d$ is tuned to 0.5 for a minimized overshot in tracking the desired path. $K_i$ is set to zero since a non-zero value was found to have a destabilizing effect that can result in a significant influence on the overshoot that causes the potential collision with the iceberg.

### 4.3.4 GNC Evaluation on a regular shape object

The designed GNC was initially evaluated in a simulation environment shown in Figure 4.22. The sonar and the iceberg modeled in Chapter 3 are implemented in

MATLAB, while the Slocum glider is simulated in a hardware simulator, a real-time glider simulator with emulated sensor output, i.e. attitude measurements and depth measurements. The designed GNC is implemented on a single board computer (SBC) in $C^{++}$. The communication between the platforms are implemented via a serial communication line.

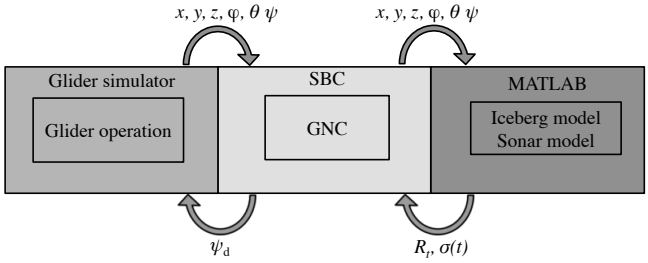


Figure 4.22: Simulation environment setup for evaluating the GNC

The profiling simulation is executed on the underwater portion of an iceberg with a constant square (200 m x 200 m) cross-section as shown in Figure 4.23. The glider is programmed to operate using a thruster at a speed about 0.5 m/s, and to maintain a target depth of 20 meters within a depth-tolerance of $\pm$ 1.5 meters. The results of the simulation are shown in Figure 4.23. The glider (red-line) successfully circum-navigated the target in about 45 minutes with the desired heading $\psi_d$ computed by the GNC shown in black arrows. Figure 4.23 also shows the ideal path in blue that is obtained by expanding the target (blue region) outward by a standoff distance of 40 meters. All valid sonar measured ranges, $R_t$, are directly converted into the NED coordinate system and shown in the green points under the assumption that the sound is coming from the central ray. The surface reconstruction is applied to the resulting point cloud using the method introduced in the Appendix A.2.

Demonstrating GNC performance, Figure 4.24 shows the distance from the vehicle to the ideal path, the blue path in Figure 4.23, together with the corresponding vehicle heading during the mission. Overshoots are observed in Figure 4.24 when the

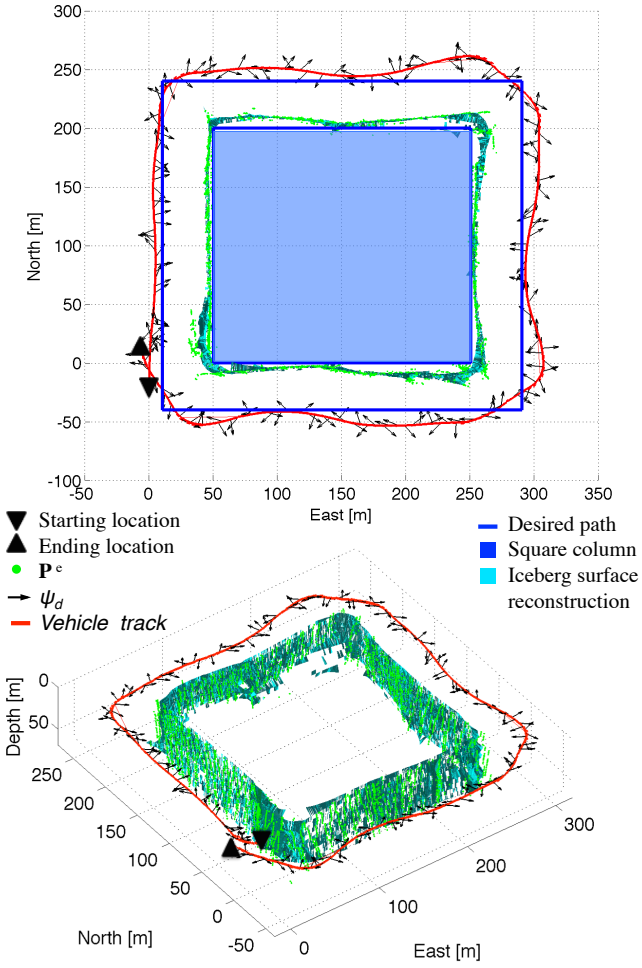


Figure 4.23: Autonomously map the artificial underwater cloumn with the proposed GNC. Top: top view of the result; bottom: perspective view of the resulting surface reconstruction.

vehicle is turning at iceberg corners leading to a sharp increase in vehicle heading. The downward-pointing arrows and upward-pointing arrows show the start and end of the turning motion at iceberg corners. The overshoots maybe due to the slow yaw dynamics of the vehicle. A RMS of 9.33 meters is found between the vehicle trajectory and the ideal path. The non-zero RMS value may because of the lack of the integral gain $K_i$, resulting in a steady-state error. Moreover, the generated desired path from the VOM is tilted towards the vehicle caused by the arc shape from the

inverse-sonar model with a forward-looking angle. As shown in Figure 4.19, the profile of the occupied cells is relative straight, but an arc shape is formed at $x_t^v$ equals to and larger than 20 m in the VOM. Therefore, the slope of the resulting path will become smaller when applying the polynomial regression on the occupied cells, and the computed desired heading will be smaller than the actual terrain profile because the cross-track error is reduced due to the decreased slope.

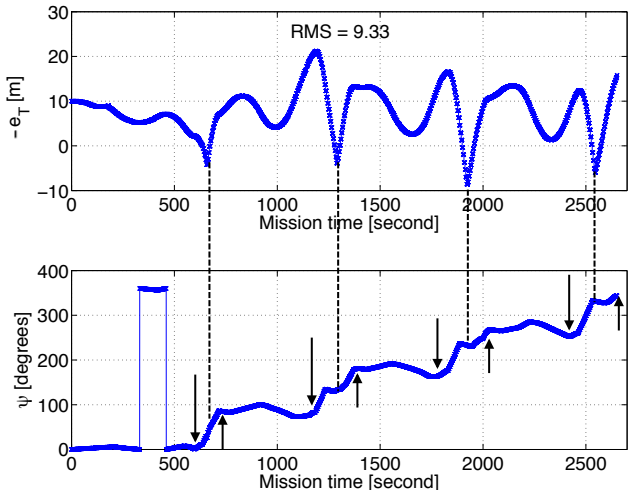


Figure 4.24: The top plot shows track error from the vehicle to the ideal path, the bottom plot shows the vehicle heading during the mission.

As mentioned in the introduction of the GNC, the received sound may come from the side rays other than the central ray. Therefore, errors will appear between the sonar measured profile and the actual shape of the target. Such errors are clearly shown in Figure 4.23 when mapping the corners of the target. For a vertically uniform object, e.g. the simulated vertical column, the measured cross-sectional profile obtained with the GOM introduced previously can be used to construct the 3D shape. The GOM obtained using the sonar ranges with the dynamic inverse-sonar model in the simulation is shown in the left plot in Figure 4.25. Meanwhile, the right plot in Figure 4.25 shows good agreements between the estimates trend of the terrain from the VOM and the actual trend of the terrain.

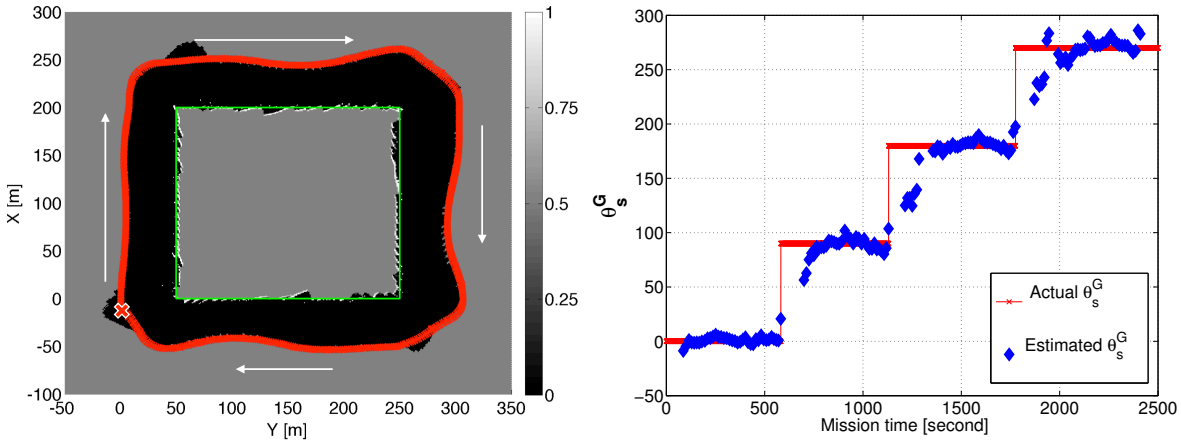


Figure 4.25: Left: Global occupancy map (GOM) generated using the dynamic inverse-sonar model. Red-line is the trajectory of the vehicle, and green-line is the actual shape of the column. Right: the slope of the terrain estimated from the VOM compared with the actual values.

We further evaluated the advantages of using the GOM updated from the dynamic inverse-sonar model. This GOM is compared to a GOM updated from the static inverse-sonar model where only $P_{DI}(\delta)$ is included in Equation 4.19, and also compared to a resulting point cloud with the general sonar model where the sonar is only simulated with the central ray. In GOMs, the cross-sectional profile is obtained by selecting the cells with $P(M^G_{x^G_t,y^G_t}|R_1,...,R_t) > 0.5$, while the cross-sectional profile is obtained by directly convert $R_t$ into NED coordinate system in general sonar model. Because this is a two-dimensional profile, only the sonar sample within the effective sector of $[-5, 5]$ is included for map updating. The cross-sectional profiles of the object obtained from different inverse-sonar models are compared in Figure 4.26. A high ratio of overlap between the profiles from the dynamic and static inverse-sonar model is detected. The mapping performance from the three sonar models is compared in terms of coverage and root-mean-square (RMS) between the observed profiles and the actual profile. Shown in Figure 4.27, the histogram summarizes the numbers of samples in angular sectors (10 degrees) around the center of the square column. The

averaged numbers from different angular sectors are indicated in dash-line across the plots. As shown in Figure 4.27, the target profile in GOM updated from the dynamic inverse-sonar model has the highest coverage on the target.

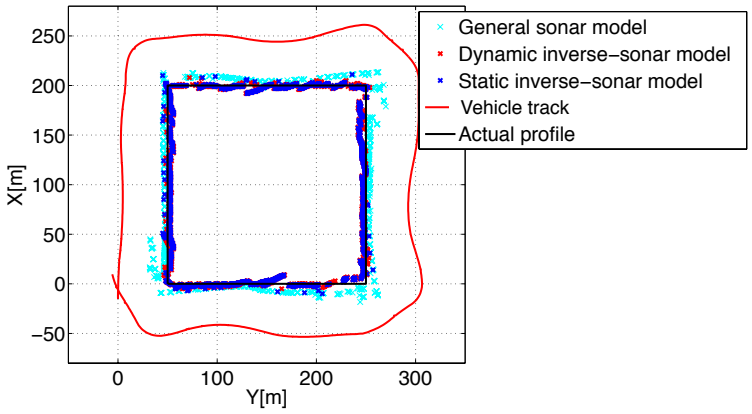


Figure 4.26: Resulting cross-sectional profiles from different sonar models when the vehicle is traveling around the column.

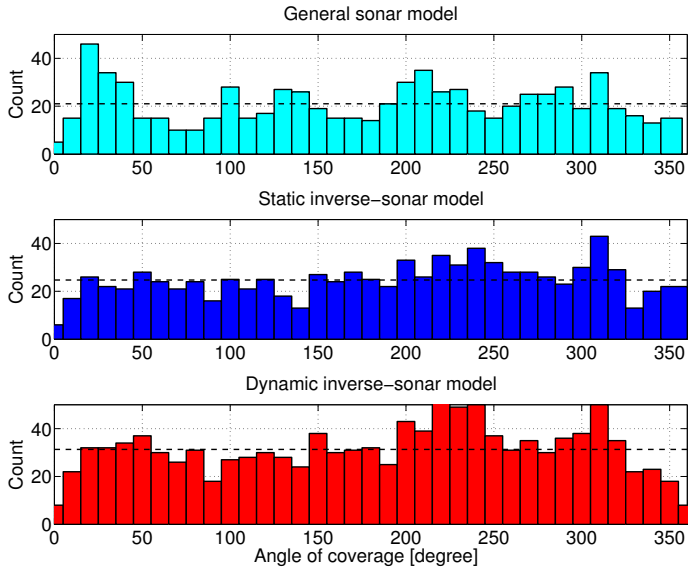


Figure 4.27: Comparison of the angle of coverage with three inverse-sonar models, the horizontal hidden line shows the averaged number of samples in the angle sectors

In the next step, we compared the resulting target profiles from GOMs with different thresholds on the $P(M^G_{x^G_t,y^G_t}|R_1,...,R_t)$ in selecting occupied cells. The root-mean-

square (RMS) error of the distance from the samples on the resulting profiles to the actual target is then calculated. Figure 4.28 shows the comparison of the RMS error and numbers of samples from different inverse-sonar model at various threshold on the probability of occupancy. The result from the general sonar model is not affected by such change in the threshold because it is not generated based on the inverse-sonar model. In contrast, the profiles obtained from GOMs have lower numbers of data points at a higher value of the probability threshold. Meanwhile, the error RMS decreases for an increased threshold. Overall, the profile extracted from the GOMs updated from the dynamic inverse-sonar model has the lowest error RMS and highest data points for a better representation of the original target.

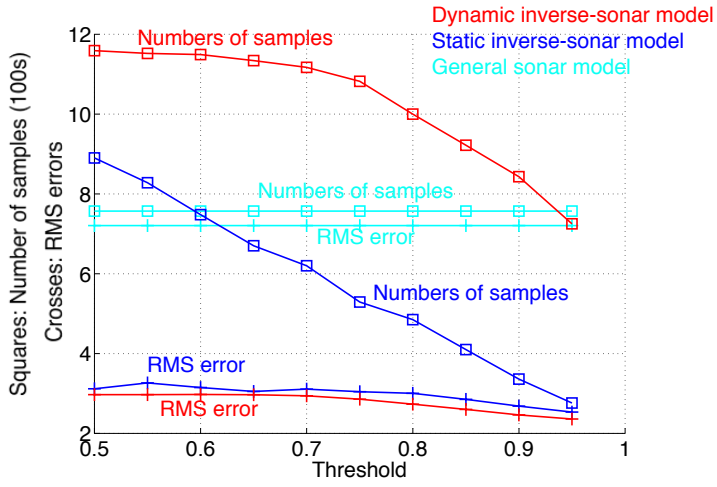


Figure 4.28: Comparison of RMS error and number of samples from different sonar model at various threshold on the probabilities.

The comparison of $P_o(\delta, R_t)$ in dynamic inverse-sonar model and static sonar model is shown in Figure 4.29 where the $\theta_s^v$ is zero so that the vehicle is moving parallel to the terrain. The dynamic inverse-sonar model yields a higher probability of occupancy at higher ray angle which is close to the y-axis of the vehicle. Figure 4.29 shows sonar samples at the same scanning-angle in the four consecutive scans on an object. The general sonar model may produce shorter range measurements because the rays

at higher ray angles collide with the object prior the center rays. Considering the fan-shape sound propagation, the ray fronts from the previous sample at smaller ray angles are overlapped by the empty region in the newer samples. As a result, only the cells ensonified by the rays at higher ray angles will remain when updating the GOM. As shown in Figure 4.29, higher values are assigned on the higher ray angles in the dynamic inverse-sonar model. Thus, the occupied cells in the GOM updated using the dynamic inverse-sonar model will have a larger number of cells at the same threshold in the probability of occupancy.

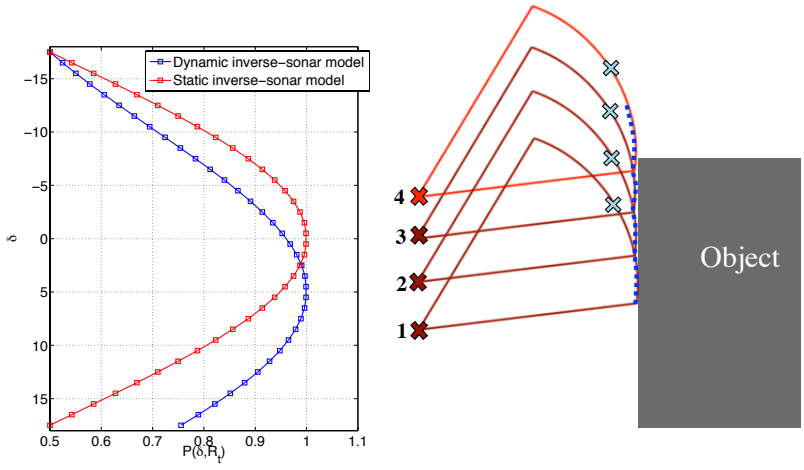


Figure 4.29: Sonar pings in the four consecutive scans at the same scanning anle

In mapping the object with varying cross-sectional profiles, the introduced GOM can be expanded into a three-dimensional mesh grid that is not limited to display the two-dimensional environment at the vehicle's traveling plane. Currently, the 3D GOM is not implemented for environment reconstruction, however, it is considered for future work. Similar research has being done in [109] where an OctoMap is constructed using measurements from laser range finder.

### 4.3.5 GNC Evaluation on modeled iceberg

After the evaluation of the GNC on a regular shape target, a simulation is conducted with the designed GNC on a modeled floating iceberg. The iceberg is assumed moving with a northward velocity of 0.05 m/s (0.18 km/hour) and a rotational velocity of 0.025 degrees/s (90 degrees/hour). The rolling, pitching, and heaving motion are assumed to be negligible. The configuration of the sonar, the glider, and the GNC are identical to the previous simulation.

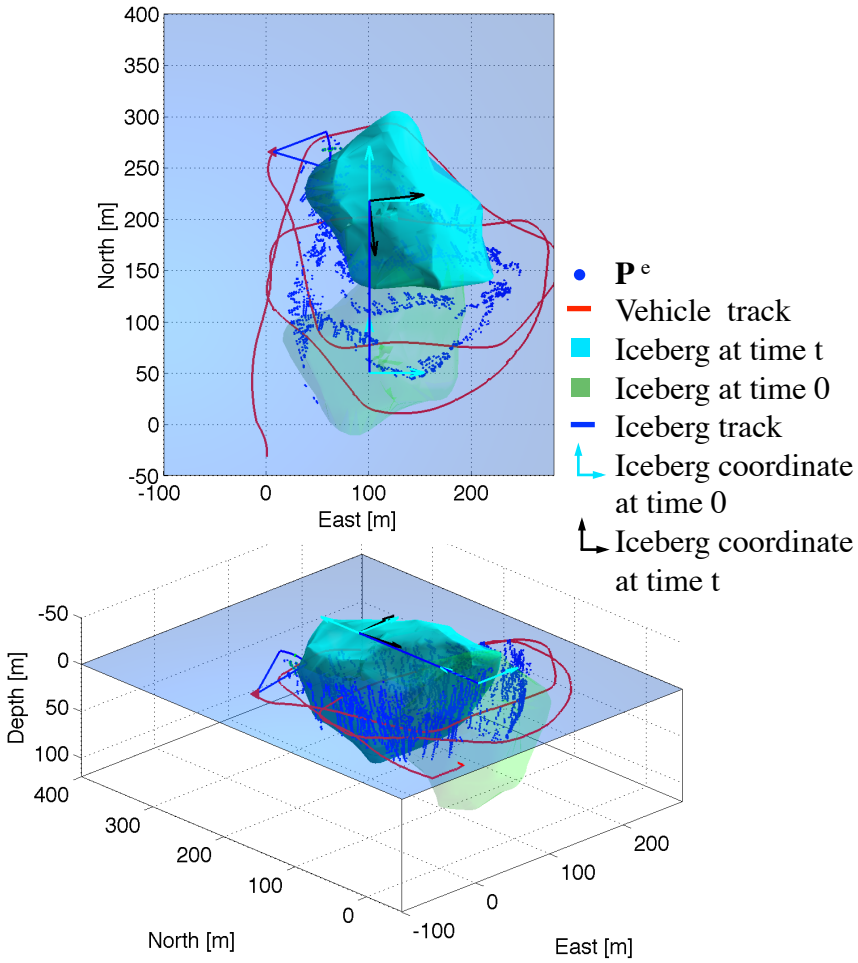


Figure 4.30: Overview of the simulated iceberg mapping operation.

Figure 4.30 shows the top view and perspective view of the results from the simulation. The glider traveled around the iceberg two times in about an hour with the trajectory

shown in red. The glider was traveling horizontally at a nominal depth of 20 meters at a speed about 0.6 m/s. As a result the iceberg profile at a depth from zero to 60 meters (about 50% of the overall volume of the target iceberg) is obtained. In Figure 4.30, the sonar detected iceberg surface is displayed in the blue dots. The initial and final iceberg pose are shown in green and cyan rendering with a blue line indicating the path of the coordinate system attached to the iceberg during the mission. To reconstruct the iceberg surface from the point cloud, the iceberg motion which is usually unknown is needed. An algorithm for estimating the iceberg motion in three degrees of freedoms will be introduced in Chapter 5.

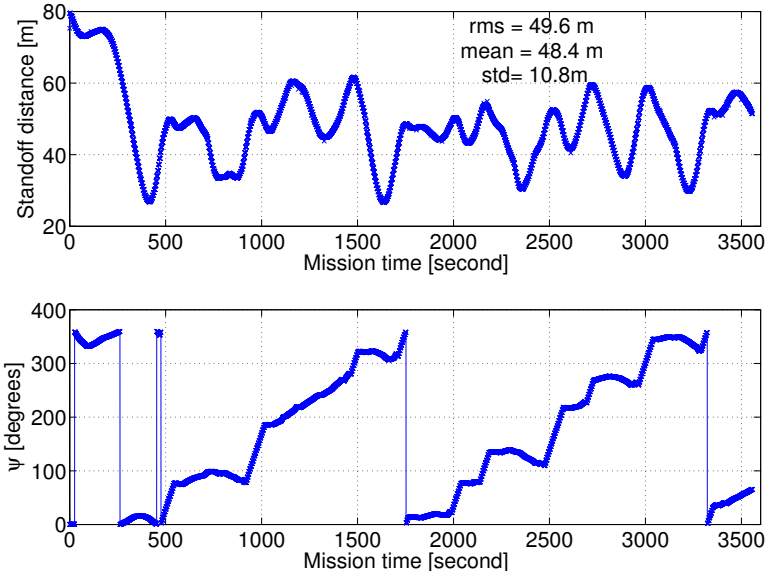


Figure 4.31: Standoff distance from the vehicle to the iceberg

To evaluate the performance of the GNC in controlling the vehicle, the distance from the vehicle to the cross-sectional profile of the iceberg at the depth of 20 meters is calculated and shown in Figure 4.31. The resulting standoff distance has a root-mean-square (RMS) of 49.6 meters, a mean value of 48.4 meters and a standard deviation of 10.8 meters. The reasons causing such offset in RMS and mean value from the desired standoff distance (40 meters) are discussed in the previous section. The lack of an

integral portion of the controller as well as slow vehicle dynamics might be the cause for these errors. Compared to the vehicle performance on a regular stationary target, the overshoots observed in this operation are larger. Therefore, the integral gain $K_i$ that may have a destabilizing effect potentially causing a collision onto the iceberg is still excluded from the GNC. Furthermore, the speed of the sound in the sonars is assumed to be 1500 m/s. However, the speed of the sound is observed smaller than 1500 m/s from the field measurements on the conductivity-temperature-depth sensor. As a result, the sonar measured ranges are actually smaller due to the overestimation in the speed of the sound. Therefore, the offset in the performance value comparing to the desired standoff distance may be compensated by the reduced speed of the sound.

### 4.3.6 GNC Evaluation in the field

In June 2016, the iceberg-profiling Slocum glider with the designed GNC was deployed to survey an iceberg in Twillingate, Newfoundland, Canada. The geographic location of Twillingate make it famous for iceberg sighting. The target iceberg is grounded on the seafloor at the entrance of Browneys Cove. The glider with the designed GNC was deployed on different days to detect the iceberg shape changes and to observe the iceberg movements.

The above water profiles captured at four locations around the target iceberg in different dates are shown in Figure 4.32. A long extension on the southern side of the iceberg is observed in the images captured on June 12. Compared to the images from later days, the above water shape has changed significantly. Based on the mission log, the weather was rainy with on-shore winds on June 13 and June 14. Because of high sea-state (2-3m) the field trials were paused on June 13 and June 14. This severe weather may have caused the iceberg to roll, and shorten the southern extension.

Similar features are found from the images captured on June 15 and June 16 that the highlighted groove across the eastern face is closer towards the water on June 16, and the portion on the western face is lifted above the water.

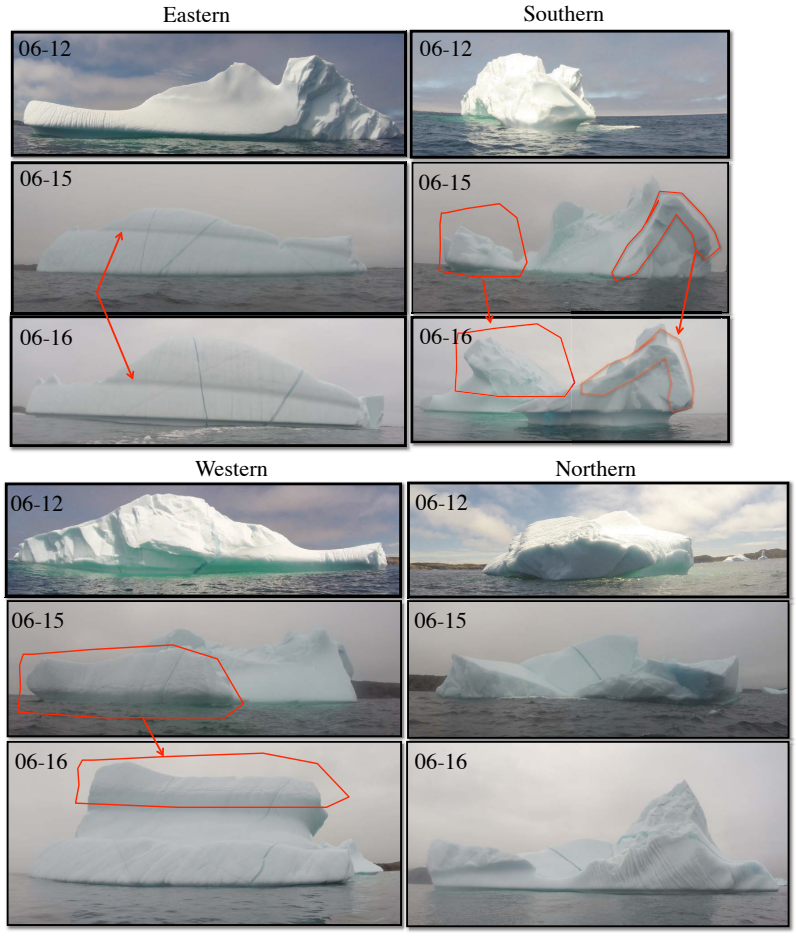


Figure 4.32: Images captured in different dates from four directions on the target icebergs

During the iceberg survey, the glider was programmed to travel horizontally at the desired depth of 25 meters with the integrated thruster. The depth error tolerance for the horizontal flight is ±2.5 meters before the buoyancy engine is engaged for a major depth correction (see Chapter 2 for more details). The glider is requested to surface when the vehicle has not communicated with the control center for 20 minutes. The sonar is configured identically to the simulation that it continuously scans a sector

within the ±45 degrees off the horizontal plane on the starboard side of the glider with a forward-looking angle of 35 degrees. The active depth ($z_e$) is configured at 10 meters, while the effective sector is $[-5, 5]$ degrees. The p-gain ($K_p$) and d-gain ($K_d$) are 1/30 and 0.5 in computing the desired heading in the LOS guidance law.

In summary, the GNC successfully guided the glider traveling around the iceberg in the four deployments conducted on three days (June 12, June 15 and June 16). In the post-processing, the underwater location of the glider is first corrected using the estimated speed in level-flight model from Chapter 2. After that, we assume the sonar measured range is coming from the central ray. The measured ranges are corrected for the averaged sound-speed derived from the measurements collected by the CTD sensor on the glider. Then, the measurements of the iceberg are converted into a point cloud in a georeference coordinate system, i.e. the latitude-longitude-depth and Universal Transverse Mercator (UTM) coordinate system.

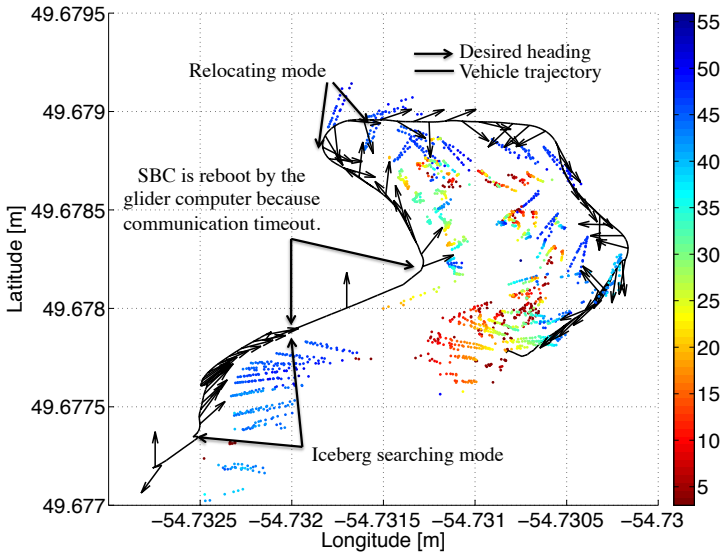


Figure 4.33: Top view of the results obtained on June 12. The colorbar indicates the depths of the detected iceberg surface.

Figure 4.33 shows the results obtained on June 12. The glider was deployed from the southwest of the iceberg. After the glider submerged under the depth of 10 meters

(the active depth), the GNC was activated and initialized in the iceberg-searching mode. As indicated in Figure 4.33, the glider was controlled to approach the iceberg with heading increasing continuously. The SBC was found to have been rebooted at 5 minutes after the mission started. The reboot was triggered by the glider computer due to a communication timeout because of an error byte or a byte drop that halts the communication between the SBC and glider or the sonar. The system becomes functional again after about 2 minutes. Once, the SBC became functional again, consistent iceberg surface was detected, the GNC mode was shifted from iceberg-searching mode into the profile-following mode to avoid the collision and to follow the western profile of the iceberg. After a while, the iceberg disappeared from the view of the sonar at a sudden profile change at the northern tip where the GNC changed the mode to control the glider in relocating mode to regain the iceberg surfaces. The glider successfully traveled around the iceberg while sectional profile are mapped with the sonar. Since the iceberg was grounded, the seafloor returns are also detected and shown in darker scatters (dark blue).

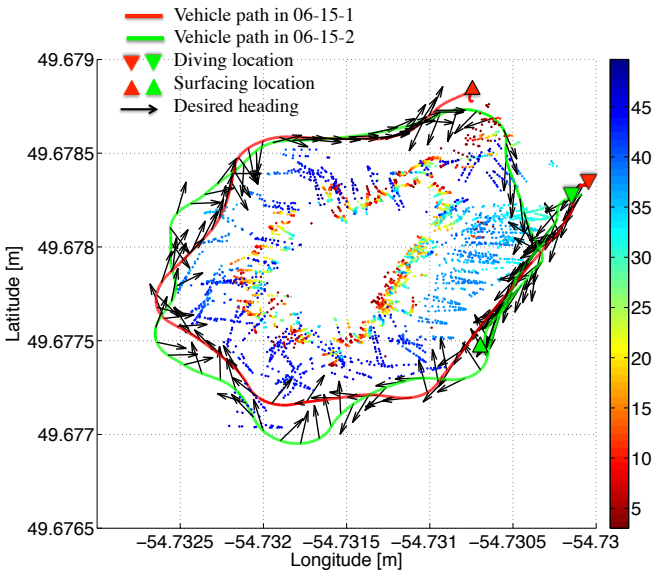


Figure 4.34: Top view of the results obtained on June 15. The colorbar indicates the depths of the detected iceberg surface.

On June 15, two deployments were conducted on the same iceberg. The glider was deployed from the northeast corner of the iceberg. Figure 4.34 shows the overall results from the two deployments. The overlap between the two resulting point clouds collected from separated deployments validates the method of correcting the glider's underwater location discussed in Chapter 2. The resulting point cloud on June 15 is different from the point cloud shown in Figure 4.33 revealing the significant rotation or shape changes on the iceberg.

On June 16, the glider was deployed from an approximate location as on June 15. The glider successfully circumnavigated around the iceberg using the presented GNC. As a result, a point cloud showing the iceberg shape is obtained from the sonar measured ranges. Comparing the point clouds collected from different dates, very similar shapes can be observed between Figure 4.34 and Figure 4.35.

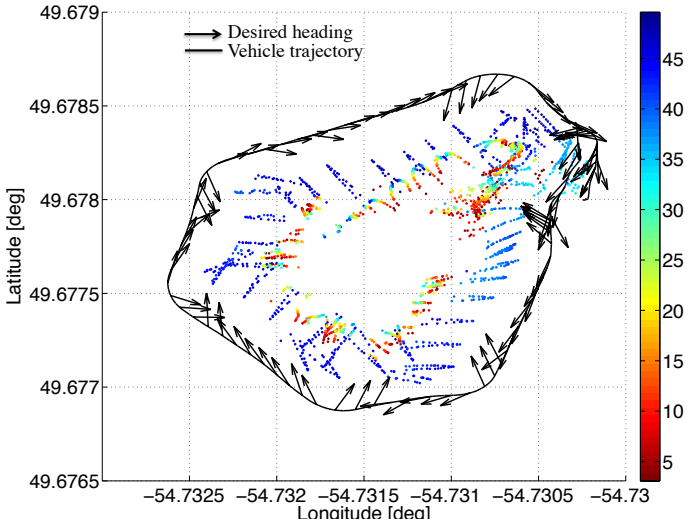


Figure 4.35: Top view of the results obtained on June 16. The colorbar indicates the depths of the detected iceberg surface.

The point clouds from different deployments presented in a Local Mission Coordinates are shown in Figure 4.36 in various colors. The shown points are limited up to depth of 30 meters to exclude the seafloor detection. No significant correlation is

observed between the point cloud obtained on June 12 and the shape measured in other deployments because a portion of the iceberg on the west was not profiled due to the malfunction of the SBC on June 12. Comparing the point clouds obtained on June 15 and June 16, the results show a similarity in geometry, but a location shift towards the south with a small counter-clockwise rotation.

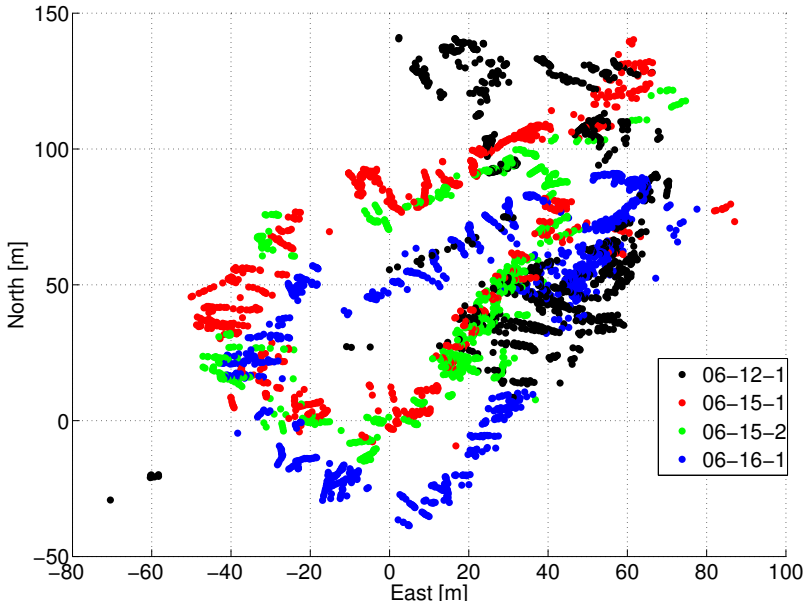


Figure 4.36: Point clouds from separated deployments shown in a local mission coordinates.

The point clouds obtained on June 15 and June 16 are further processed to reconstruct the iceberg surface and shown in Figure 4.37. In Figure 4.37, the red surface shows the iceberg reconstruction using the point clouds collected in two operations conducted on June 15, while the blue surface is generated based on the single mission accomplished on June 16. The points for reconstruction is limited up to depth of 30 meters, while the deeper points are treated as seafloor returns showing in dots in Figure 4.37. The trajectories of the vehicle from the three deployments are shown in red, green and black. The weight of the volume enclosed by the two iceberg surface are calculated to be similar, but a slightly increase is observed on June 16. The mass is calculated

by integrating the cross-sectional areas over its depth span (2.5 meters).

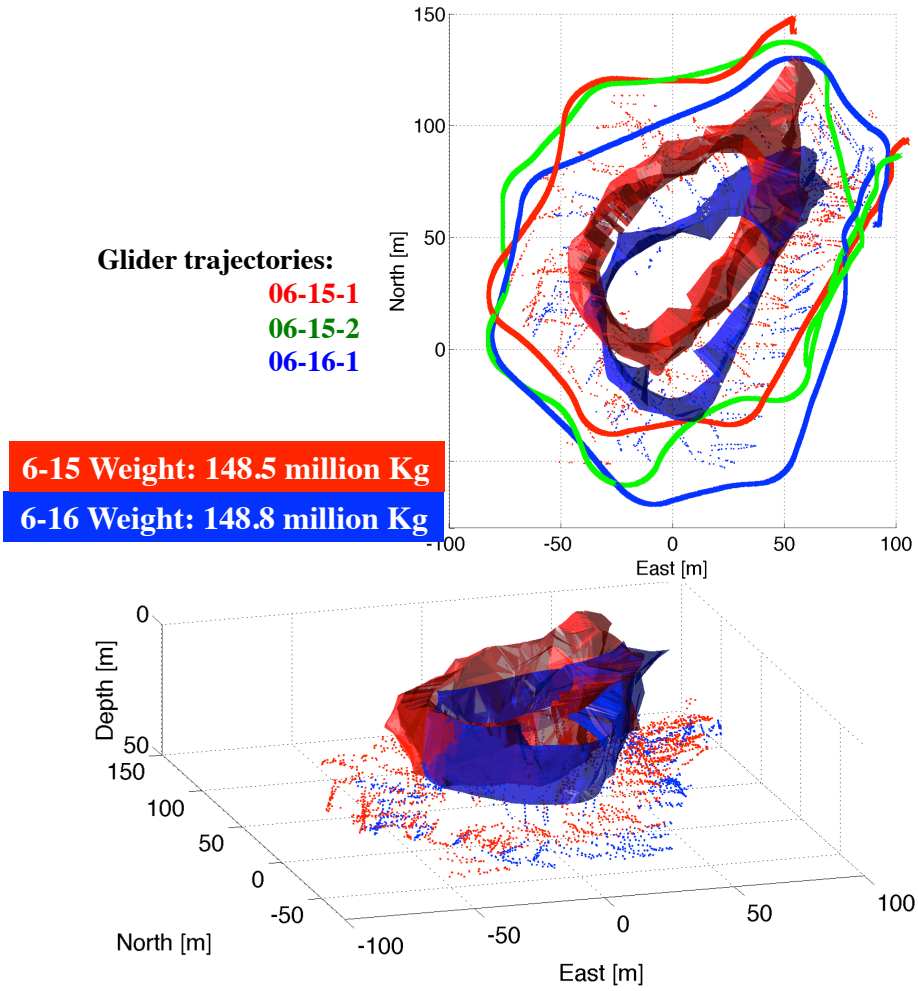


Figure 4.37: Iceberg surface reconstruction from the data collected on June 15 and June 16. The shape is registered in Local Mission coordinate system with origin located at a known longitude-latitude.

The small increment in the weight may because of the rotation of the iceberg where a rolling towards the east is found from the above water images. But the difference in the weight estimate is about 1% which is well within the measurement error. Possible reason for changing the profiles, shapes and volumes may due to the iceberg tilting. The change of environment, e.g. tide level, may be another factor causing an increase in the underwater portion. Since the iceberg was grounded, the water-

line on the iceberg may have increased on June 16 leading an increased underwater portion. Another factor causing an increased underwater shape is the change of the water density. During the circumnavigation, the conductivity and temperature were measured with a Sea-Bird Conductivity-Temperature-Depth (CTD) sensor installed on the mid-section of the glider. The water density is then calculated from the CTD measurements using the algorithm in [110]. Figure 4.38 shows the resulting water density versus depth measured during the missions in two days. The water density is found larger on June 15 than June 16. Therefore, the iceberg may sit lower in the water if any room is available between the iceberg and the seafloor. Overall, above water and below water measurements have to be conducted simultaneously in order to obtain the overall change in volume.

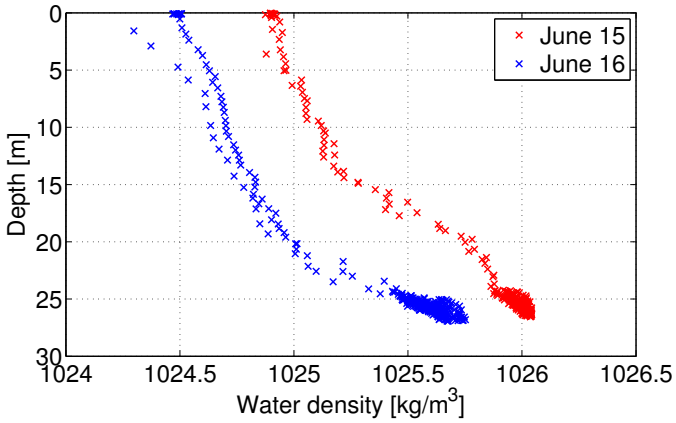


Figure 4.38: Water density at depth calculated from the CTD measurements

Regarding the performance of the GNC, the cross-track errors ($e_T$) in the LOS guidance law is shown in Figure 4.39. The objective of the LOG guidance law is to minimize the cross-track error to zero. As shown in Figure 4.39, the Root-Mean-Square and the mean value of $e_T$ are negative, meaning the vehicle is further away from the target than desired. However, overshoots are observed in the three deployments where $e_T$ increased upto 20 meters. As a recommendation in the future work, the gains in

the LOS will be tuned to minimize the overshoots and steady-state errors.

Figure 4.40 shows the standoff distance between the vehicle's trajectories to the iceberg surface shown in Figure 4.37. Compared to the desired standoff distance, the Root-Mean-Square Error (RMSE) of the standoff distance is about 8 meters for the three missions. As shown in Figure 4.40, The standoff distance has a minimum value at about 1000 seconds. Similar performance is also observed in Figure 4.39.

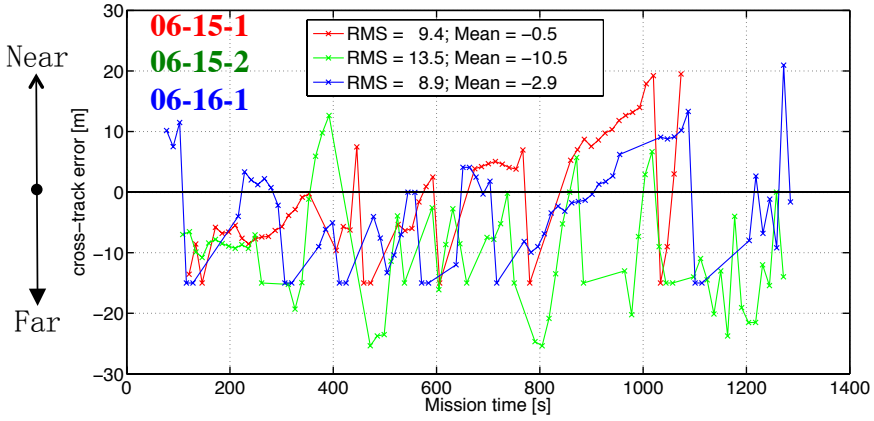


Figure 4.39: Cross-track errors during the three deployments

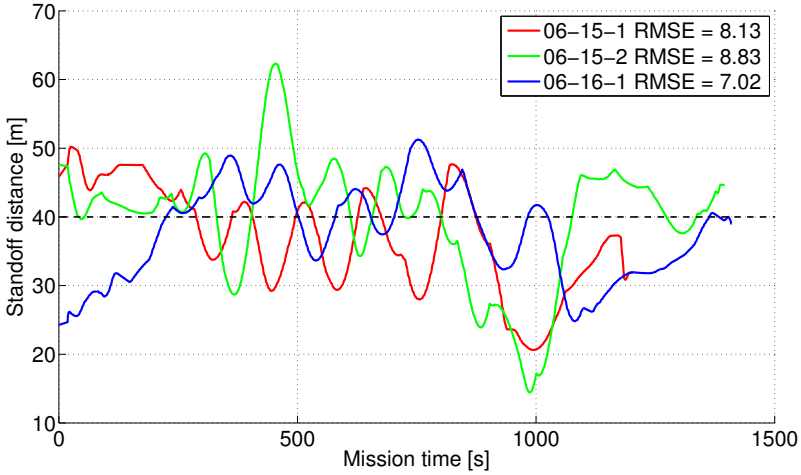


Figure 4.40: Resulting standoff distance from the reconstructed iceberg surface during the three deployments

In summary, multiple assessments were conducted on the target iceberg with the

modified Slocum glider. The autonomous iceberg profiling is successfully implemented on the Slocum glider with the designed GNC. However, fine tuning on the guidance law is required in order to minimize the overshoot and errors in the standoff distance and cross-track errors.

# Chapter 5

# Iceberg motion estimation

In this Chapter, an algorithm for estimating the iceberg motion is introduced. Before the development of the algorithm, several assumptions are stated.

- The roll, pitch and heave motion of the iceberg are constrained because they are small compared to the other motions. Therefore, the iceberg motion is limited to three degrees-of-freedom (DOF), northward velocity ($u_i$), eastward velocity ($v_i$), and a rotational velocity ($r_i$) around the z-axis of the iceberg-centered coordinate system. The rolling, pitching, and heaving happen due to the nonuniform deterioration causing a shift of the center of mass. Obeying the iceberg stability theory [43] and [92], a pitching, a rolling or a heaving will occur to realign the center of gravity (CG) and center of buoyancy (CB) vertically. These types of motion typically happen every several hours. From the field trial result in Chapter 4, the Slocum glider circumnavigated around an iceberg in about 25 minutes. Therefore, the AUV-based underwater iceberg profiling will complete in a significantly shorter period before the occurrence of CB and CG realignment.

- The iceberg-attached coordinate system is assumed to be located at the centroid

of the cross-sectional profile at calm water sea-level. For the initial state (time = 0), the x-axis of the coordinate points north while y-axis of the coordinate points east. The z-axis of the coordinate points downward.

- The velocities of the iceberg are assumed to be constant during the iceberg survey. As introduced in [3], the iceberg motion is a result from multiple environmental sources including wind, ocean current, surface waves, and tide. These factors slowly change over long periods (hours). Therefore the assumption of constant iceberg velocities over one or two hours is reasonable.

In the following section, the algorithm developed based on the point cloud registration will be introduced to estimate the motion of iceberg. The proposed algorithm is validated with simulated iceberg profiling data and real world multi-beam sonar data collected circumnavigating around a floating iceberg.

## 5.1 Point cloud registration based motion estimation

Due to the iceberg motion, the location and the orientation of the iceberg coordinate system is changing between time 0 to time t as shown in Figure 5.1. With the assumed constant velocities $u_i$, $v_i$, and $r_i$, the iceberg changes in location and orientation are expressed in Equation 5.1 and 5.2. In underwater iceberg-profiling, the sonar produced range measurements are first converted into point locations relative to the vehicle. Then using the orientation and location of the vehicle, these point locations are converted into points an the inertial coordinate system, e.g. $X^e - Y^e$ as shown in Figure 5.1. Figure 5.1 shows the same point on the iceberg as measured by the sonar at time = 0 and time = t. In the iceberg-attached coordinate, $\mathbf{P}_0^i$ and $\mathbf{P}_t^i$ represent the

same location, however they are appear differently in the inertial coordinate system since $\mathbf{P}_0^e$ is not aligned with $\mathbf{P}_t^e$. Therefore, the point cloud based on $X^e - Y^e$ is needed to be convert into the iceberg-attached frame to represent the actual iceberg shape. The conversion is conducted using the information about iceberg motion between time 0 and t. For example, $\mathbf{P}_t^e$ is converted into $\mathbf{P}_t^i$ in Equation 5.3 and 5.4. Once all the points are based on the iceberg-attached coordinate system, then the iceberg reconstruction method mentioned in Appendix A.2 can be performed.

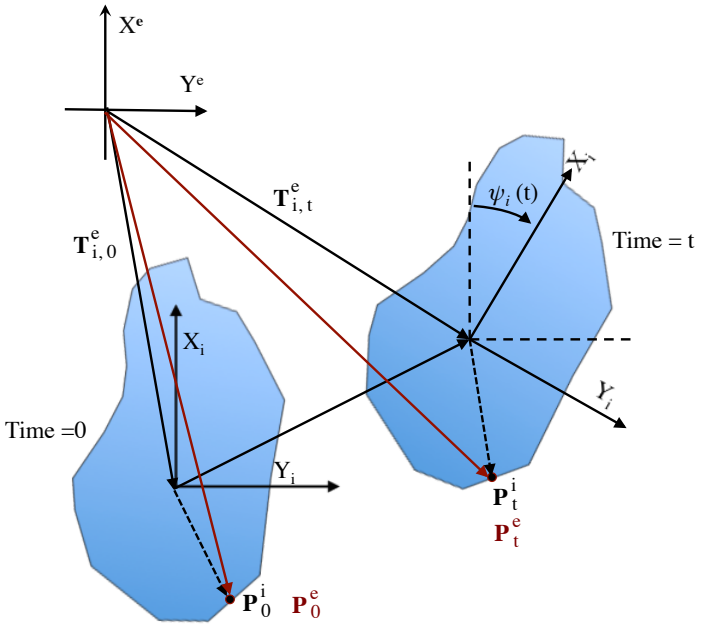


Figure 5.1: Iceberg moved and rotated from time 0 to time t causing a point on the iceberg is shifted from $\mathbf{P}_0^e$ to $\mathbf{P}_t^e$.

Assuming a region on the iceberg is measured by the sonar between time $t = j$ to $t = k$ and from time $t = p$ to $t = q$, two groups of points are indicated by $\mathbf{P}^e_{j:k}$ and $\mathbf{P}^e_{p:q}$ in the inertial coordinate system. After converted into the iceberg-attached frame, $\mathbf{P}^i_{j:k}$ and $\mathbf{P}^i_{p:q}$ should coincide if the correct information about the iceberg motion are used in converting the points using Equation 5.3 and 5.4. Otherwise, the information about the iceberg motion is required to be adjusted, or the assumption that $\mathbf{P}^i_{j:k}$ and

$\mathbf{P}^i_{p:q}$ are the same region on the iceberg is invalid.

$$\mathbf{T}^e_{i,t} = \mathbf{T}^e_{i,0} + \int_0^t \begin{bmatrix} u_i \\ v_i \\ 0 \end{bmatrix} dt = \mathbf{T}^e_{i,0} + \begin{bmatrix} u_i \cdot t \\ v_i \cdot t \\ 0 \end{bmatrix} \tag{5.1}$$

$$\psi_i(t) = \psi_i(0) + \int_0^t r_i dt = \psi_i(0) + r_t \cdot t \tag{5.2}$$

$$\mathbf{P}^i_t = \mathbf{R}^{i,t}_e(\mathbf{P}^e_t - (\mathbf{T}^e_{i,t} - \mathbf{T}^e_{i,0})) \tag{5.3}$$

$$\mathbf{R}^{i,t}_e = \begin{bmatrix} \cos(\psi_i(t)) & \sin(\psi_i(t)) & 0 \\ -\sin(\psi_i(t)) & \cos(\psi_i(t)) & 0 \\ 0 & 0 & 1 \end{bmatrix} \tag{5.4}$$

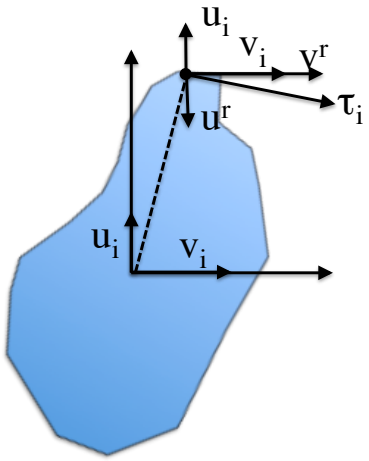


Figure 5.2: Additional translation motion induced by the rotation around the vertical axis of the iceberg-attached frame

Based on the above statement, an algorithm for estimating the iceberg motion using point clouds is developed. The overall algorithm consists of four parts with the flowchart shown in Figure 5.3. During the initialization, two points clouds, $\mathbf{P}^e_{j:k}$ and

$\mathbf{P}^e_{p:q}$, are selected. Invalid sonar measurements where the $R_t$ equals to the maximum profiling range, $R_s$, are excluded. The numbers of valid sonar measurements in $\mathbf{P}^e_{j:k}$ and $\mathbf{P}^e_{p:q}$ are preferred to be equal or close. The iceberg is initially assumed stationary with $u_i$, $v_i$ and $r_i$ at zero. As shown in Figure 5.2, the rotation induces a tangential velocity of a point on the iceberg. In order to avoid the interference between the iceberg motion in rotation and translation, the translation and rotation are estimated in the separate iteration process.

During the iteration operations, $\mathbf{P}^e_{j:k}$ and $\mathbf{P}^e_{p:q}$ are first converted to $\mathbf{P}^i_{j:k}$ and $\mathbf{P}^i_{p:q}$ using Equation 5.3. Then the Iterative Closest Point (ICP) algorithm [72] is applied to the two iceberg-related point clouds to estimate the transformation matrice which links $\mathbf{P}^i_{j:k}$ and $\mathbf{P}^i_{p:q}$ in Equation 5.5. The ICP algorithm is one of the most popular algorithms used in point cloud registration. There have been several modifications to the first ICP in [72], such as the generalized ICP [76].

$$\mathbf{P}^i_{p:q} = \mathbf{R}_{icp} \cdot \mathbf{P}^i_{j:k} + \mathbf{T}_{icp} \tag{5.5}$$

$$u_i := u_i + K_p \frac{\mathbf{T}_{icp,(1,1)}}{(p+q-j-k)/2} \tag{5.6}$$

$$v_i := v_i + K_p \frac{\mathbf{T}_{icp,(2,1)}}{(p+q-j-k)/2} \tag{5.7}$$

$$r_i := r_i + K_p \frac{\arcsin(\mathbf{R}_{icp,(1,2)})}{(p+q-j-k)/2} \tag{5.8}$$

Because these point clouds are presumed to be identical initially, the translation velocities are updated if the ICP yields a nonzero $\mathbf{T}_{icp}$ in updating translation estimates. To satisfy the objective such that the elements in $\mathbf{T}_{icp}$ is approaching zero, the

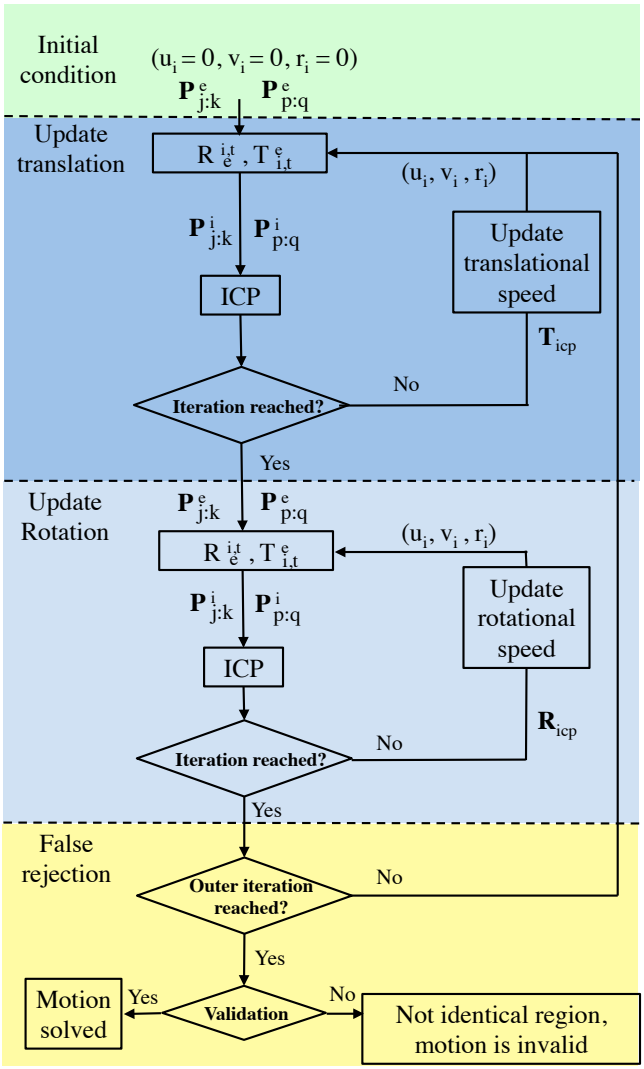


Figure 5.3: Flowchart of iceberg motion estimator

northing velocity ($u_i$) and easting velocity ($v_i$) are updated using Equation 5.6 and Equation 5.7. After the iterations on updating the translation, the rotation velocity is iteratively updated using Equation 5.8. The object is that $\mathbf{R}_{icp,(1,2)}$ is approaching zero. In Equation 5.6 to 5.8, $K_p$ is a variable used to control the rate of convergent and to reduce the overshoot in the estimates during the iteration. The denominator in the equations are the average time differences between the two point clouds. An outer iteration is included using the updated rotational velocity to re-estimate the

translational velocity because the change in rotational velocity may affect the $\mathbf{T}_{icp}$ leading an additional adjustment in estimating translational velocity. The number of the outer iterations is usually less than 5 and internal iteration in updating the translational and rotational velocity is usually less than 50.

The introduced motion updating process only uses two-dimensional point clouds. As a consequence, profiles at the corners of the iceberg may be similar leading to a false estimates in the algorithm. Therefore, a validation process is designed to reject the false estimates. Presuming the motion estimation is valid, the following points sampled after the two chosen point clouds, $\mathbf{P}^i_{m:n}$ and $\mathbf{P}^i_{r:s}$, should be overlapped after converted into the iceberg-attached coordinate system using the estimated iceberg motion. As a result from applying ICP on the two new point clouds $\mathbf{P}^i_{m:n}$ and $\mathbf{P}^i_{r:s}$, $\mathbf{R}_{icp}$ and $\mathbf{T}_{icp}$ should satisfy the objectives stated in Equation 5.10 to 5.11.

$$\mathbf{P}^i_{r:s} = \mathbf{R}_{icp} \cdot \mathbf{P}^i_{m:n} + \mathbf{T}_{icp} \tag{5.9}$$

$$\mathbf{R}_{icp} \approx \begin{bmatrix} 1 & 0 & 0 \\ 0 & 1 & 0 \\ 0 & 0 & 1 \end{bmatrix} \tag{5.10}$$

$$\mathbf{T}_{icp} \approx \begin{bmatrix} 0 & 0 & 0 \end{bmatrix}^T \tag{5.11}$$

## 5.2 Validation with simulation dataset

In Chapter 3, an iceberg profiling simulator was constructed. This simulation environment is used to create data for validating the iceberg motion estimation algorithm. In the simulation, a level-flight Slocum underwater glider equipped with a mechanical

scanning sonar is modeled moving a constant surge speed of 0.5 m/s. The profile-following control algorithm introduced in Chapter 4 is implemented to control the vehicle to keep a constant standoff distance away from the iceberg. Meanwhile, a translation and a rotation vectors is applied on the iceberg model to mimic a continuous and steady iceberg motion.

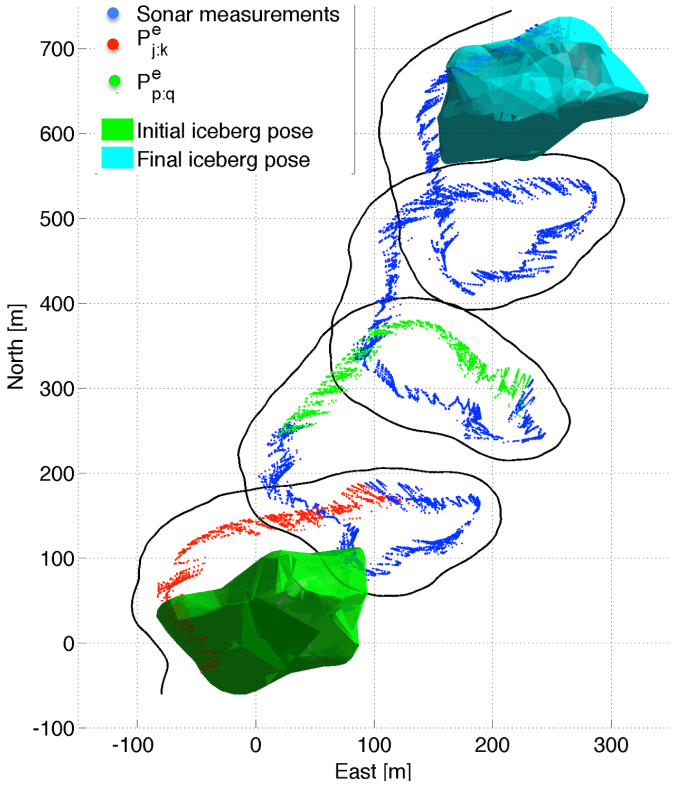


Figure 5.4: Iceberg measurements during the circumnavigation based on the inertial coordinate. The data is obtained from the simulated environment.

A dataset from the simulator is shown in Figure 5.4 where a simulated level-flight Slocum glider is surveying a translating and rotating iceberg with a mechanical scanning sonar continuously scans the vertical swath on the starboard side of the vehicle. The green and cyan rendering show the initial and final position of the iceberg. The iceberg was translating at a speed of $u_i = 0.094$ m/s and $v_i = 0.0342$ m/s, and was rotating clockwise at a rate of $r_i = 0.025$ degree/s. The blue point cloud shown in

Figure 5.4 shows the overall sonar measured iceberg surfaces during the mission. The red and green point clouds measured at the different periods present the same region on the iceberg but shifted due to the iceberg motion.

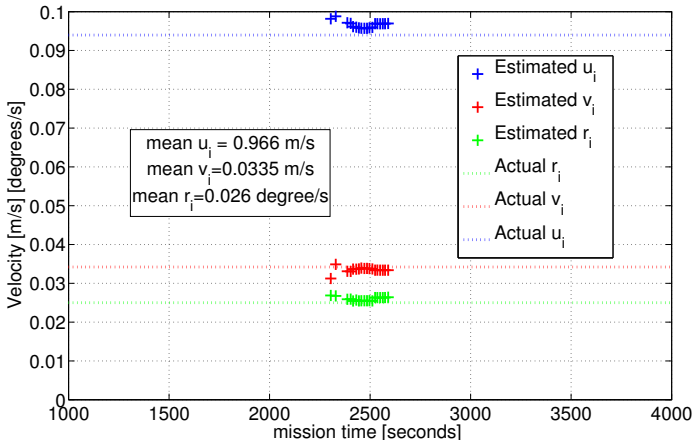


Figure 5.5: Valid estimated iceberg motion on the point cloud shown in Figure 5.4.

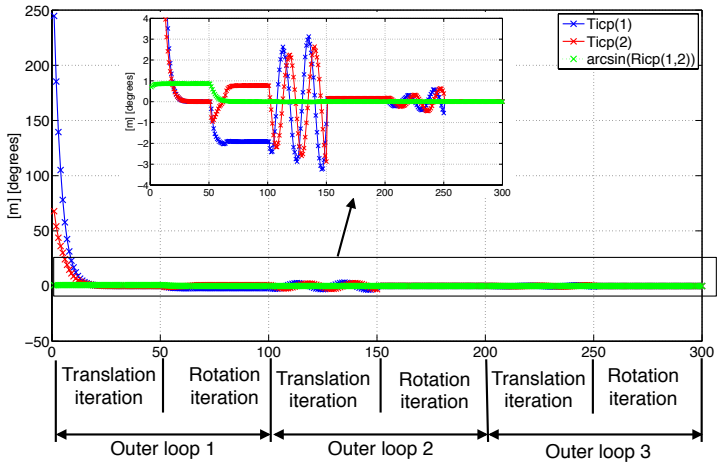


Figure 5.6: Results by applying ICP on $\mathbf{P}^{i}_{j:k}$ and $\mathbf{P}_{p:q}$ at incremental iterations.

The algorithm for estimating the iceberg motion is applied to the blue point cloud. The first 3000 valid sonar samples are indicated in red in Figure 5.4 are chosen as $\mathbf{P}^{e}_{j:k}$, while $\mathbf{P}^{e}_{p:q}$ is a segment of blue point cloud. The iceberg motion is estimated whenever 50 new valid sonar measurements are obtained after time $k$, and the oldest 50 valid sonar measurements in $\mathbf{P}^{e}_{p:q}$ is eliminated in order to keep a similar data volume.

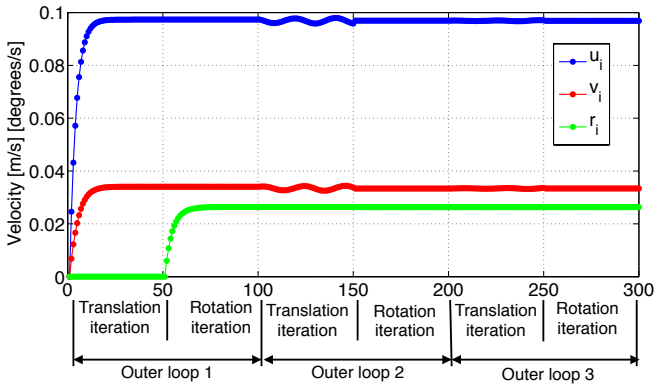


Figure 5.7: Estimated velocities, $u_i$, $v_i$, and $r_i$ at incremental iterations based on the data from the simulation.

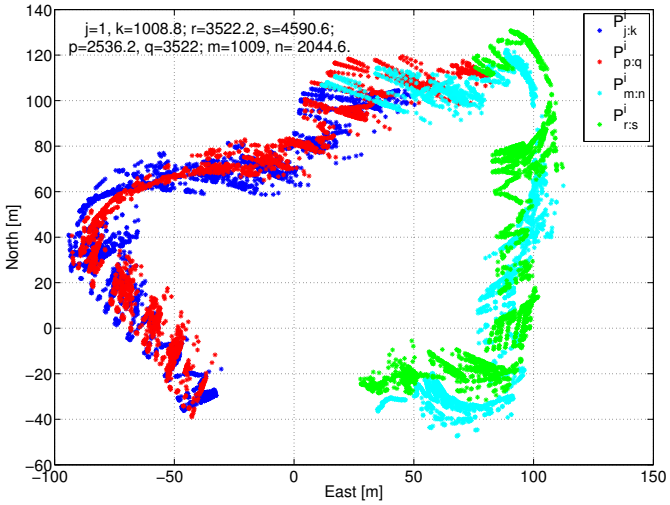


Figure 5.8: $\mathbf{P}^i_{j:k}$, $\mathbf{P}^i_{p:q}$, $\mathbf{P}^i_{m:n}$ and $\mathbf{P}^i_{r:s}$ obtained using the estimated iceberg motion based on the data from the simulation.

Figure 5.5 shows the result from the motion estimation. The motion solution for this simulation is found after about 2500 seconds of mission time. Figure 5.6 shows the results from the ICP during the iteration after 2536 seconds. For the same time, 5.7 shows the estimated iceberg motion at incremental iterations The numbers of outer iteration and internal iteration are 3 and 50 respectively. The elements in $\mathbf{T}_{icp}$ and $\sin^{-1}(\mathbf{R}_{icp}(1,2)$ are approaching zero (see objectives stated in Equation 5.10 and 5.11) during the iteration meaning the overlap between two point clouds are

likely. Meanwhile, the estimated motion converges. A small oscillation in translation estimates is observed at the beginning of the second outer loop to compensate the small shift in translation induced by the updated rotation motion.

Figure 5.8 shows resulting point cloud $\mathbf{P}^i_{j:k}$ and $\mathbf{P}^i_{p:q}$ at time 2536 using the results from the motion estimation. $\mathbf{P}^i_{m:n}$ and $\mathbf{P}^i_{r:s}$ shows the validation that future points cloud of $\mathbf{P}^i_{j:k}$ and $\mathbf{P}^i_{p:q}$ are overlapped indicating a valid estimation.

## 5.3 Validation with a field trial dataset

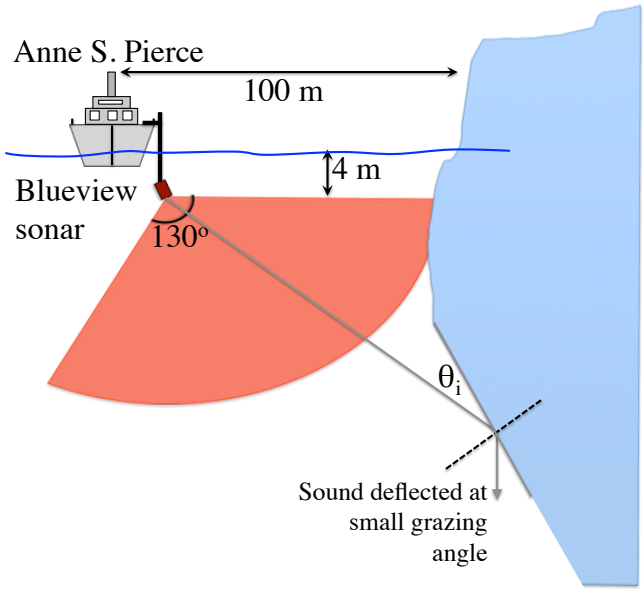


Figure 5.9: Sketch of Blueview multi-beam sonar setup on the MV Anne S. Pierce

In July 2015, the Blueview multi-beam sonar (M450-130) was side-mounted on a Marine Vessel, MV Anne S. Pierce, to profile a floating iceberg (Figure 5.9). The sonar was submerged to a depth of 4 meters, and it was oriented to align its 130 degrees of field-of-view vertically. The sonar is further rotated such that one of the edges of the field-of-view to be horizontal. The sampling of the sonar is controlled by the Proviewer Software [111] provided by the manufacturer. The sonar samples

are logged with the information of longitude, latitude, Coordinated Universal Time (UTC) and course over ground from an external GPS module. The support vessel circumnavigated in counter-clockwise direction around the iceberg three times at a nominal speed about 3 m/s maintaining a distance of about 100 meters away from the iceberg. The profiling range of the sonar was set to 150 meters at which range the sonar is pinging at 2 Hz.

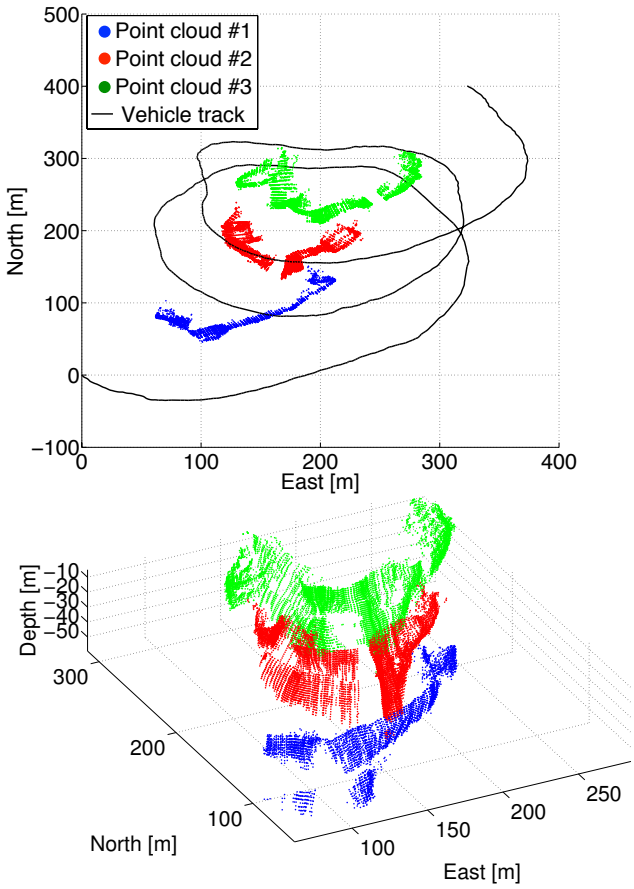


Figure 5.10: Sonar measurements collected using the Blueview sonar, and the ship's trajectory is shown in black. The measurements are presented in the North-East-Down coordinate with origin at the initial location of the ship.

Using the software development kit (SDK) provided by the manufacturer, the samples in the logged files are processed into ranges as introduced in Chapter 2. The ranges are further converted into points in a NED coordinate with origin attached to the

initial location of the vessel when the survey started (see Appendix A.1 for the transformation). In post-processing, the rolling and pitching of the support vessel were not considered due to lack of attitude measurements, and are assumed to be zero for the processing of the range measurements. Moreover, the heading of the vehicle was assumed to coincide with the course-over-ground measured from the GPS. The heave motion of the vessel was not measured during the mission. The missing measurements will cause some errors in the resulting point cloud shown in Figure 5.10. Different colors are assigned to the samples from various revolutions. Figure 5.10 shows only sectional profiles. The reason for the lack of coverage maybe due to the high slope of the vertical profile on the northern side of the iceberg. As shown in Figure 5.9, the acoustic energy is deflected away from the surface instead of reflected back to the sonar at a small incident angle ($\theta_i$).

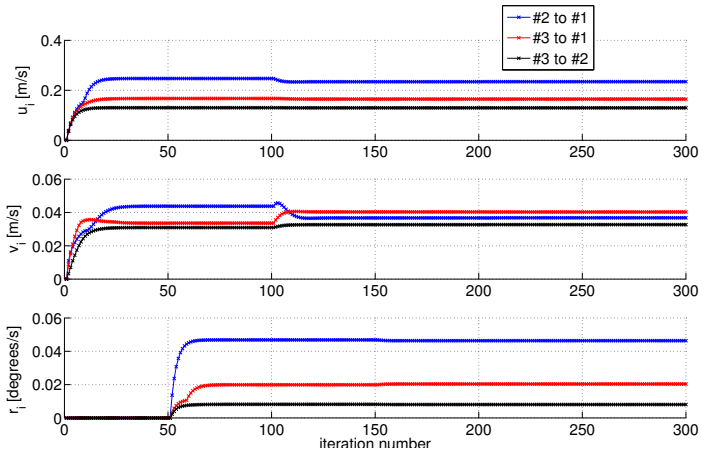


Figure 5.11: The estimated iceberg motion at incremental iterations

The algorithm for estimating the iceberg motion is applied to the three point clouds. To decrease the processing time in ICP the size of the point cloud is reduced to about 60% of the original size that only the points between depth of zero to 20 meters are selected when estimating the iceberg motion. The outer iteration and the internal iteration is assign to 3 and 50 respectively resulting in a total number of iterations of

300. Figure 5.11 shows the velocity estimates at individual iterations, and Figure 5.12 shows the resulting transformation from the ICP when applied to the compared point clouds. From the estimates it can be observed, the iceberg has a higher translation and rotation motion from the first revolution to the second revolution which agrees with Figure 5.10 where the blue point cloud and red point cloud are further apart.

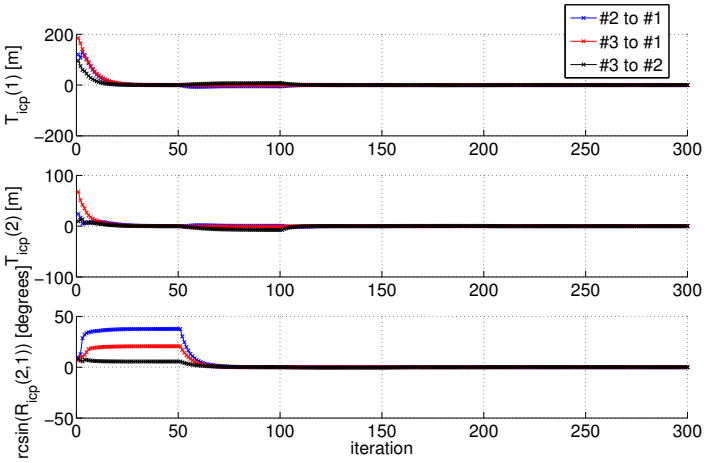


Figure 5.12: The resulting transformation from applying ICP to the point clouds corrected to the estimated iceberg motion.

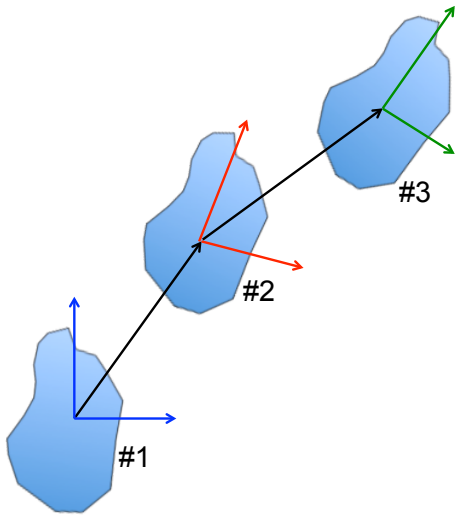


Figure 5.13: Evolution of the iceberg-attached coordinate at three different time

For an iceberg with an inconsistent motion, as shown in Figure 5.13, the location and

orientation of the iceberg-attached coordinate, $X_i(t) - Y_i(t) - Z_i(t)$, at time #3 can be derived from #1 by integrating the velocities over time. Since we have estimated the averaged iceberg motion from three different point clouds, the estimates are valid if Equation 5.12 is satisfied. The time $t_1$, $t_2$, and $t_3$ denote the averaged time in the three point clouds, and subscripts in the iceberg motion denote the source of point clouds used in estimating the iceberg. Using the converged values from Figure 5.11, Equation 5.12 becomes Equation 5.13. The difference between the left-hand side and the right-hand side in Equation 5.13 may cause by the ICP that although the $\mathbf{R}_{icp}$ is approximately an identity matrix and $\mathbf{T}_{icp}$ is approaching zero (see Figure 5.12), the two point clouds may not be fully overlapped due to the outliers in the samples. More importantly, the rolling, pitching and heave motion of the ship were not considered which induce uncertainty in the point clouds.

$$\begin{bmatrix} u_{3,1} \\ v_{3,1} \\ w_{3,1} \end{bmatrix} \cdot (t_3 - t_1) \approx \begin{bmatrix} u_{2,1} \\ v_{2,1} \\ r_{2,1} \end{bmatrix} \cdot (t_2 - t_1) + \begin{bmatrix} u_{3,2} \\ v_{3,2} \\ r_{3,2} \end{bmatrix} \cdot (t_3 - t_2) \tag{5.12}$$

$$\begin{bmatrix} 229.35 \\ 56.02 \\ 28.31 \end{bmatrix} \approx \begin{bmatrix} 171.02 \\ 26.84 \\ 33.78 \end{bmatrix} + \begin{bmatrix} 85.86 \\ 21.61 \\ 5.30 \end{bmatrix} = \begin{bmatrix} 256.88 \\ 48.45 \\ 39.08 \end{bmatrix} \tag{5.13}$$

Figure 5.14 shows the point clouds converted into the iceberg-attached frame using the estimated averaged iceberg motion. The small misalignment could be caused by the assumption of constant iceberg motion, and the lack of roll, pitch and heave information for the surface vessel. Figure 5.15 shows the result in reconstructing the iceberg surface using the points in Figure 5.14. The iceberg is reconstructed using the method introduced in Appendix A.2 that the points are separated into cross-sectional profiles at incremental depth (colored contours in Figure 5.15). Then Alpha shape

[93] is applied to remodel the iceberg surfaces.

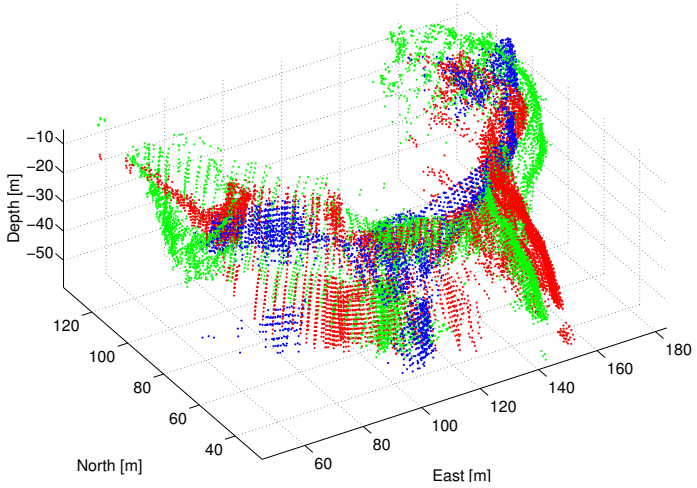


Figure 5.14: Three point clouds in Figure 5.10 are merged with the estimated iceberg motion.

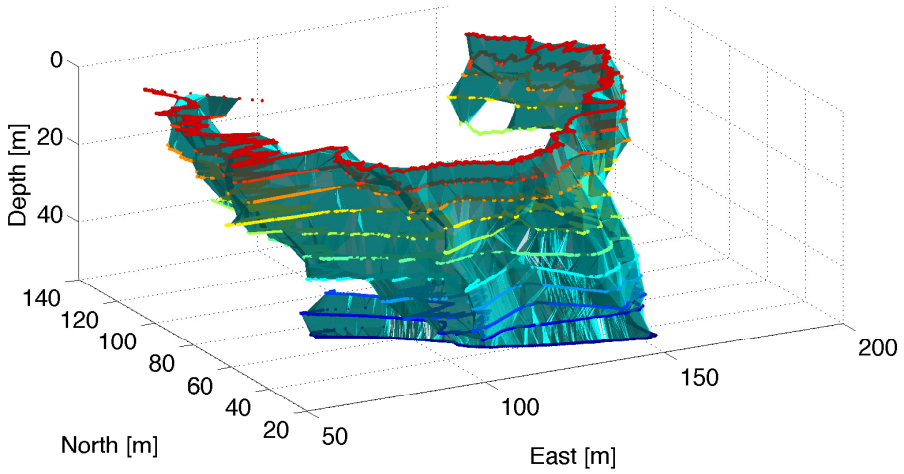


Figure 5.15: Iceberg reconstruction with Alpha shape algorithm, the color contours are the cross-sectional profiles.

During the field trial, I found the planar velocity of the iceberg is not constant since the distance between the blue point cloud and the red point cloud is larger than the distance between the red point cloud and the green point cloud. As a result from applying the estimation algorithm on these point clouds, the change in iceberg motion is detected. However, this result is an averaged iceberg motion during each

revolution. Additional measurements are required for estimate an accelerating iceberg motion. One approach is to equip the AUV with a Doppler Velocity Log that measures the speed of iceberg surface relative to the vehicle [59].

# Chapter 6

# Conclusion and future work

## 6.1 Summary of the work

In this thesis, we have presented an application using an AUV for underwater iceberg mapping. Compared to the conventional method in which a vertical sonar-based profiler from a ship, the AUV operation is safer, more convenient and cost-effective. The selected AUV, a Slocum glider, has an endurance up to months that allows continuously tracking and mapping of a floating iceberg without the need for a support vessel.

Applying a simulation analysis in Chapter 3, we have compared the performance of the proposed AUV-based mapping method with the ship-based iceberg-profiler. The operations from both platforms are simulated for three icebergs with the same modeled mechanical scanning sonar. I show that the AUV yields lower errors and more consistent performance in estimating the overall shape of the underwater portion than those from the vertical probe. Although the performance of the profiling probe can be improved using a sonar with a longer range and deploying it more frequently, the cost and time of the operation will be increased proportionally. The AUV based operation

takes longer to perform an iceberg profiling operation than the conventional method, but the time can be reduced by increasing the speed of the vehicle which is assumed to be 0.5 m/s in the simulation. One benefit of the AUV-based iceberg mapping is that there is a high ratio of overlap in sonar measurements between consecutive revolutions. During the analysis, the number of revolutions is reduced by half without significantly increasing the resulting error. The AUV can obtain the underwater shape of a medium size iceberg in two hours and map a large iceberg in 4 hours. The averaged errors in estimating the actual shape are about 15% for overall volume. Overall, the AUV-based method is found to be more accurate and less expensive than for conventional operation. In summary, this thesis demonstrated a novel and low-cost solution for mapping the underwater portions of icebergs. The simulation tool that we developed could also be used for analysing other aspects of the iceberg surveying, e.g. exploring the influence of iceberg motion on the result.

The AUV-based iceberg-profiling is challenging due to the navigation and autonomy control using on-board sensors. While previous work has been done in [59] to [62] to improve iceberg-related AUV navigation, this work focuses on the development of sonar-based autonomous control for iceberg surveys. A guidance, navigation, and control (GNC) system is developed for the AUV in Chapter 4 to map the iceberg autonomously. From the results, both the simulations and the field trials, the designed GNC can successfully guide the vehicle around the iceberg at a desired stand-off distance without collision. Due to limitations in physical constraints and power consumption, a mechanical scanning sonar is integrated to sense the range from the vehicle to the iceberg for controlling the vehicle and iceberg mapping. This sonar is configured to scan a sector on the starboard side of the vehicle $\pm$45degrees off the horizontal plane. It is further rotated to have a forward-looking angle of 35 degrees for avoiding any protrusion feature of the iceberg. A vehicle-attached occupancy map

(VOM) is implemented in the GNC that presents the environment around the vehicle, revealing the obstacles detected by the sonar. The VOM is updated using a dynamic inverse-sonar model once a sonar range is collected. The dynamic inverse-sonar model is modified from a general inverse-sonar model used for range-finders on a mobile robot. The novelty of this modification is to account for the influence from the incident angle when the simulated rays intersect the terrain. The probabilities of occupancy in the inverse-sonar model are adapted for the change of the terrain. Compared with a static inverse-sonar model, that assumes the central ray always has the highest probability of occupancy, the dynamic inverse-sonar model yields more occupied cells in the occupancy map, and presents the actual environment at smaller errors (see Section 4.3.4 in Chapter 4). The GNC is first characterized in a simulation environment. Then, it is implemented on the Slocum glider and evaluated in the field. The GNC successfully guided the vehicle circumnavigating around a target icebrg four times on different dates. As a result, the underwater shape of the target iceberg is obtained with shape and location changes observed from the measurements collected on different dates.

When reconstructing the iceberg shape, knowledge of the iceberg movement is essential. The resulting point cloud collected from the sonar has to be converted into a coordinate system relative to the iceberg. In Chapter 5, an algorithm is designed to estimate the iceberg motion by registering the two separated point clouds sampled in different periods. The algorithm is applied to data sets collected from simulation and in the field. As a result, the estimated iceberg motion agrees with the assumed iceberg motion of the simulation. The point cloud collected in the field is corrected using the estimated iceberg motion. Then the iceberg shape is reconstructed with the resulting point cloud in the iceberg-attached coordinate system. The algorithm is not limited to AUV-based iceberg survey but could also apply to the samples collected from a

side-looking sonar on a surface vessel that is used for a quick iceberg assessment near an offshore platform.

## 6.2 Future work

In the future, the GNC will be further improved. Currently, an initial heading is required in the mission script so that the glider will not collide with the iceberg. As an improvement, the initial heading could be computed automatically from the above water measurements that can be provided from an Unmanned Surface Vessel (USV). The communication between the two unmanned platforms will be implemented so the initial heading can be obtained on the USV and then transmitted to the AUV. Moreover, the navigation of the AUV can be further improved by better characterizing the thruster, this yielding a better dead-reckoning model. Since an underwater modem is also available on our AUV, its underwater location can be resolved from the surface unit. The resolved locations will then be transmitted from the surface to the AUV for a geo-referenced location update. Based on our experience localizing the AUV with the underwater modem, the underwater modem alone is not sufficient to generate a smooth and consistent trajectory of the AUV due to the noise in the ocean. Therefore, the acoustic method and the dead-reckoning method will be combined for the best localization result.

The algorithm for estimating the iceberg motion will be further implemented on the GNC. When the algorithm generates a valid motion estimate, the two point clouds used in the algorithm overlap. In other word, the vehicle is back at its original position relative to the iceberg. If multiple revolutions at different depth are required for a deep-keel iceberg, this loop-closure detection can be implemented to notify the vehicle to adapt its depth for mapping deeper portion. In iceberg reconstruction,

a three-dimensional global occupancy map (GOM) will be implemented. Currently, the point cloud for iceberg reconstruction are converted from the sonar ranges Such an assumption will induce uncertainty in determining the true shape of the target. The three-dimensional GOM will compensate for such uncertainty by assigning a probability of occupancy to the elements in three-dimensional mesh gridded map.

Regarding the operational scenario discussed in Section 1.5 in Chapter 1, this thesis addressed the problem of vehicle control and reconstructing a floating iceberg shape. A future study should be conducted for path planning of the AUV approaching an iceberg from a further distance using periodic iceberg location updates.

# Bibliography


[1] C-Core and B. Wright and Associates Ltd., *An Assessment of Current Iceberg Management Capabilities*, PERD/CHC Report 20-33, November, 1998.

[2] AMEC Earth & Environmental, R.F. McKenna & Associates, and PETRA International Ltd., *Grand Banks Iceberg Management*, PERD/CHC Report 20-84, May 2007.

[3] S. Smith and N. Donaldson, *Dynamic Modelling of Iceberg Drift using Current Profiles*, Candian Technical Report of Hydrography and Ocean Sciences No. 91, 1987.

[4] G. Hodgson, J. Lever, C. Woodworth-Lynas, and C. Lewis, *Dynamics of Iceberg Grounding and Scouring Volume 1 - The Field Experiment*, Environmental Studies Research Funds, 1998.

[5] Autonomous Undersea Vehicle Application Center, *www.auvac.org*.

[6] C. Bishop, B. deYoung, and R. Bachmayer, *Autonomous Underwater Glider Research at Memorial University*, Jounral of Ocean Technology, NO. 1, Vol. 4, 2009.

[7] D. L. Rudnick, R. E. Davis, C. C. Eriksen, D. M. Fratantoni, and M. J. Perry, *Underwater Gliders for Ocean Research*, Journal of Marine Technology Society, Vol 38, 2004.

[8] D. Thompson, D. Caress, H. Thomas, and D. Conlin, *MBARI Mapping AUV Operations in the Gulf of California 2015*, OCEANS 2015 - MTS/IEEE, Washington, October, 2015.

[9] H. Koyama, A. Asada, T. Ura, H. Jun, T. Obara, K. Nagahasi, *Bathymetric Survey at Hydrothermal Site by L-array Interferometric Sonar Mounted on AUV-r2D4*, 2007 Symposium on Underwater Technology and Workshop on Scientific Use of Submarine Cables and Related Technologies, Tokyo, April 2007.

[10] C. R. German, D. R. Yoerger, M. Jakuba, T. Shank, and J. Lin, *Hydrothermal Exploration by AUV: Progress to-date with ABE in the Pacific, Atlantic & Indian Oceans*, IEEE/OES AUtonomous Underwater Vehicles, AUV 2008, Woods Hole, 2008.

[11] S. A. Jenkins, D. E. Humphreys, J. Sherman, C. Jones, N. Leonard, J. Graver, R. Bachmayer, T. Clem, P. Carroll, P. Davis, J. Berry, P. Worley, and J. Wasyl, *Underwater Glider System Study*, Scripps Institution of Oceanography, Technical Report No. 53, May, 2003.

[12] C. C. Eriksen, *Gliders*, Encyclopedia of Ocean Sciences (Second Edition), Academic Press,2009.

[13] R. Yeo, *Surveying the Underside of an Arctic Ice Ridge using a Man-portable GAVIA AUV Deployed Through the Ice*, OCEANS 2007, Vancouver, Canada, October, 2007.

[14] M. J. Doble, P. Wadhams, A. L. Forrest, and B. E. Laval, *Experiences from Tow-years' Through-ice AUV Deployments in the High Arctic*, 2008 IEEE/OES Autonomous Underwater Vehicles, AUV 2008, Woods Hole, 2008.

[15] H. Johannsson, T. Thorhallsson, and H. Hafsteinsson, *An Efficient Method of Combining Detection and Identification of Seafloor Objects using Gavia AUV*, OCEANS 2006, Boston, USA, September 2006.

[16] J. Leonard, A. Bennett, C. Smith, and H. Feder, *Autonomous Underwater Vehicle Navigation*, MIT Marine Robotics Laboratory Technical Memorandum 98-1, 1998.

[17] J. C. Kinsey, R. M. Eustice, and L. L. Whitcomb, *A Survey of Underwater Vehicle Navigation: Recent Advances and New Challenges*, 7th IFAC Conference on Manoeuvring and Control of Marine Craft (MCMC'2006), Portugal, September, 2006

[18] L. Stutters, H. Liu, C. Tiltman, and D. Brown, *Navigation Technologies for Autonomous Underwater Vehicles*, IEEE Transcations on Systems, Man and Cybernetics - Part C: Applications and Reviews, Vol. 38, 2008.

[19] P. A. Miller, J. A. fARRELL, Y. Zhao, and V. Djapic, *Autonomous Underwater Vehicle Navigation*, IEEE Journal of Oceanic Engineering, No. 3, Vol 35, 2010.

[20] L. Paull, S. Saeedi, M. Seto, and H. Li, *AUV Navigation and Localization: A Review*, IEEE Journal of Oceanic Engineering, No. 1, Vol. 39, 2014.

[21] J. G. Paglia and W. F. Wyman, *DARPA's Autonomous Minehunting and Mapping Technologies (AMMT) Program: An Overview*, OCEANS '96. MTS/IEEE, Fort Lauderdale, USA, September, 1996.

[22] A. R. Diercks, V. L. Asper, M. Woolsey, J. L. Williams, and F. Cantelas *NIUST AUV's study shipwrecks in the northern Gulf of Mexico*, 2010 IEEE/OES Autonomous Underwater Vehicles, Monterey, USA, September, 2010.

[23] P. Rigby, O. Pizarro, and S. B. Williams, *Towards geo-referenced auv navigation through fusion of USBL and DVL measurements* In Proceedings of the IEEE/MTS OCEANS Conference and Exhibition, September 2006.

[24] R. M. Eustice, L. L. Whitcomb, H. Singh and M. Grund, *Experimental results in synchronous-clock one-way-travel- time acoustic navigation for autonomous underwater vehicles*. In Proceedings of the IEEE international conference on robotics and automation (ICRA), Rome, Italy, April 2007, pp. 4257–4264.

[25] S. E. Webster, R. M. Eustice, H. Singh, and L. L. Whitcomb, *Advances in single-beacon one-way-travel-time acoustic navigation for underwater vehicles*, The International Journal of Robotics Research, 31(8), 935-949, 2012.

[26] Z. J. Harris and L. L. Whitcomb, *Preliminary Study of Cooperative Navigation of Underwater Vehicles without a DVL Utilizing Range and Range-Rate Observations*, IEEE International Conference on Robotics and Automation (ICRA), Stockholm, Sweden, May, 2016.

[27] B. Claus and R. Bachmayer, *Terrain-aided Navigation for an Underwater Glider*, Journal of Field Robotics 00(0), 1-17, 2015.

[28] G. Roberts and R. Sutton, *Advances in Unmanned Marine Vehicles*, The Institution of Eletrical Engineers, 2006.

[29] A. Bennet, J. Leonard, and J. Bellingham, *Bottom Following for Survey-Class Autonomous Underwater Vehicles*, International Symposium on Unmanned Untethered Submersible Technology, 1995.

[30] D. Yoerger, A. M. Bradley, B. B. Walden, H. Singh, and R. Bachmayer, *Surveying a subsea lava flow using Autonomous Benthic Explorer*, International Journal of Systems Science, Vol. 29, No. 10, 1998.

[31] W. K. Stewart, *Multisensor Modeling Underwater with Uncertain Information*, Ph.D thesis, Department of Ocean Engineering, MIT, July, 1988.

[32] R. Bachmayer, *Adaptive Control of an Experimental Underwater Vehicle*, Diplomarbeit, Institut fuer Industrielle Informationstecnik, Universitat Karlsruhe.

[33] S. McPhail, M. Furlong, and M. Pebody, *Low-altitude Terrain Following and Collision Avoidance in a Flight-class Autonomous Underwater Vehicle*, Proceedings of the Institution of Mechanical Engineers, Part M: Journal of Engineering for Maritime Environment, Vol. 224, 2010.

[34] J. Melo and A. Matos, *Bottom estimation and following with the MARES AUV*, MTS/IEEE Oceans, 2012, 2012

[35] N. Paulino, C. Silverstre, R. Cunha, and A. Pascoal, *A Bottom-Following Preview Controller for Autonomous Underwater Vehicles*, Proceedings of the 45th IEEE Conference on Decision & Control, San Diego, CA, USA, December, 2006.

[36] R. Skjetne, U. Jorgensen, and A. R. Teel, *Line-of-sight Path-following along Regularly Parametrized Curves Solved as a Generic Maneuvering Problem*, IEEE Conference on Decision and Control and European Control Conference, Orland, FL, USA, December, 2011.

[37] A. Lekkas, and T. Fossen, *Line-of-sight Guidance for Path Following of Marine Vehicles*, Chapter 5, Advanced in Marine Robotics, LAP LAMBERT Academic Publishing, 2013.

[38] J. Ghommam, F. Mnif, A. Benali, and N. Derbel, *Nonsingular Serret-Frenet Based Path Following Control for an Underactuated Surface Vessel*, Journal of Dynamic Systems, Measurement and Control, Vol. 131, March, 2009.

[39] S. Moe, *Path Following of Underactuated Marine Vessels in the Presence of Ocean Currents*, Master of Science in Engineerging Cybernetics, Department of Engineering Cybernetics, Norwegian University of Science and Technology.

[40] T. I. Fossen, K. Y. Pettersen and R. Galeazzi, *Line-of-Sight Path Following for Dubins Paths with Adaptive Sideslip Compensation of Drift Forces*, IEEE Transactions on Control Systems Technology, VOL. 23, NO. 2, March 2015.

[41] P. B. Sujit, S. Saripalli, and J. B. Sousa, *Unmanned Aerial Vehicle Path Following*, IEEE Control Systems Magazine, February 2014.

[42] A. Bruneau, and R. Dempster, *Engineering and Economic Implications of Icebergs in the North Atlantic*, Oceanology International, 1972.

[43] P. Benedict, *Dimensional Modelling of Icebergs*, Cold Regions Science and Technology, Vol. 1, 1980.

[44] Y. Wang, B. deYoung, and R. Bachmayer, *A Method of Above-water Iceberg 3D Modelling using Surface Imaging*, International Ocean and Polar Engineering Conference, Big Island, Hawaii, USA, June, 2015.

[45] Furgo GeoSurveys, *Integrated 3D Iceberg Mapping*, www.furgro.com.

[46] Canadian Seabed Research Limited, *Techniques for Determining the Maximum Draft of an Iceberg*, PERD/CHC Report 20-46, 2000.

[47] M. EL-Tahan and H. EL-Tahan, *Estimation of Iceberg Draft*, Oceans 82, 1982.

[48] A. Barker, M. Sayed, and T. Carrieres, *Determination of Iceberg Draft, Mass and Cross-sectional Areas*, The Fourteenth International Offshore and Polar Engineering Conference, 2004.

[49] L. D. Farmer, and R. Q. Robe, *Volumetric Measurements of Icebergs*, Polar and Ocean Engineering Under Arctic Conditions, Fairbanks, USA, 1975.

[50] P. Benedict, *Underwater Profiling of Icebergs*, Second International Conference on Port and Ocean Engineering Under Arctic Conditions, 1974.

[51] Oceans Ltd., *Determination of Iceberg Draft and Shape*, PERD/CHC Report 20-75, 2004.

[52] P. Kimball, S. Rock, *Sonar-based iceberg-relative AUV navigation*, IEEE/OES Autonomous Underwater Vehicles, 2008.

[53] A. Forrest, V. Schmidt, B. Laval, and A. Crawford, *Digital Terrain Mapping of Petermann Ice Island Fragments in the Canadian High Arctic*, 21st IAHR International Symposium on Ice, 2012.

[54] R. Bachmayer, B. deYoung, and D. Holland, *Working Towards Ice Profiling Using Underwater Gliders: Operational Experience in Western Greenland*, Symposium on Unmanned Untethered Submersible Technology, 2007

[55] M. Pebody, *Autonomous Underwater Vehicle Collision Avoidance for Under-ice Exploration*, Proceedings of the Institution of Mechanical Engineers, Vol. 222, No.2, 2008

[56] M. Zhou and R. Bachmayer, *Working towards single beam acoustic iceberg profiling using active roll control on a Slocum glider*, IEEE Symposium on Underwater Technology, 2011.

[57] M. Zhou, *The Approach of Improving the Roll Control of a Slocum Autonomous Underwater Glider*, Master's Thesis, Memorial University of Newfoundland, 2012.

[58] K. Kim, T. Ura, and etc., *Towards AUV-based iceberg profiling and gouging survey in arctic sea: The first Japanese under-ice AUV deployment in Okhotsk Sea*, IEEE International Underwater Technology Symposium, 2013.

[59] P. Kimball and S. Rock, *Sonar-Based iceberg-relative navigation for autonomous underwater vehicles*, Deep-Sea Research II, 2011.

[60] P. Kimball, S. Rock, *Estimation of Iceberg Motion for Mapping by AUVs*, IEEE/OES Autonomous Underwater Vehicles, 2010.

[61] M. Mammond and S. Rock, *Enabling AUV Mapping of Free-Drifting Icebergs Without External Navigation Aids*, IEEE/MTS OCEANS 2014, St. John's, Canada, September, 2014.

[62] M. Mammond and S. Rock, *A SLAM-based Approach for Underwater Mapping using AUVs with Poor Inertial Information*, IEEE/OES AUtonomous Underwater Vehicles, AUV 2014, Oxford, USA, October, 2014.

[63] P. Norgren and R. Skjetne, *Line-of-sight Iceberg Edge-following using an AUV Equipped with Multibeam Sonar*, 10th IFAC Conference on Manoeurving and Control of Marine Craft (MCMC), August 2015.

[64] J. Marko, J. Birch, and M. Wilson, *A Study of Long-Term Satellite-Tracked Iceberg Drifts in Baffin Bay*, Arctic, Vol. 35, No. 1, 1986.

[65] Canatec, *UAV Ice Beacon*, http://www.canatec.ca/wp-content/uploads/2015/07/UAV-Ice-Beacon.pdf.

[66] F. Pomerleau, F. Colas, and R. Siegwart, *Review of Point Cloud Registration Algorithms for Mobile Robotics*, Foundations and Trends in Robotics, Vol. 4, 2015.

[67] J. Submuth, M. Winter and Gunther Greiner, *Reconstructing Animated Meshes from Time-Varying Point Clouds*, Eurographics Symposium on Geometry Processing 2008.

[68] M. Whitty, S. Cossell, K. S. Dang, J. Guivant, and J. Katupitiya, *Autonomous Navigation using a Real-time 3D Point Cloud*, Australasian Conference on Robotics and Automation, 2010.

[69] H. Durrant-Whyte and T. Bailey, *Simultaneous Localisation and Mapping (SLAM): Part I*, IEEE Robotics and Automation Magazine, June, 2006.

[70] T. Bailey and H. Durrant-Whyte, *Simultaneous Localisation and Mapping (SLAM): Part II*, IEEE Robotics and Automation Magazine, September, 2006.

[71] J. B. A. Maintz and M. A. Viergever, *A Survey of Medical Image registration.*, Medical Image Analysis, Vol. 2 No. 1, March 1998.

[72] P. Besl and N. Mckay, *A Method for Registration of 3-d Shapes*, IEEE Transcations on Pattern Analysis and Machine Intelligence, Vol.14, 1992.

[73] G. Champleboux, S. Lavalllee, and R. Szeliski, and L. Brunie., *From Accurate Range Imaging sensor Calibration to Accurate Model-based 3D Object Localization*, Conference on Computer Vision and Pattern Recognition, 1992.

[74] Z. Zhang, *Iterative Point Matching for Registration of Free-form Curves and Surfaces*, International Journal of Computer Vision, Vol. 13, 1994.

[75] S. Ahuja, and S. Waslander, *3D Scan Registration using Curvelet Features*, Canadian Conference on Computer and Robot Vision, 2014.

[76] A. V. Segal, D. Haehnel, S. Thrun, *Generalized-ICP*, Robotics: Science and Systems 2009.

[77] M. Bosse and R. Zlot, *Map Matching and Data Association for Large-Scale Two-dimensional Laser Scan-based SLAM*, The International Journal of Robotics Research, Vol. 27 No. 6, 2008.

[78] S. Zhang, B. He, R. Nina, Y. Liang, and T. Yan, *SLAM and a Novel Loop Closure Detection for Autonomous Underwater Vehicles*, IEEE/MTS Oceans 2013, San Diego, CA, September, 2013.

[79] M. Labb and F. Michaud, *Online Global Loop Closure Detection for Large-Scale Multi-Session Graph-Based SLAM*, IEEE/RSJ International Conference on Intelligent Robots and Systems, 2014.

[80] K. Eik, *Review of Experiences within Ice and Iceberg Management*, The Journal of Navigation, Vol, 61, P557-572, 2008.

[81] J. McClintock, R. McKenna, and C. Woodworth-Lynas, *Grand Banks Iceberg Management*, PERD/CHC Report 20-84.

[82] National Energy Board, *Offshore Physical Environmental Guidelines Appendix B - Ice Management Program*, www.neb-one.gc.ca.

[83] J. Das, F. Py, T. Maughan, T. O'Reilly, M. Messie, J. Ryan, and G. Sukhatme, *Simultaneous tracking and sampling of dynamic oceanographic features with autonomous underwater vehicles and Lagrangian drifters*, 12th International Symposium on Experimental Robotics, New Delhi, India, December 2010.

[84] U. S. Coast Guard, *Search Patterns*.

[85] P. McGuire, A. Younan, Y. Wang, M. Gandi, T. King, K. Keeping, and K. Regular, *Smart Ice Management System - Rapid Iceberg Profiling System*, Arctic Technology Conference, Newfoundland, Canada, October, 2016.

[86] Teledyne Webb Research, *User Manual, Slocum Glider*, 2009.

[87] Institue Geographique National, Projection cartographique Mercator Transverse: Algorithmes, Notes Techniques NT/G 76, Janvier 1995.

[88] Tritech International Limited, *http://www.tritech.co.uk/chirp*.

[89] RD Instruments, *Acoustic Doppler Current Profiler Principles of Operation A Practical Primer*, RD Instruments, 1996.

[90] D. Sudom, A. Tivy and G. Timco, *Sea Ice and Iceberg Engineering on the East Coast of Canada*, PERD Workshop, 2013.

[91] D. Sudom, G. Timco, A. Tivy, *Iceberg Sightings, Shapes, and Management Techniques for Offshore Newfoundland and Labrador: Historical Data and Future Applications*, Oceans, 2014.

[92] P. Allaire, *Stability of Shimply Shaped Icebergs*, Journal of Canadian Petroleum Technology, 1972.

[93] N. Akkiraju, H. Edelsbrunner, M. Facello, P. Fu, E. P. Mucke and C. Varela, *Alpha shapes: definition and software*, Proc. International Computatioanl Geometry Software Workshop, Minneapolis 1995.

[94] R. Urick, *Principles of Underwater Sound*, McGraw-Hill, 1983.

[95] H. Medwin and C. Clay, *Fundamentals of Acoustical Oceanography*, Academic Press, 1998.

[96] P. Etter, *Underwater Acoustic Modeling: Principles, Techniques, and Applications*, Shock and VibrationDigest, 1984.

[97] P. Martz, *Generating Random Fractal Terrain*, http://www.gameprogrammer.com/fractal.html.

[98] W. Mason, *Physical Acoustics*, Vol. 2, Academic Press Inc., New York, 1965.

[99] W. Leonard, P. Combs, and L. Skidmore, *Attenuation of Sound in Synthetic Sea Water*, Journal of Acoustic Society of America, Vol. 21, 1949.

[100] R. Francois and G. Garrison, *Sound Absorption Based on Ocean Measurements. Part II: Boric Acid Contribution and Equation for Total Absorption*, Journal of Acousic Society of America, Vol. 72, 1982.

[101] J. Bell, *A Model for the Simulation of Sidescan Sonar*, Ph. D thesis, Department of Computing and Electrical Engineering, Heriot-Watt University, 1995.

[102] P. L. Graham, *An Efficient Algorithm for Determining the Convex Hull of a Finite Planar Set*, Information Processing Letters, 132-33, 1972.

[103] A. M. Andrew, *Another Efficient Alogrithm for Convex Hulss in Two Dimensions*, Information Processing Letters, Volumn 9, number 5, 1979.

[104] MeshLab, *http://meshlab.sourceforge.net*.

[105] Y. Chou, *Statistical Analysis*, Holt International, 1975.

[106] S. Thrun, W. Burgard, D. Fox, *Probabilistic Robotics*, MIT Press, 2015.

[107] A. Elfes, *Occupancy Grids: A Probabilistic Framework for Robot Perception and Navigation*, Ph. D Thesis, Carnegie-Mellon University, 1989.

[108] A. Elfes, *Sonar-Based Real-World Mapping and Navigation*, IEEE Journal of Robotics and Automation, Vol. RA-3, 1987.

[109] A. Hornung, K. Wurm, M. Bennewitz, C. Stachniss, and W. Burgard, *OctoMap: An Efficient Probabilistic 3D Mapping Framework Based on Octrees*, Autonomous Robots, Vol. 34, No. 3, 2013.

[110] P. Fofonoff, and R.C. Millard, *Algorithms for computation of fundamental properties of seawater*, Unesco Techinical Papers in Marine Science, Unesco 1983.

[111] Teledyne Blueview, *http://www.blueview.com/software/2d-imaging/proviewer/*

[112] S. E. Bruneau, *Icebergs of Newfoundland and Labrador*, Flanker Press Ltd., St. John's, NL, 2014.

[113] T. Nakatani, T. Ura, Y. Ito, J. Kojima, K. Tamura, T. Sakamaki, and Y. Nose, *AUV "TUNA-SAND" and its Exploration of Hydrothermal Vents at Kagoshima Bay*, OCEANS 2008 - MTS/IEEE, Kobe, April 2008.

[114] G. Ferri, M. V. Jakuba, D. R. Yoerger, *A Novel Method for Hydrothermal Vents Prospecting using an Autonomous Underwater Robot*, IEEE International Conference on Robotics and Automation, Pasadena, May, 2008.

[115] A. L. Forrest, B. Laval, M. J. Doble, R. Yeo, and E. Magnusson, *AUV Measurements of Under-ice Thermal Structure*, OCEANS 2008, Quebec City, Canada, September, 2008.

[116] International Ice Patrol, *Report of the International Ice Patrol in the North Atlantic, 2014 Season*, 2014

[117] T. Fossen, *Guidance and Control of Ocean Vehicles*, Wiley, 1994.

[118] Z. Li, *Design of a Robust Autonomous Surface Craft (ASC) for Deployment in Harsh Ocean Environment*, Master's Thesis, Memorial University of Newfoundland, 2012.

[119] J. Geisbert, *Hydrodynamic Modeling for Autonomous Underwater Vehicles using Computational and Semi-Empirical Methods*, Master's Thesis, Virginia Polytechnic Institute and State University, 2007.

[120] C. Woolsey, *Energy Shaping and Dissipation: Underwater Vehicle Stabilization using Internal Rotors*, Ph. D Dissertation, Princeton University, 2001.

[121] N. Mahmoudian, *Efficient Motion Planning and Control for Underwater Gliders*, Ph. D Dissertation, Virginia Polytechnic Institute and State University, 2009.

[122] D. Cook, A. Vardy and R. Lewis, *A Survey of AUV and Robot Simulators for Multi-Vehicle Operations*, Autonomous Underwater Vehicles (AUV), 2014, IEEE/OES, 2014.

[123] S. Carreno, P. Wilson, P. Ridao and Yvan Petillot, *A Survey on Terrain Based Navigation for AUVs*, MTS/IEEE Seattle, Oceans 2010, 2010.

[124] CANATEC Consultants Ltd., ICL Isometrics Ltd., CORETEC Inc. and Westmar Consultants Ltd., *Compliation of Iceberg Shape and Geometry Data for the Grand Banks Region*, PERD/CHC Report 20-43, June, 1999.

[125] B. Claus, and R. Bachmayer, *Experimental Flight Stability Tests for the Horizontal Flight Mode of a Hybrid Glider*, IEEE/OES Autonomous Underwater Vehicles, 2010.

[126] M. Zhou, R. Bachmayer, B. deYoung, *Initial Performance Analysis on Underside Iceberg Profiling with Autonomous Underwater Vehicle*, Oceans'14, St. John's, September, 2014.

[127] M. Zhou, *The Approach of Improving the Roll Control of a Slocum Autonomous Underwater Glider*, Master's Thesis, Memorial University of Newfoundland, September, 2012.

[128] P. Bhatta, *Nonlinear Stability and Control of Gliding Vehicles*, Ph. D Dissertation, Princeton University, September, 2006.

# Appendix A

# Appendix

## A.1 Coordinate systems and transformation

### A.1.1 General coordinate transformation

Figure A.1 depicts the transformation from coordinate $X-Y-Z$ to $X"-Y"-Z"$ by rotating about the Z-axis with an angle of $\rho_1$, Y-axis with an angle of $\rho_2$, and X-axis with an angle of $\rho_3$. For each rotation process a rotation matrix is associated with it and expressed in Equation A.1 to A.3.

$$R_{\rho_1} = \begin{pmatrix} \cos\rho_1 & \sin\rho_1 & 0 \\ -\sin\rho_1 & \cos\rho_1 & 0 \\ 0 & 0 & 1 \end{pmatrix} \tag{A.1}$$

$$R_{\rho_2} = \begin{pmatrix} \cos\rho_2 & 0 & -\sin\rho_2 \\ 0 & 1 & 0 \\ \sin\rho_2 & 0 & \cos\rho_2 \end{pmatrix} \tag{A.2}$$

$$R_{\rho_3} = \begin{pmatrix} 1 & 0 & 0 \\ 0 & \cos\rho_3 & \sin\rho_3 \\ 0 & -\sin\rho_3 & \cos\rho_3 \end{pmatrix} \tag{A.3}$$

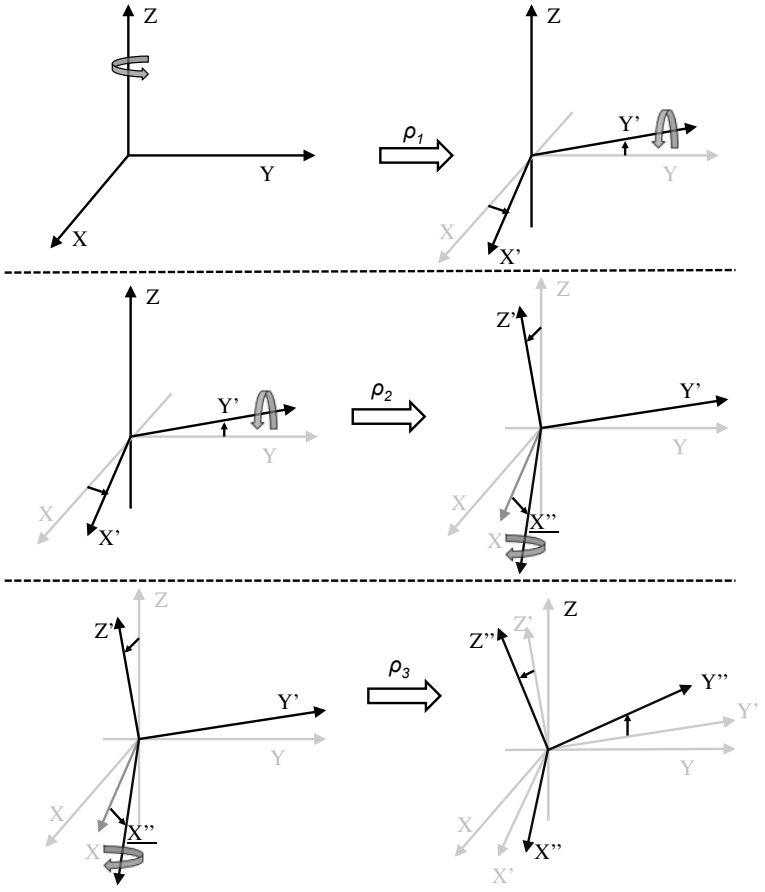


Figure A.1: Defination of $\phi$, $\theta$, and $\psi$ in rotating a coordinate system

Therefore, to transform a point in the $X-Y-Z$ to $X"-Y"-Z"$, the overall matrix is shown in Equation A.4. The transformation from a point in $X"-Y"-Z"$ to $X-Y-Z$ is the transpose of $R"$. The relation between a point in $X-Y-Z$ ($\mathbf{P}$) and a point in $X"-Y"-Z"$ ($\mathbf{P}"$) is shown in Equation A.5 and A.6.

$$\mathbf{R}" = R_{\rho_3} \cdot R_{\rho_2} \cdot R_{\rho_1} \tag{A.4}$$

$$\mathbf{P}" = \mathbf{R}"\mathbf{P} \tag{A.5}$$

$$\mathbf{P} = \mathbf{R}"^{T}\mathbf{P}" \tag{A.6}$$

## Converting sonar ranges into points in the vehicle coordinate system

Figure A.2 and A.3 shows the installation of the Tritech Micron mechanical scanning on the iceberg-profiling Slocum glider. The sonar is configurated to scan the starboard side of the vehicle with a forward-looking angle. The transducer rotates about the $Z_s$ axis shown in the Figure A.2. $\sigma$ is defined as the scan angle of the sonar relative to the plane $X_v - Y_v$, $\beta$ is the forward-looking angle when installing the sonar, and $\delta$ is the ray angle if the sonar propagation is modeled in the ray-tracing.

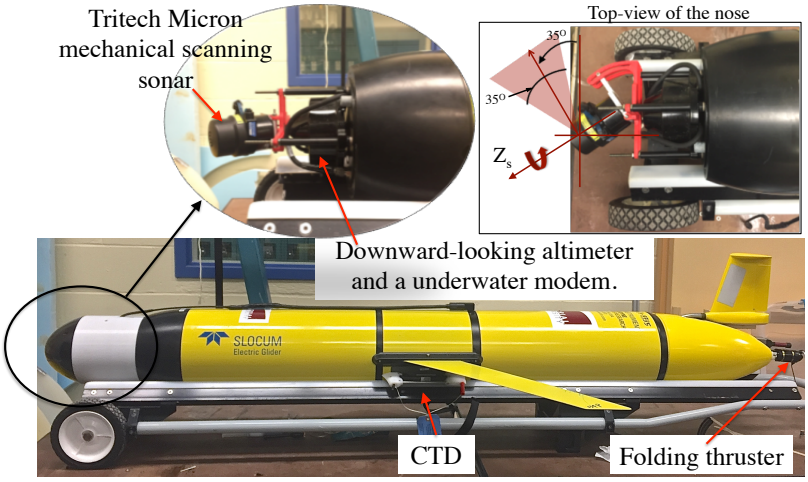


Figure A.2: Tritech Micron mechanical scanning sonar installed in the nose of the Slocum glider.

If we define a sensor frame $(X_s - Y_s - Z_s)$ that is attached to the transducer as shown in Figure A.3, the sensor frame is rotated from the vehicle coordinate system

$(X_v - Y_v - Z_v)$ about the $Z_v$-axis with an angle of $\delta + \beta$. When the sonar is scanning, the sensor frame is further rotated about the $X_s$-axis with an angle of $\sigma$. Therefore, a sonar range $R_t$ is converted into a point in the $X_v - Y_v - Z_v$ in Equation A.7 and Equation A.9 where $[x_s, y_s, z_s]^T$ is the mounting offset from the origin of the vehicle coordinate system. The sonar can be assumed located at the origin of $X_v - Y_v - Z_v$ because the offset is relatively small (1 meters) comparing to the sonar measured ranges (tens of meters). $\delta$ is usually unknown on a mechanical scanning sonar that is assumed $\delta = 0$ on a $R_t$, except the inverse-sonar model where $\delta$ is range for -17.5 to 17.5.

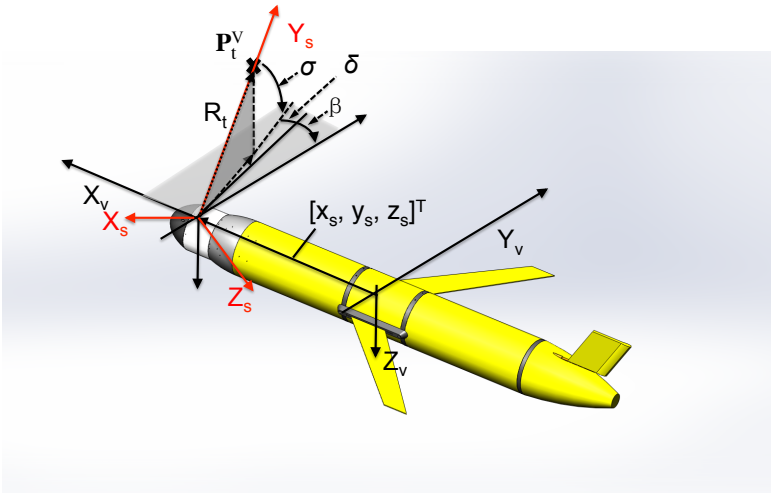


Figure A.3: Geometrical relation of converting $R_t$ to $\mathbf{P}_t^v$ using $\beta$, $\delta$, and $\sigma$.

$$\mathbf{P}_t^v = [R_\sigma \cdot R_{\beta+\delta}]^T \cdot \begin{bmatrix} 0 \\ R_t \\ 0 \end{bmatrix} + \begin{bmatrix} x_s \\ y_s \\ z_s \end{bmatrix} = \mathbf{R}_s^v \cdot \begin{bmatrix} 0 \\ R_t \\ 0 \end{bmatrix} + \begin{bmatrix} x_s \\ y_s \\ z_s \end{bmatrix} \tag{A.7}$$

$$\mathbf{R}_s^v = \begin{pmatrix} \cos(\beta+\delta) & \sin(\beta+\delta) & 0 \\ -\sin(\beta+\delta) & \cos(\beta+\delta) & 0 \\ 0 & 0 & 1 \end{pmatrix}^T \cdot \begin{pmatrix} 1 & 0 & 0 \\ 0 & \cos\sigma & \sin\sigma \\ 0 & -\sin\sigma & \cos\sigma \end{pmatrix}^T \tag{A.8}$$

$$\mathbf{P}_t^v = \begin{bmatrix} -\cos\sigma \cdot \sin(\beta+\delta) \\ \cos\sigma \cdot \cos(\beta+\delta) \\ \sin\sigma \end{bmatrix} \cdot R_t + \begin{bmatrix} x_s \\ y_s \\ z_s \end{bmatrix} \approx \begin{bmatrix} -\cos\sigma \cdot \sin(\beta+\delta) \\ \cos\sigma \cdot \cos(\beta+\delta) \\ \sin\sigma \end{bmatrix} \cdot R_t \qquad \text{(A.9)}$$

Figure A.4 shows the installation of the Blueview multibeam sonar on a surface vessel. It is mounted with zero forward-looking angle with a fan-shape field-of-view as shown in Figure A.4. The sonar is oriented with angle of $\Delta\sigma$ to align the edge of the field-of-view horizontally. As a result from processing the sonar measurements, the range and bearing $\sigma$ is known from the sonar to obstacles. In order to convert a range $R_t$ into the vehicle coordinate system, $\sigma$ is offset by $\Delta\sigma$ in converting $R_t$ into $\mathbf{P}_t^v$ in Equation A.9 where $\beta$ and $\delta$ are zero for the Blueview. The offset vector $[X_s, Y_s, Z_s]^T$ can be assumed zero that the sonar is installed at the origin of the vehicle coordinate because the offset is relatively small (less 1 meter on the glider and less than 10 meters on the vessel) comparing to the profiling range of the sonar (75 meters on the glider and 150 meters on the support vessel).

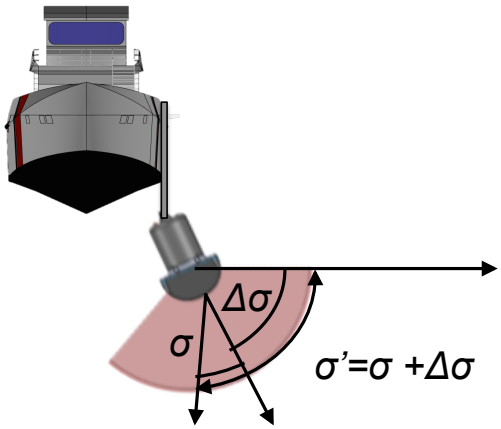


Figure A.4: The blueview multibeam sonar is rotated with an angle of $\Delta\sigma$ to align one margin of the field of view horizontally.

## Converting points from the vehicle coordinate system into inertial coordinate systems

Figure A.5 shows a vehicle coordinate system, $X_v - Y_v - Z_v$ and an inertial coordinate system, $X_e - Y_e - Z_e$. The $X_e - Y_e - Z_e$ is firstly rotated to $X"_e - Y"_e - Z"_e$ then translated to $X_v - Y_v - Z_v$ with a vector $\mathbf{T}^e_{v,t}$. Comparing to the general case in transforming coordinate systems, $\rho_1$ is the yaw angle ($\psi$), $\rho_2$ is the pitch angle ($\theta$), and $\rho_3$ is the roll angle ($\phi$). To convert a point in the vehicle coordinate system $\mathbf{P}^v_t$ to point in the inertial coordinate system $\mathbf{P}^e_t$, Equation A.10 is used where $\mathbf{R}^e_{v,t}$ is the transpose of $\mathbf{R}^{v,t}_e$ (Equation A.11) and $\mathbf{T}^e_{v,t}$ is a translation matrix. The individual rotation matrice in Equaion A.11 is shown in Equation A.12 to A.14. Equation A.15 and A.16 shows the detail elements in the overall rotation matrice.

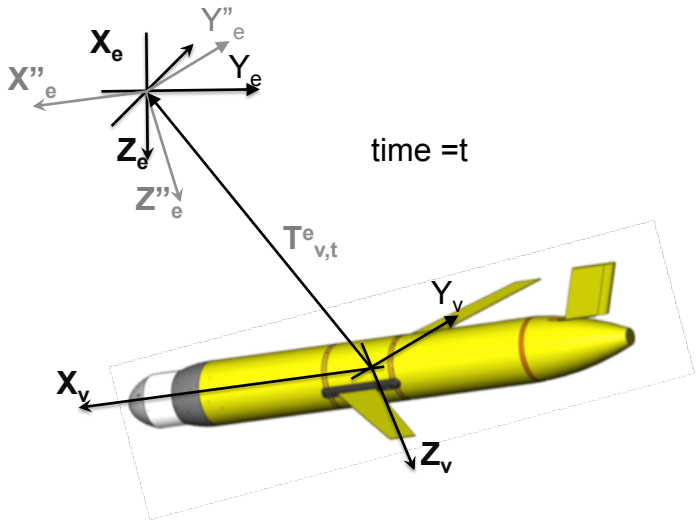


Figure A.5: Inertia coordinate systems and Vehicle coordinate system

$$\mathbf{P}^e_t = \mathbf{R}^e_{v,t} \cdot \mathbf{P}^v_t + \mathbf{T}^e_{v,t} \tag{A.10}$$

$$\mathbf{R}^{v,t}_e = R_\phi R_\theta R_\psi \tag{A.11}$$

$$R_{\psi} = \begin{pmatrix} \cos\psi & \sin\psi & 0 \\ -\sin\psi & \cos\psi & 0 \\ 0 & 0 & 1 \end{pmatrix} \tag{A.12}$$

$$R_{\theta} = \begin{pmatrix} \cos\theta & 0 & -\sin\theta \\ 0 & 1 & 0 \\ \sin\theta & 0 & \cos\theta \end{pmatrix} \tag{A.13}$$

$$R_{\phi} = \begin{pmatrix} 1 & 0 & 0 \\ 0 & \cos\phi & \sin\phi \\ 0 & -\sin\phi & \cos\phi \end{pmatrix} \tag{A.14}$$

$$\mathbf{R}_{e}^{v,t} = \begin{pmatrix} \cos\psi\cos\theta & \sin\psi\cos\theta & -\sin\theta \\ -\sin\psi\cos\phi + \cos\psi\sin\theta\sin\phi & \cos\psi\cos\phi + \sin\phi\sin\theta\sin\psi & \cos\theta\sin\phi \\ \sin\psi\sin\phi + \cos\psi\cos\phi\sin\theta & -\cos\psi\sin\phi + \sin\theta\sin\psi\cos\phi & \cos\theta\cos\phi \end{pmatrix} \tag{A.15}$$

$$\mathbf{R}_{v,t}^{e} = \begin{pmatrix} \cos\psi\cos\theta & -\sin\psi\cos\phi + \cos\psi\sin\theta\sin\phi & \sin\psi\sin\phi + \cos\psi\cos\phi\sin\theta \\ \sin\psi\cos\theta & \cos\psi\cos\phi + \sin\phi\sin\theta\sin\psi & -\cos\psi\sin\phi + \sin\theta\sin\psi\cos\phi \\ -\sin\theta & \cos\theta\sin\phi & \cos\theta\cos\phi \end{pmatrix} \tag{A.16}$$

The orientation, $\phi$, $\theta$, and $\psi$ in the rotation matrix are usually measured using compass and altitude sensor while $\mathbf{T}_{v,t}^{e}$ is the vehicle's location relative to the origin of the inertial coordinate system. The origin of an inertial coordinate system is defined at a known location on the earth. Its x-axis is pointed north, its y-axis is pointed east, and its z-axis is pointed downward. The most common inertial coordinate systems are the

Universal Transverse Mercator (UTM) coordinate system and Longitude-Latitude-Depth coordinate system. The transformation between two coordinate system are introduced in [87]. North-East-Down coordinate system can be derived from UTM by shifting its origin to a known location near the mission site.

## A.2 Iceberg reconstruction

In the thesis, the sonar measured ranges are initially converted into points clouds in an inertial coordinate system. However, these points are required to be converted into an iceberg-attached coordinate system (see Section 5.1 in Chapter 5). The resulting point cloud $\mathbf{P}_t^i$ is used to reconstruct the iceberg surface. Figure A.6 shows an example of the process of shape reconstruction. In the first step, the three-dimensional point cloud is rearranged into cross-sectional profiles at discrete depths. Then the cross-sectional profiles are smoothed with a moving average filter. Because a sparser point cloud will result empty region in the reconstruction, the data points are further interpolated to increase the sample density and to decrease the distance between the neighbor points. Finally, the Alpha Shape [93] is apllied on the processed point cloud to reconstruct surface between adjacent points. This process is implemented in the MATLAB script.

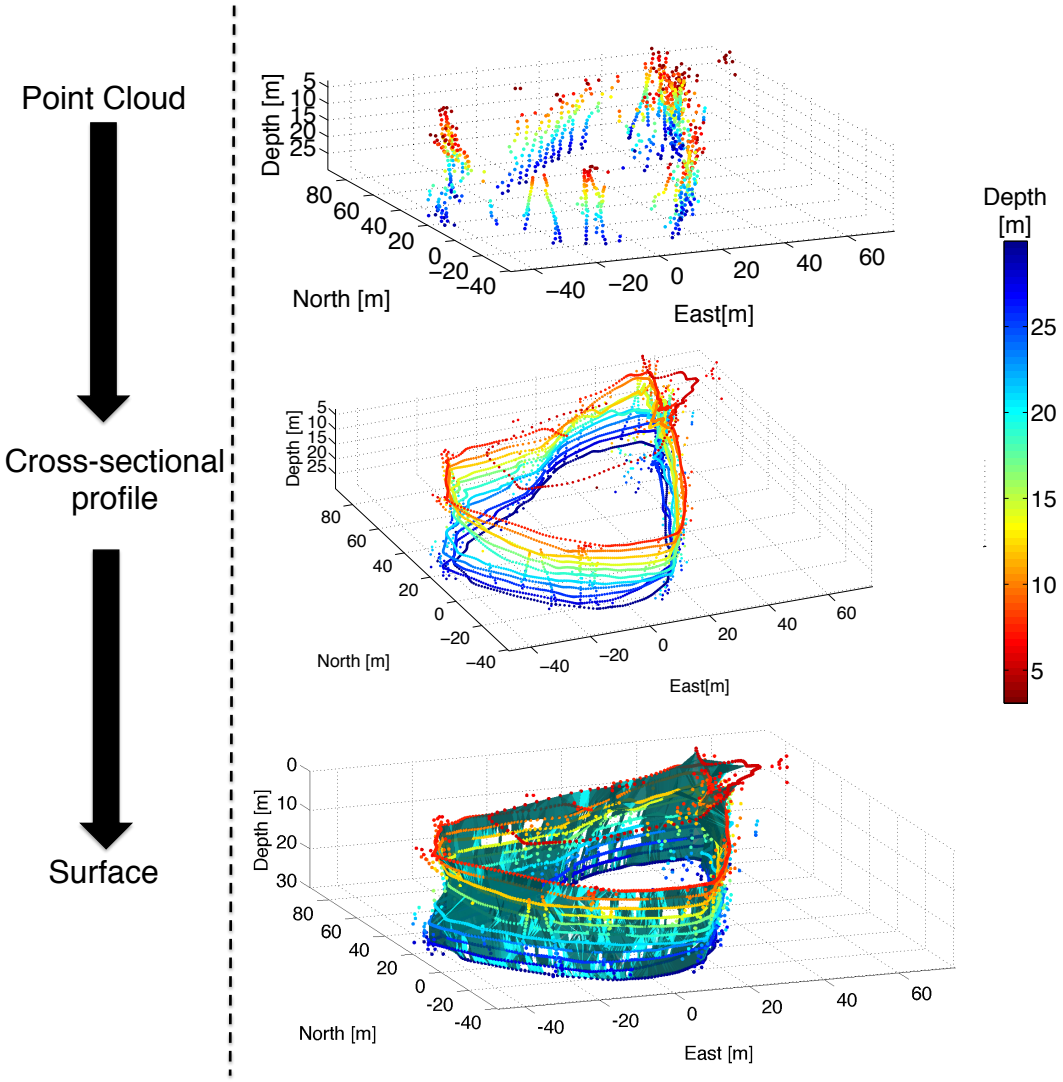


Figure A.6: Reconstruction of a iceberg shape from a point cloud

## A.3 Resutling point clouds in iceberg profiling verification

In the Chapter 3, a verification is conducted on the conventional and AUV-based iceberg profiling operation. The sonar was configurated in three levels of pinging rate, 1 Hz, 2 Hz, and 5 Hz. As a result, a total of 18 simulation were conducted on the three target iceberg from the iceberg database provided by the National Research Council Canada (NRCC). The following figures summarize the cross-sectional profiles obtained from different platforms at various sonar pinging rates on the three icebergs. The top plots in the figures are the reference cross-sectional profiles from the iceberg database.

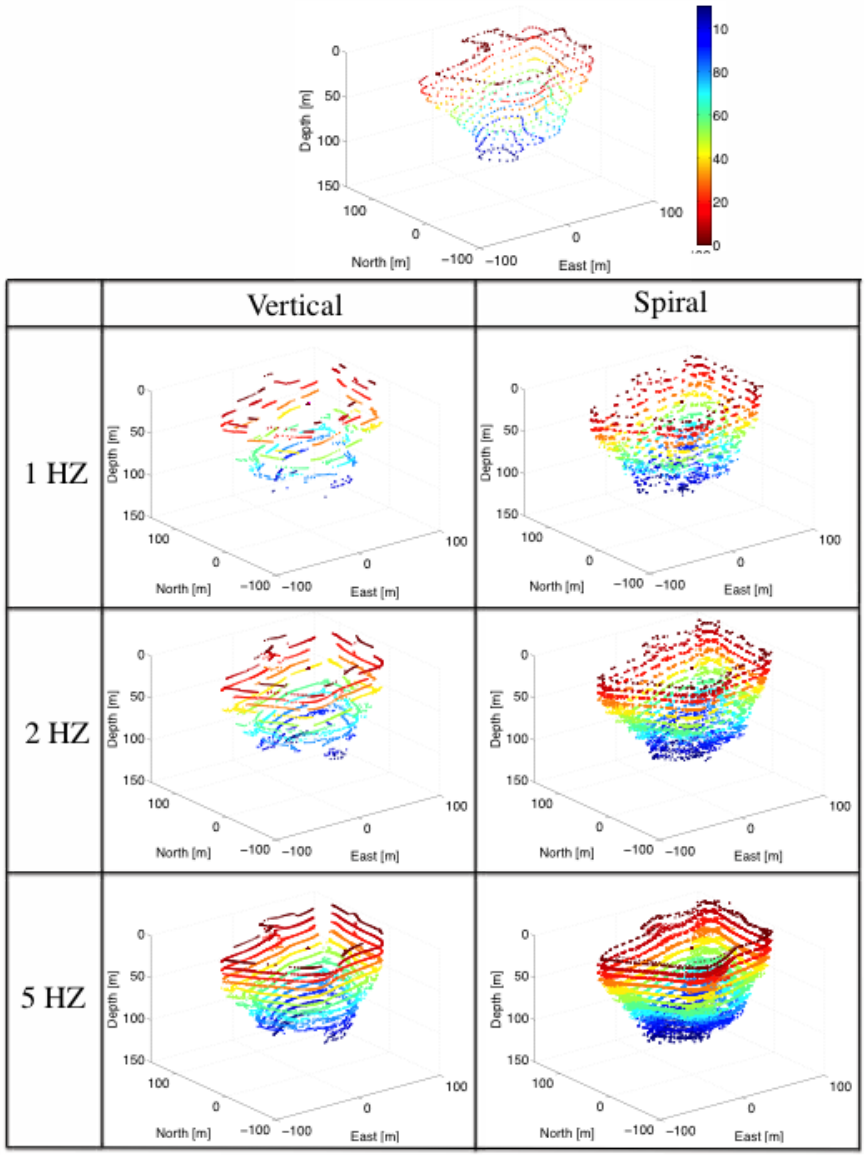


Figure A.7: Reuslting cross-sectional profiles from different platforms on R11i01 with three levels of pinging rate. The top plot is the reference data points from the iceberg database.

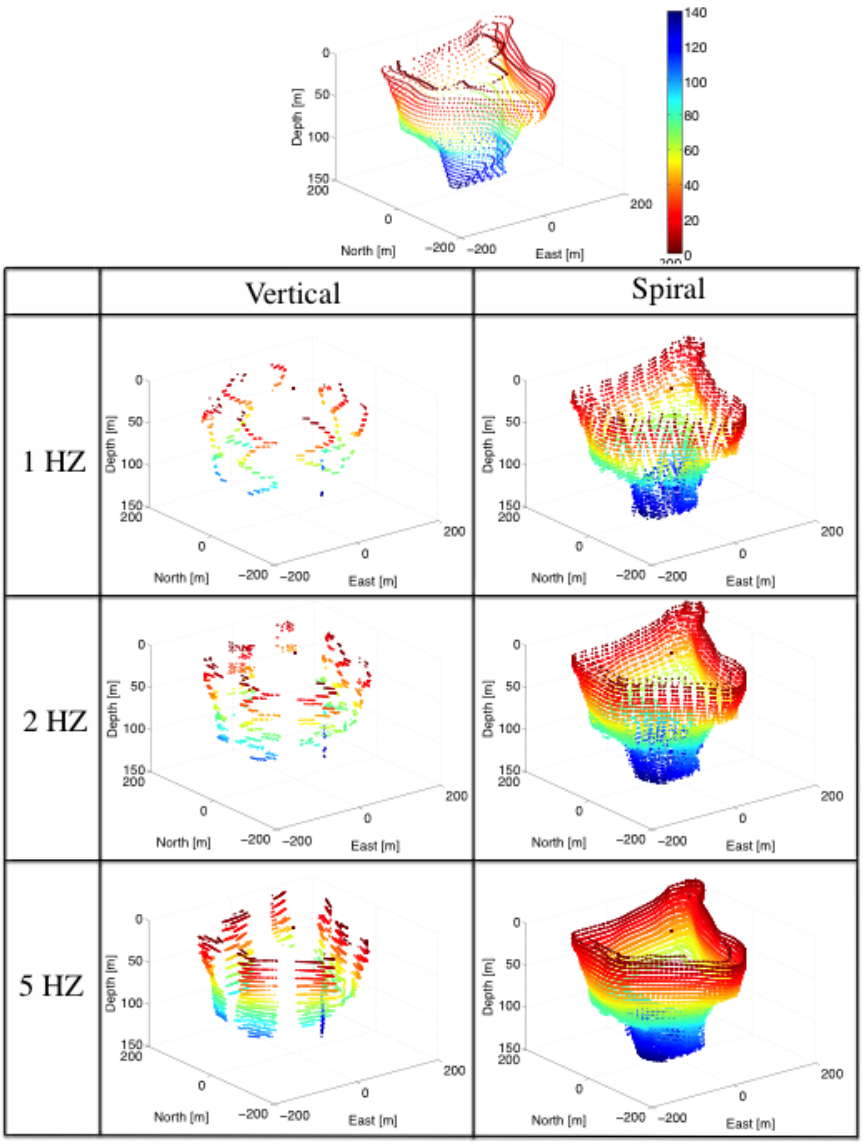


Figure A.8: Reuslting cross-sectional profiles from different platforms on R11i02 with three levels of pinging rate. The top plot is the reference data points from the iceberg database.

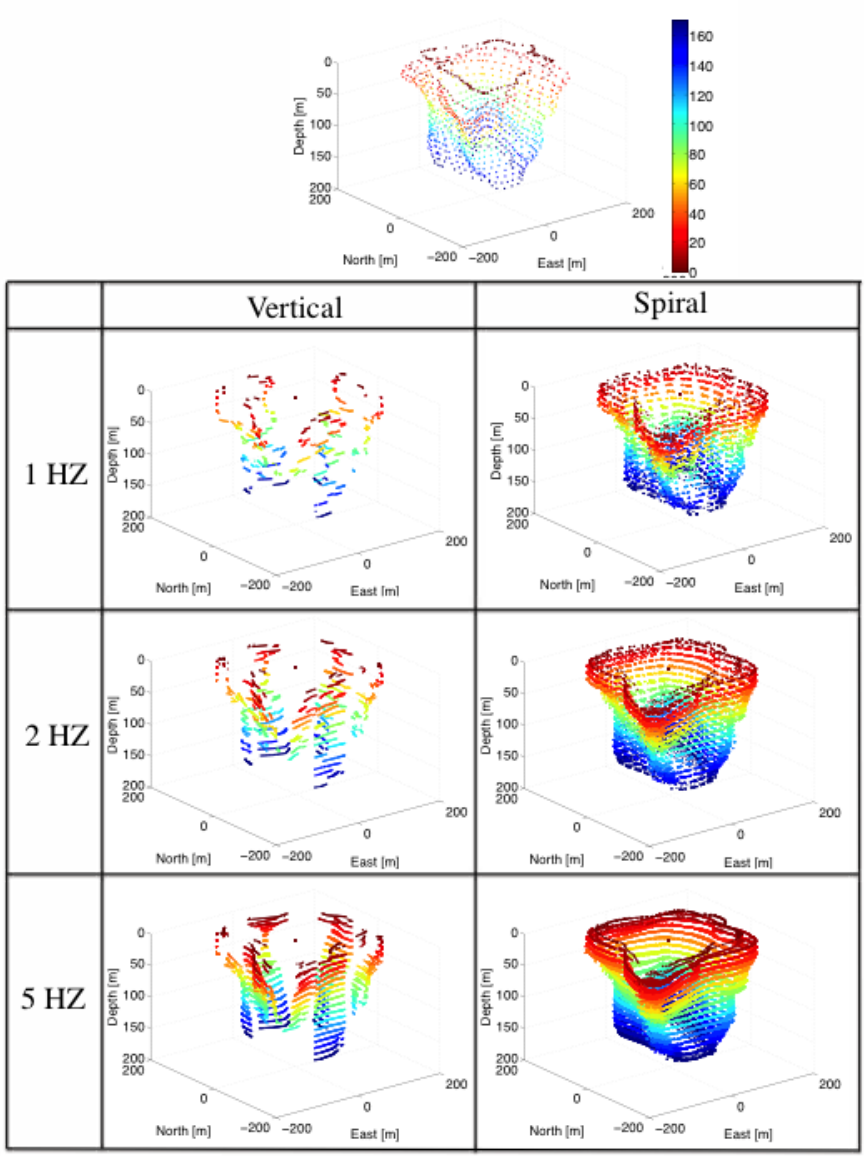


Figure A.9: Reuslting cross-sectional profiles from different platforms on R11i03 with three levels of pinging rate. The top plot is the reference data points from the iceberg database.